Study of High Aspect-Ratio Dual Intersecting Jets and the Installation Effect on Control Authority

An Experimental and Numerical Investigation

Mazen Zohiry

In the loving memory of my late father, Mohamed Zohiry, for whom I overworked myself to achieve this milestone and make proud.

Gone but never forgotten...

- Mazen Zohiry

Study of High Aspect-Ratio Dual Intersecting Jets and the Installation Effect on Control Authority

An Experimental and Numerical Investigation

Thesis Report

by

Mazen Zohiry

to obtain the degree of Master of Science
at the Delft University of Technology
to be defended publicly on March 31, 2023

Thesis committee:

Chair:	Dr. Daniele Ragni
Supervisors:	Dr. Daniele Ragni
	Dr. Woutijn Baars
	Senior Aerodynamicist, Tesla: Christopher Wood
External examiner:	Dr. Steven Hulshoff
Place:	Faculty of Aerospace Engineering, Delft
Project Duration:	May 2022 - April 2023
Student number:	5280281

An electronic version of this thesis is available at http://repository.tudelft.nl/.

Faculty of Aerospace Engineering · Delft University of Technology

Preface

Transforming my Master's thesis project into a reality has been an epic journey filled with remarkable discoveries in the field of free shear flows' aerodynamics. My desire to work on a project that directly impacts consumers drove me to collaborate with a company, and what better way to do so than to join Tesla's Engineering team! Being part of Tesla's most innovative Engineering team has been a goal of mine for several years before joining the Aerothermal team at Tesla as an intern in August 2022. I was blown away by the number of interesting projects the team was working on and the immense potential for learning and personal growth within the team. This realization motivated me to choose an industrial project at Tesla for my Master's thesis. With the guidance of my manager and team, I proposed the idea of investigating momentum mixing in air jets, the concept that air vents in current Tesla production vehicles rely on. Juggling my research alongside Tesla projects was an uphill battle, but spending time doing what I'm truly passionate about was totally worth it. I want to extend my heartfelt gratitude to Dr.ir. Dani Ragni and Dr. Woutijn Baars for their guidance and supervision throughout this thesis project. Additionally, I want to thank my manager Christopher Wood and my teammates for their steadfast support, without which I wouldn't have been able to conclude this project. Most importantly, I couldn't have achieved this milestone without the unwavering support of my family. From my dad, mom, sister, brother, and all my friends who cheered me on from afar to my most-supportive fiancee and soon-to-be wife, Menna, who never stopped empowering me through the toughest moments of the journey. I'm beyond grateful for their endless motivation and belief in me, and I'll carry their love and encouragement with me wherever I go!

Mazen Zohiry
Thursday 6th April, 2023

Contents

Nomenclature

Abbreviations

AD	Axisymmetric Decay
AR	Aspect Ratio
ASHARE	The American Society of Heating, Refrigerating and Air-Conditioning Engineers
CD	Characteristic Decay
CFD	Computational Fluid Dynamics
DNS	Direct Numerical Simulation
HVAC	Heating, Ventilation and Air-Conditioning
HWA	Hot Wire Anemometry
IP	Instrument Panel
ISO	International Organization for Standardization
LDA	Laser Doppler Anemometry
MFR	Mass flow ratio
PC	Potential Core
PIV	Particle Image Velocimetry
PMV	Predictive Mean Vote
PPD	Predicted Percentage Dissatisfied

Symbols

α	Twin jet angle between the incident velocity vectors	$^\circ$
γ	Twin jet angle between the merged jet and the weaker jet	$^\circ$
Λ	Jet's half-width growth in the minor axis	m
λ	Jet's half-width growth in the major axis	m
μ	Kinematic viscosity	$\mathrm{m\,s^{-2}}$
ρ	Air density	$\mathrm{kg\,m^{-3}}$
τ_{lam}	Laminar shear stress	$\mathrm{N\,m^{-1}}$
τ_{turb}	Turbulent shear stress	$\mathrm{N\,m^{-1}}$
θ	Twin-jet discharge angle	$^\circ$
a	Twin-jet spacing surface recession	m
cp	Twin-jet combined Point	-
d	Twin-jet nozzle total height	m
e	Eccentricity	-
h_{cv}	Twin-jet merged jet centerline velocity	m
K	Fluid thermal conductivity	-
l	Nozzle outlet major dimension (length)	m
mp	Twin-jet merging Point	-
n	Characterstic decay exponent	-
p_∞	Total pressure	Pa
r	Twin jet velocity ratio	-
Re	Reynolds Number	-
s	Twin-jet center-to-center distance	m
T_b	Target object temperature	$^\circ$C
t_{cl}	Twin-jet merged jet centerline velocity	m
T_f	Cooling Fluid temperature	$^\circ$C
t_{mr}	Twin-jet merged jet centerline velocity	m
U_c	Single jet centerline velocity/Twin-jet merged jet centerline velocity	$\mathrm{m\,s^{-1}}$
U_{o1}	Twin-jet stronger jet discharge centerline velocity	m
U_{o2}	Twin-jet weaker jet discharge centerline velocity	m
U_{oc}	Single jet Max centerline velocity	$\mathrm{m\,s^{-1}}$
w	Nozzle outlet minor dimension (height) - channel height for twin-jets	m
x_{AD}	Twin jet's onset of the Axisymmetric Region	m
x_o/y_o	Twin jet's virtual origin depending on orientation	-
x_{PC}	Twin jet's streamwise extent of Potential Core	m
x_{rp}	Offset jet's reattachment point streamwise location	m

List of Figures

List of Tables

1 Introduction

1.1. Background and Motivation

1.1.1. Thermal Sensation and Comfort

Thermal sensation varies in a non-uniform fashion across the different body parts, meaning that not all body parts perceive warmth or cool at the same level. The non-uniformity in sensation results from a few factors, the uneven distribution of sensory neurons across the skin - some body parts have more receptors than others, the variation in the body's local thermoregulatory mechanisms, and the asymmetry in clothing and surrounding conditions, to mention a few. Additionally, local comfort changes throughout the body depending on the rest of the body parts' thermal condition. Some measure comfort based on the local comfort of more sensitive body parts, while others base it on the number of comfortable body areas. The author agrees with the literature suggesting that overall thermal comfort is a weighted function of the local comfort of all body parts [1]; making ideal comfort achievable by creating a comfort sleeve that provides uniform heating/cooling around the subject. Although there is literature that tries to understand the thermosensitivity of specific bodies (e.g., [2, 3]), to the author's knowledge, there is no established approach to appraise how comfort is integrated into people's minds. Despite the previous controversy, the European EN ISO [4] (Parts 1,2, and 3) and the American ASHRAE standard [5] are two extensively used standards to assess thermal comfort. These standards use various scales such as the Predicted Mean Vote - Predicted Percentage Dissatisfied (PMV-PPD) [6] or the Standard Equivalent Temperature (SET) [7]. These standards are often employed in the building/indoor heating, ventilation, and air conditioning (HVAC) segment, as they are more suited for judging comfort under consistent conditions.

Fanger performed a study over 30 years ago in which volunteers wore "standard" attire, performed "standard" activities, and were subjected to various heat conditions. The volunteers evaluated their comfort state using the conventional ASHRAE scale with seven values (-3: cold, -2: cool, -1: slightly cool, 0 neutral, 1: slightly warm, 2: warm, 3: hot)[5]. After analyzing the human body's thermoregulation and heat transfer mechanisms, Fanger proposed the PMV index, per the ASHRAE seven-value scale. By introducing the external physical quantities that influence the nature of heat transfer and some individual variables related to the human body's thermal equilibrium, Fanger obtained a relationship between the produced and released body heat flux. Using nine variables, the PMV index was computed and mapped on the same -3 to 3 ASHRAE scale through (1.1); these variables are outlined in Figure 1.1. When Fanger's heat balance equation is satisfied, the heat generated by the human body is dissipated without an increase in the activity of the body's thermoregulatory system. The PPD index is another form

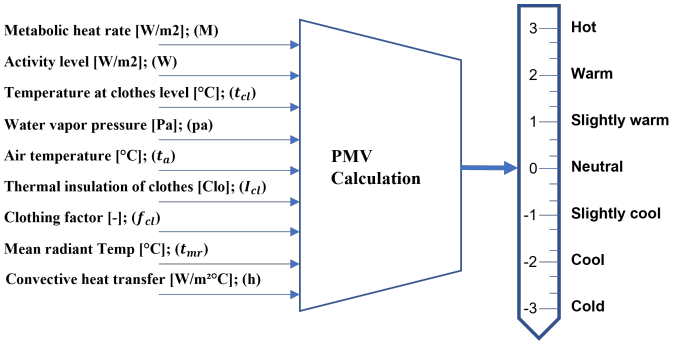

Figure 1.1: PMV Index Calculations Schematic [8]

of PMV indicating the percentage of individuals undergoing the test and experiencing thermal discomfort [8].

$$\begin{aligned} PMV = (0.303e^{0.303} + 0.028)\{&(M-W) - 3.05[5.73 - 0.007(M-W) - p_a] \\ &- 0.42[(M-W) - 58.15] - 0.0173M(5.87 - p_a) - 0.0014M(34 - t_a) \\ &- 3.96 \times 10^{-8} f_{cl}[(t_{cl}+273)^4 - (t_{mr}+273)^4] - \underbrace{f_{cl}h_{cv}(t_{cl}-t_a)}_{\text{Weighted Convective Heat Transfer}} \} \end{aligned} \tag{1.1}$$

With an unprecedented surge in the number of individuals utilizing personal vehicles for commuting across the globe, it is becoming critical to immediately deliver an adequate degree of comfort efficiently in car cabins to help drivers remain focused and attentive [9]. A pleasant thermal experience may also decrease weariness and irritation, increasing driving safety [10]. As the thermal conditions inside a vehicle may vary quickly, one might argue that the PMV index standard falls short of capturing the vehicle's spatiotemporally non-uniform and asymmetric conditions. Nonetheless, several studies have continued to apply similar guidelines to assess thermal sensation in vehicle cabins. One of these investigations performed in [1] studied the environmental characteristics of a car parked inside and outside for almost a year with four individuals. This study claims that the PMV index can be modified to use weighted average variables to appropriately predict the passengers' comfort level in a vehicle to a reasonable extent.

1.1.2. Vehicle Thermal Environment

Several parameters, such as heating, ventilation, and air conditioning (HVAC) airflow temperature, speed and direction, interior surface temperatures, solar radiation intensity, and incidence angle, all influence the environment observed by vehicle passengers [8]. When the car is in motion, and the HVAC system is switched on, the passenger compartment's interior temperature and humidity change swiftly. As a result of the confined and complex geometry of the space, airflow movement in the vehicle becomes exceedingly dynamic. Additionally, the degree of focus maintained by the driver operating the vehicle or another passenger performing a different task affects the metabolic rate and hence the passenger comfort as indicated by (1.1). All of these factors contribute to a thermal sensation which differs from that observed in other conditioned spaces. Given the preceding, it is critical to comprehend the thermal environment, human thermoregulation, and comfort assessment methods to achieve adequate thermal comfort in a vehicle. As shown in Figure 1.2, the heat transfer between a passenger and the vehicle environment is more involved than that occurring in an enclosed room, for instance. The different driving modes, variable weather conditions along the ride, and the vehicle's HVAC system operation settings all render

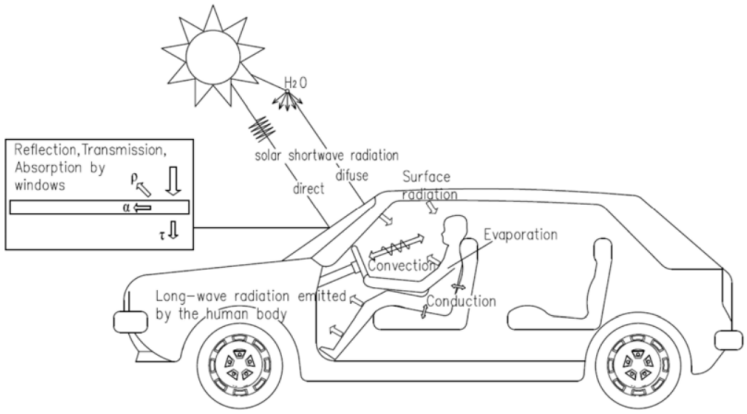

Figure 1.2: Heat transfer between a human body and its surroundings in a car [11]

the thermal environment of a vehicle non-uniform, and irregular [12]. Before proposing ways to attain sufficient thermal comfort, it is essential to provide a brief analysis of the heat exchange in a vehicle. The heat transfer between a human body and the surroundings (Q_{tot}) consists of four elements, namely, convective heat transfer (Q_{cv}), radiative heat transfer (Q_r), conductive heat transfer (Q_{cd}), and evaporative/metabolic heat transfer (E_{sk}) as expressed in (1.2). [13, 14, 2]:

$$Q_{tot} = Q_{cv} + Q_{cd} + Q_r + E_{sk} \tag{1.2}$$

In case of elevated temperature, the evaporative/metabolic heat transfer occurs (in the form of sweat), which carries a significant share of energy from the skin. Through this form of heat transfer, the passenger body tries to achieve thermal equilibrium in response to the energy added through the other forms of heat transfer; this is illustrated by the arrows in Figure 1.2. In the extreme outside solar loading, the occupant body, under real driving circumstances, could exchange additional heat through radiation [15], [3] and conduction [16] than in an indoor setting. While the vehicle's exterior surfaces (especially the glass) reflect some solar energy, the remaining wavelengths of the radiation are either transmitted or absorbed into the cabin surface, which both contribute to raising the solar load on the vehicle. By increasing the cabin's surface temperature, the long-wave absorbed radiation enhances the exterior's radiative heat transfer capability. Meanwhile, the passenger receives the transmitted short wavelength radiation directly. Moreover, about 25% of the occupant's body surface area is in touch with the seat, headrest, and steering wheel in a vehicle [16]. These surfaces exchange heat with the body parts in contact through conduction. In addition to radiation, conduction and evaporation, an important form of heat transfer between a human body and its surroundings is convection. The level of area averaged convection (q''_{cv}) depends on the convective heat transfer coefficient h_{cv} and the difference between the occupant's body temperature T_b and the airflow temperature T_f as expressed in (1.3). By observing the thermal PMV index formula in (1.1) closely, **it can be noticed that the last test term aligns with the convective heat transfer equation which is a pathway to the topic of this thesis**.

$$q''_{cv} = h_{cv}(T_b - T_f) \tag{1.3}$$

According to the preceding, thermal comfort commences when the passenger's body achieves thermal equilibrium by receiving enough convective heat transfer to offset the sum of conduction, radiation, and evaporation. Sufficient occupant thermal comfort could be achieved in two ways: cabin thermal load reduction and cabin ventilation. The earlier involves advanced thermal insulation for the cabin, double pane glass windows, solar reflective glazing, solar reflective paint, low

mass seats, and other techniques [4]. The latter uses the HVAC system to provide airflow to the vehicle's passenger cabin through several air vents, enabling hotter/colder, more comfortable and dehumidified air as needed. These vents control the rate and direction of the airflow entering the cabin and are usually installed on the instrument panel (IP) for front-row ventilation. In some vehicles, air vents can be found on consoles or mounted to the B-pillars in the second row for rear passengers' comfort. These vents are connected to the HVAC distribution unit, which encloses the blower responsible for the fresh air intake, via under-IP ducting for the first-row vents and under-floor ducting for those in the rear row(s) [17]. The functionality of the HVAC system lies in controlling the convective heat transfer experienced by the occupant or in other words adjusting the h_{cv} and T_f terms in (1.3) to maximize q''_{cv}. The heat transfer coefficient could be thought of as a proportionality at which convective heat transfer takes place per unit area per a degree of temperature difference between the target body and the cooling air; making the heat transfer coefficient a combined property of fluid, flow, and geometry of the body. The convective heat transfer coefficient can be expressed as:

$$h_{cv} = \frac{NuK}{L} \quad \text{where;} \quad Nu = f(Re, Pr), \quad Re = \frac{\rho v L}{\mu}, \quad Pr = \frac{\mu cp}{K} \tag{1.4}$$

Nu is the Nusselt number, Re is the Reynolds Number, and Pr is the Prandtl number. K is the thermal conductivity of the fluid, L is the characteristic length of the geometry, cp is the fluid heat capacity. As indicated by (1.4), the value of the convective heat transfer coefficient h_{cv} is proportional to a few fluid characteristics (which are constants for known conditions) and directly proportional to the flow velocity. The dependency of the convective heat transfer coefficient on the Reynolds number can be explained as follows; when the flow convectes against the surface of the object to be cooled, this surface acts as a no-slip wall. For a smooth surface (e.g., skin), a viscous sub-layer forms near the surface, providing significant resistance to heat flow since the heat flow across this layer is governed by conduction. Increasing the turbulence intensity of the flow promotes eddies in this layer which enhances the mixing of the fluid and, hence, promotes the convective transport of heat to the outer turbulent flow. The velocity and turbulence intensity of the airflow entering the cabin can be immediately controlled by the HVAC operation settings and the air vent design; allowing control over the heat transfer coefficient. The airflow temperature governs the other term of the equation; the ambient air gets cooled by the evaporator of the HVAC system; however, it partially loses some of its cooling power as it passes through the distribution unit, the ducting, and the air vents. Nonetheless, most of the heat exchange of the low-temperature air stream occurs as the air jet leaves the vents and starts mixing with the cabin ambient before reaching the target passenger. A more efficient air jet can conserve its temperature as it travels through the cabin environment. The previously stated heat transfer mechanisms are highly non-uniform in space and time, contributing to enclosing the occupant inside a bubble of heterogeneous air temperature, which makes achieving thermal comfort a challenge.

1.2. Problem Statement

Traditional car air vents are often known to have a low aspect ratio (AR), meaning that their width is proportional to their height; circular and square vents are typical examples of these. While these vents can be nicely integrated into the vehicle decor, their point-like nature makes them unsuitable for providing a large coverage area on the occupant's body. To achieve near-uniform convection across the body, it becomes necessary to use several vents that are spread out or an array of adjacent outlets for sufficient coverage of each passenger. Additionally, air vents that are proud

and explicitly designed may be unappealing and detract from the otherwise uniform appearance of the vehicle's interior surfaces [17]. Designers and Engineers at Tesla are always concerned with creating functional and visually appealing interior components. One step towards achieving this is to conceal the most eye-catching elements of a car's interior, the air vents, and associated vanes. Most current air vents have comparable geometries and form factors; what distinguishes one is its appearance, pristinity, and efficiency; all can be achieved through a good understanding of jet aerodynamic principles. Tesla is realizing this by utilizing the vent design patented in [17]; this design hinges on the concept of momentum mixing to achieve airflow direction control while eliminating the use of mechanical steering vanes; the flow direction can rather be controlled through the vehicle's user interface (UI). This design comprises two jet outlets which together effectively form a twin-jet nozzle. The two jets are often oblique, allowing for a greater angle control range; this range's upper and lower limits are set by the bottom and top jet ejection angles, respectively. Vertical flow steering can be achieved by intercepting two air jets that combine and create a single jet before impinging on the targeted object. More details are provided in the following sections on the working principles of this concept. Figure 1.3 depicts a *xz*-section of the patented vent design installed on the vehicle's instrument panel, where the x-axis points from the front to the rear of the vehicle and the z-axis points from the vehicle's floor to roof. The section shows the instrument panel **602**, the upper and lower outlets of the vents labeled **606** and **608**, as well as the ducts leading to these outlets labeled **610** and **612**, respectively. As apparent in Figure 1.3, the lateral (side-to-side) airflow control across the vehicle is carried out using vanes that are installed upstream enough along the channel leading to the upper outlet to ensure the vanes' invisibility. Figure 1.4 shows a schematic of a simplified twin-jet nozzle configuration highlighting all the different geometric parameters (See *Nomenclature* for details)

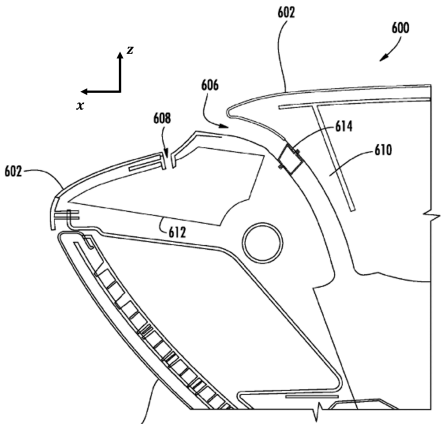

Figure 1.3: Tesla Airvent Patented Design [17]

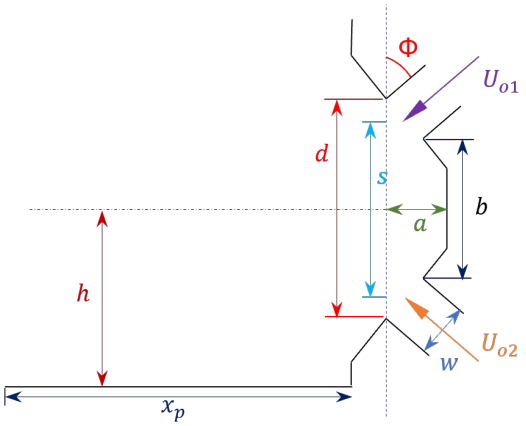

Figure 1.4: Confluent oblique twin offset jets

The minimalism of the Tesla air vent design incurs an efficiency cost, making intersecting twin jets' centerline velocity decay nearly twice as fast as their single jet counterparts. Additionally, the interaction between the jet and a surface close to the outlet hurts both the jet's convective heat transfer capability and controllability. Achieving cooling performance and controllability that is on par with existing conventional vents is currently a challenge that this study aims to alleviate.

As the offset distance between the centerline of the jet and a surface in the close vicinity

becomes smaller than a certain threshold, the forming jet tends to bend towards the surface until it attaches and travels along with it owning to a phenomenon known as the Coanda effect. In order to better design air vents of the previous configuration and the surrounding surfaces to both be optimal for aerodynamic performance and aesthetics, this behavior needs to be better understood and quantified.

1.3. Research Formulation

The research presented in this thesis is part of the development work carried out by the Aerothermal team at Tesla. The team aims to understand the underlying physics of high aspect ratio subsonic jets, particularly intersecting twin jets, to better control the vehicle's cabin climate. Although current Tesla production cars are already employing this concept for the air vents, the team still believes that the cooling capacity of these jets could be challenged for higher overall thermal system efficiency.

Research Objective

This thesis aims to investigate the physics represented by the mean and turbulence flow characteristics of high AR twin intersecting subsonic jets. Additionally, scrutinize the installation effect on the jet emanating from this nozzle configuration, focusing on the offset-height influence. Finally, identify a suitable RANS turbulence model to simulate this nozzle configuration and the installation effect accurately.

This objective is broken down into a number of research questions as follows,

Research Question 1

What is the influence of the installation surface on the twin jet characteristics?

1. Merging point, combined point, upper vortex point, lower vortex point, and reattachment point
2. Flow-field mean velocity, vorticity and TKE
3. The range where self-similarity takes place
4. The growth rate of the merged jet shear layers
5. The decay of the centerline velocity of the jet
6. The interaction between the two jets and between the combined jet and the wall

Research Question 2

How does the Coanda effect contribute to the loss of the jet's control authority of installed jets?

1. How does this contribution vary with the installation surface offset distance?
2. How can this contribution be reduced or mitigated?

Research Question 3

What is the most appropriate RANS turbulence model for simulating free and installed intersecting twin jets?

Research Hypothesis

The hypotheses addressed in this thesis are
(I) The efficiency of the jet is compromised by moving from a single jet to a twin intersecting jet that occupies the same outlet height
(II) The vertical controllability of intersecting twin jets is compromised by the presence of a surface within a certain offset distance range, and the effect of the surface becomes less significant for higher offset values. These hypotheses are to be confirmed by this research work

Research Methodology

The thesis workflow is comprised of two main components,
(I) Experimental Study:
Characterizing the evolution of large-scale flow structures in high AR (planar) confluent oblique twin offset jets at moderate Reynolds number experimentally using high-fidelity planar particle image velocimetry (PIV) in both installed and uninstalled conditions. Due to the high cost and set-up complexity of PIV systems, they are rarely used for industrial applications, making computational methods a more common tool in the engineering design process; this motivated utilizing TUDelft's facility for high-fidelity experimental data acquisition. The twin-jet flow characteristics and direction sensitivity to the installation surface offset are then studied by varying the offset distance.
(II) Computational Study:
Employing the experimental results to select, calibrate and validate the most appropriate RANS turbulence model for simulating intersecting jets and their installation surface interaction

1.4. Thesis Outline

This thesis report aims to establish the groundwork necessary to address the research questions at hand. To accomplish this, a comprehensive review of existing literature on subsonic turbulent jets is presented in Chapter 2, providing essential background information for the research. The literature review focuses on the research area of turbulent single subsonic free jets, dual jets, and offset jets, as these are particularly relevant to this thesis work. Additionally, this chapter aims to identify gaps in the literature to motivate the objective of the imminent thesis work. This chapter concludes by describing the nozzle configuration adopted throughout the research work.

In Chapter 3, the flow measurement technique utilized for conducting the experimental work is presented. The chapter begins by briefly overviewing the Particle Image Velocity (PIV) working principle. This is followed by describing the facility where the measurement campaign was carried out, including the test subject used. A detailed discussion of the test setup, calibration, and different parameters used for fine-tuning the measurement apparatus is presented. An overview of the measurement campaign and a rationale for the test matrix chosen to run the experiment is posed. The last section of this chapter covers the post-processing pipeline developed to extract parameters of interest from the raw experimental data, a description of each of these parameters, and their significance to the current investigation.

Chapter 4 focuses on the computational aspect of the research, outlining the setup utilized for simulations. The chapter commences by describing the geometry of the computational domain used for the simulations. It then proceeds to discuss CFD modeling and presents a concise explanation of selected high-order RANS turbulence models that are of particular interest in this study. Moreover, the model flow physics, model closure, boundary, and initial conditions are all discussed. The meshing strategy, solver convergence settings, and data extraction routine are also detailed. The chapter concludes by presenting the results obtained from various studies highlighting the sensitivity of CFD predictions for free-shear flows to various grid sizes and domain inlet turbulence intensities.

In Chapter 5, the experimental and computational investigation findings are presented and analyzed to address the research questions outlined in Chapter 1. The chapter is structured in a way that facilitates answering each research question. Firstly, the experimental data compares the flow field of free-standing intersecting jets across the design control range to their installed counterparts, providing insights into Research Question 1. Next, the influence of the installation surface's offset distance on the intersecting jet control range is closely examined to understand the features contributing to the range variation, answering Research Question 2. The third section of this chapter involves an assessment of four different RANS turbulence models to evaluate their ability to capture the physics of jet merging at different mass flow ratios. The solutions of each model are compared with PIV data to determine the best-performing model. The potential of the most-accurate turbulence model to predict the installation surface's impact on the jet control curve and the reattachment point is challenged, providing answers to Research Question 3.

Finally, Chapter 6 summarizes the current investigations' findings providing answers to the research questions posed. The chapter concludes with a few recommendations aimed at improving the execution of this thesis work and providing suggestions for future research. These recommendations are based on the insights gained from the study and to provide guidance for researchers interested in further exploring the topics covered in this work.

2

Theoretical Framework & Literature Review

This chapter presents an overview of turbulent, incompressible single jets. The conventional single jet governing equations, namely conservation of mass and momentum, are discussed in detail in Section 2.1. Furthermore, the chapter covers the jet structure and jet mean flow features of a 3D asymmetric free jet, including the maximum mean velocity decay, half-width growth, and jet entrainment. It is important to note that jet flows can be represented as two-dimensional flows under certain conditions. For instance, when the aspect ratio of an asymmetric nozzle with a rectangular cross-section is greater than 8, the centerline properties of the jet are minimally affected by edge effects [18]. In such cases, the nozzle can be assumed to be infinitely wide in the spanwise direction, allowing for statistically homogeneous turbulence behavior. However, for small aspect ratio jets, which have more evident edge effects on the jet shape and bulk characteristics, 3D treatment is required, making them more challenging to analyze. The review primarily focuses on 2D planar jets since the nozzles used in this study have an aspect ratio of $AR > 8$. Nonetheless, the chapter discusses the baseline scenario of a free single jet using a 3D rectangle jet to provide clarity.

2.1. Governing Equations

The fluid flow equations for free jets are derived from principles of mass, momentum, and energy conservation over an infinitesimal control volume. The three conservation laws, in conjunction with the equation of state (The ideal gas law, in this case), correlate the velocity vector field to the thermodynamic quantities (pressure p, density ρ, and temperature T). The continuity equation for a 3D jet reads as,

$$\frac{\partial \rho}{\partial t} + \frac{\partial u}{\partial x} + \frac{\partial v}{\partial y} + \frac{\partial w}{\partial z} = 0 \tag{2.1}$$

The conservation of momentum is described by the Navier-stokes equations as:

$$\frac{\partial u}{\partial t} + u\frac{\partial u}{\partial x} + v\frac{\partial u}{\partial y} + w\frac{\partial u}{\partial z} = -\frac{1}{\rho}\frac{\partial p}{\partial x} + \nu\left(\frac{\partial^2 u}{\partial x^2} + \frac{\partial^2 u}{\partial y^2} + \frac{\partial^2 u}{\partial z^2}\right) - \left(\frac{\partial \overline{u'^2}}{\partial x} + \frac{\partial \overline{u'v'}}{\partial y} + \frac{\partial \overline{u'w'}}{\partial z}\right) + f_x \tag{2.2}$$

$$\frac{\partial v}{\partial t} + u\frac{\partial v}{\partial x} + v\frac{\partial v}{\partial y} + w\frac{\partial v}{\partial z} = -\frac{1}{\rho}\frac{\partial p}{\partial y} + \nu\left(\frac{\partial^2 v}{\partial x^2} + \frac{\partial^2 v}{\partial y^2} + \frac{\partial^2 v}{\partial z^2}\right) - \left(\frac{\partial \overline{u'v'}}{\partial x} + \frac{\partial \overline{v'^2}}{\partial y} + \frac{\partial \overline{v'w'}}{\partial z}\right) + f_y \tag{2.3}$$

$$\frac{\partial w}{\partial t}+u\frac{\partial w}{\partial x}+v\frac{\partial w}{\partial y}+w\frac{\partial w}{\partial z}=-\frac{1}{\rho}\frac{\partial p}{\partial z}+\nu\left(\frac{\partial^2 w}{\partial x^2}+\frac{\partial^2 w}{\partial y^2}+\frac{\partial^2 w}{\partial z^2}\right)-\left(\frac{\partial\overline{u'w'}}{\partial x}+\frac{\partial\overline{v'w'}}{\partial y}+\frac{\partial\overline{w'^2}}{\partial z}\right)+f_z \tag{2.4}$$

where, as shown in Figure 2.1, the x-axis defines the axial direction of the jet, the z-axis is in the direction of the height of the nozzle (transverse), and the y-axis is the spanwise direction axis; u, v, and w are the turbulent mean velocity quantities, and u', v' and w' are the fluctuating velocities in the x, y, and z directions, respectively. p is the mean pressure at any point, ν is the kinematic viscosity, and ρ is the mass density of the fluid, t is the time variable and f is a term representing body forces. For simplicity, the mean flow can be assumed steady in time and two-dimensional (e.g for planar jets), which allows for simplifying the previous equations. The y-direction's mean and fluctuating velocity components v and v' and the time derivative $\frac{\partial}{t}$ all tend to zero for 2D steady axial jets. Additionally, assuming the jet issued into a large stagnant environment, the body forces acting on the jet can also be neglected. Further, since the transverse extent of the flow is small, u is generally much larger than the transverse velocity component w in a large portion of the jet, however the velocity and stress gradients in the z-direction are much larger than those in the x-direction. The previous considerations can simplify the continuity equation as follows

$$\cancel{\frac{\partial \rho}{\partial t}}+\frac{\partial u}{\partial x}+\cancel{\frac{\partial v}{\partial y}}+\frac{\partial w}{\partial z}=0\Longrightarrow\boxed{\frac{\partial u}{\partial x}+\frac{\partial w}{\partial z}=0} \tag{2.5}$$

While the v component of the momentum equation cancels to zero, the other two equations simplify to the following

$$u\frac{\partial u}{\partial x}+w\frac{\partial u}{\partial z}=-\frac{1}{\rho}\frac{\partial p}{\partial x}+\nu\frac{\partial^2 u}{\partial z^2}-\left(\frac{\partial\overline{u'^2}}{\partial x}+\frac{\partial\overline{u'w'}}{\partial z}\right) \tag{2.6}$$

$$0=-\frac{1}{\rho}\frac{\partial p}{\partial z}-\frac{\partial\overline{w'^2}}{\partial z} \tag{2.7}$$

Integrating (2.7) with respect to z from $z=0$ to a point outside the jet results in the following,

$$p=p_\infty-\rho\overline{w'^2} \tag{2.8}$$

where p_∞ is the ambient pressure. (2.6) can be rewritten after subbing (2.8) as,

$$u\frac{\partial u}{\partial x}+w\frac{\partial u}{\partial z}=-\frac{1}{\rho}\frac{dp_\infty}{dx}+\nu\frac{\partial^2 u}{\partial z^2}-\frac{\partial\overline{u'w'}}{\partial z}-\cancel{\frac{\partial}{\partial x}(\overline{u'^2}-\overline{w'^2})}\ \text{0, smaller than other terms} \tag{2.9}$$

The last two terms in (2.9) can be written as,

$$\nu\frac{\partial^2 u}{\partial z^2}-\frac{\partial\overline{u'w'}}{\partial z}=\frac{1}{\rho}\frac{\partial}{\partial z}\left(\mu\frac{\partial u}{\partial z}\right)+\frac{1}{\rho}\frac{\partial}{\partial z}(-\rho\overline{u'w'})=\frac{1}{\rho}\frac{\partial}{\partial z}\left(\underbrace{\mu\frac{\partial u}{\partial z}}_{\tau_{lam}}+\underbrace{-\rho\overline{u'w'}}_{\tau_{turb}}\right)\ \ll\tau_{turb},\ \text{no solid boundaries} \tag{2.10}$$

The pressure gradient in the axial direction is negligible, allowing simplifying (2.9) to its final form as follows,

$$\boxed{u\frac{\partial u}{\partial x}+w\frac{\partial u}{\partial z}=\frac{1}{\rho}\frac{\partial\tau_{turb}}{\partial z}} \tag{2.11}$$

This derivation shows the simplification accompanies the planar jet 2D, steadiness and incompressibility assumptions.

2.2. Single Jet Characteristics

2.2.1. Jet Flowfield Regions

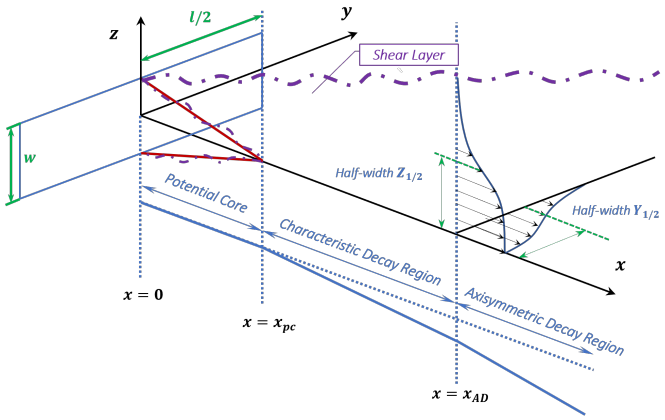

Figure 2.1: Flow Field Regions of a Single Subsonic Jet [19]

The traditional single-free jet dynamics are investigated to comprehend complex jet phenomena better. The pressure differential across the nozzle outlet caused by a pressure source upstream (e.g blower) excites the jet and releases it into the quiescent ambient. Upon exiting the nozzle, the jet flow interacts with the surrounding static ambient, forming a jet boundary layer due to the mismatch between the $U_o \neq 0$ jet and the $U_\infty = 0$ ambient; this boundary layer is referred to as the shear layer. This layer behaves as an interface between the jet's core and the surrounding fluid close to the nozzle outlet. As this layer develops, it carries particles of the surrounding ambient along its outer edge and slows down particles of the jet core along its inner edge leading to the thickening of this layer. Along the section of the velocity profile between the inner and outer edges of the shear layer exists an inflection point that triggers an instability known as Kelvin-Helmholtz instability. This instability induces roll-ups and streaky structures that together interact to form large-scale azimuthal vortices along the jet boundary layer. This instability promotes mass and momentum transfer between the jet and the surrounding fluid, increasing jet mixing and mass flow. The shear layers on both ends of a planar jet start thin at the nozzle outlet and gradually thicken until they intersect at the jet axis trapping between them a cone-shaped irrotational flow region known as the potential core. The length of the jet's potential core is determined by the size and the growth rate of the jet's shear layers. Trentacoste's early work in [19] classified the structure of an asymmetric jet originating from a sharp-edged nozzle into three main zones, as illustrated in Figure 2.1. The coordinate system convention shown in the schematic (and used henceforth unless otherwise mentioned) indicates that the origin of an asymmetric jet is at the centroid of the nozzle outlet, the positive x-axis is in the axial flow direction, the z-axis is in the direction of the smaller nozzle dimension (the minor axis), and the nozzle height and width are denoted by w and l, respectively. As the schematic indicates, the flow field of the jet comprises the following three regions:

The Potential Core (PC) region: The mixing initiated at the jet boundaries has not yet propagated across the entire jet height in this region, leaving a cone with a uniform axis velocity close to the jet exit velocity. As the name implies, this zone is distinguished by the potential or vorticity-free flow. The length of the potential core extends from $x = 0$ to a few jet nozzle diameters downstream (x_{PC}). This streamwise point corresponds to where the jet's mean centerline velocity U_c ceases to be constant and begins to decay. According to a study by Zaman et al., the length of the potential

core in a jet downstream of the nozzle outlet can vary up to 6.5 times the diameter of the jet, depending on the velocity profiles and turbulence levels at the nozzle exit [20].
The Characteristic Decay (CD) region: Right downstream of x_{PC} the potential core starts vanishing. The centerline velocity decay and symmetry plane velocity profiles vary with the orifice configuration. For 3D jets, this region is characterized by self-similar velocity profiles in the plane of the nozzle's minor axis, unlike the profiles in the plane of the major axis (y), which are not fully developed yet, hence non-self-similar. Therefore, as the name suggests, this region is deemed characteristic of the jet's initial geometry.
The Axisymmetric Decay (AD) region: The axis velocity decay in this region is axisymmetric. The overall jet shape tends to approach axisymmetry, making the jet flow oblivious to the nozzle geometry. In both symmetry planes, the velocity profiles in this region are self-similar and conform to Gortler's solution [21].

The distinct flow regions may also be explained by the innate tendency of fluid flows to adopt shapes that facilitate the flow of momentum. In the case of jet flows, momentum is transferred from the jet (the mover) to the quiescent surroundings (the non-mover). This transfer occurs through a process called mixing, where momentum moves perpendicular to the jet's boundary layer. To facilitate mixing, the jet cross-section tends to increase, allowing for a more efficient lateral flow of momentum and quicker mixing between the jet and the surroundings [22]. Consequently, the axial velocity of the fluid in the jet column declines rapidly as it mixes with the surrounding ambient. This uniform morphing of the jet in all directions occurs in the **AD** region, resulting in a rapid decline in centerline velocity. The work presented in [19], [23] confirm that the bulk characteristics and extent of the jet's potential core and characteristic regions (near-field) appear to be determined completely by orifice geometry (cross-section and aspect ratio) and that the flow in the axisymmetric decay (far-field) is oblivious of the nozzle geometry. The geometry dependency in the near field is attributed to the shear layer and mixing originating at the boundaries of the nozzle in the lateral (z direction). As the aspect ratio of the orifice approaches unity, the **CD** region degenerates into a transition region between the **PC** and **AD** regions, e.g., the square and axisymmetric jets. Numerous investigators have examined single rectangular jet flows; some of the earliest work carried out in [19] and [24] collected results for rectangular and "bluff" three-dimensional jets. The experimental data entails measurements at very large distances downstream, over 1000 slots widths, making it undoubtedly prone to higher uncertainty margins, however, the trends are still useful to look at. The bulk flow characteristics of single free jets and the influence of aspect ratio on these characteristics are discussed in upcoming sections.

2.2.2. Jet Velocity and Turbulence Intensity Profiles

A jet's velocity and turbulence intensity profiles depend on the nozzle geometry and upstream conditions. Starting with pipe flows, the lateral velocity profile of the flow changes from being rectangular for the irrotational pipe inlet flow to a parabolic shape as it develops. A fully developed flow is attained when the flow has traveled for a sufficient distance (more than the entrance length) through the pipe, allowing the boundary layer to merge. The fully developed laminar flow has a Hagen-Poiseuille parabolic velocity profile at lower Reynolds numbers. However, the velocity distribution of fully developed turbulent pipe flows at higher Reynolds numbers is more top-hat shaped with a concave top profile. The development of the lateral velocity profile of the pipe flow is shown in Figure 2.2. Assuming the flow leaves the pipe into a quiescent ambient, the larger velocity gradients towards the boundaries of a turbulent jet would trigger higher velocity shear between the jet and the near-static ambient air resulting in more aggressive velocity fluctuations,

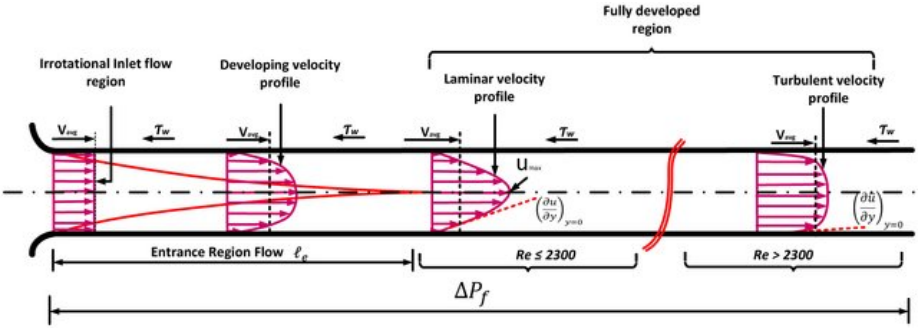

Figure 2.2: Schematic of Straight Pipe With Velocity Profiles at Different Development Stages [24]

K-H instability, and mixing. These fluctuations increase as the jet develops and becomes more turbulent. Figure 2.3 highlights the difference between the intensities of velocity fluctuation profiles of both a laminar and a turbulent round jets in the near-field reported in [25]. Asymmetric

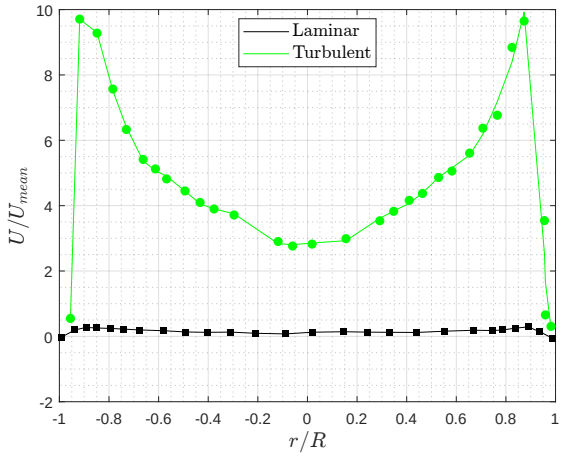

Figure 2.3: Velocity Fluctuation Profiles Across Turbulent vs Laminar Jets [25]

jets, such as rectangular ones, exhibit notable differences in both their mean and fluctuating velocity distributions compared to their symmetric counterparts in jets and pipe flows. In [26], Quinn presents 2D contour plots obtained through a hot-wire anemometry experiment on a sharp-edged rectangular slot with a 20 aspect ratio. The measurements were taken at various streamwise positions to investigate the jet's development. Unlike the axisymmetric jet, the rectangular jet exhibits two off-center velocity peaks at the nozzle outlet. Downstream measurements show that the jet stretches in the z direction and shrinks in the y direction, gradually transforming into a circular contour that aligns with earlier findings in the literature. This change in shape can be explained by the formation of a vortex ring as the rectangular jet exits the nozzle, which has a prescribed rectangular shape due to the slot's geometry. The non-uniform shape of the vortex ring results in non-uniform self-induction and hence deformation of the vortical structure and the jet's cross-sectional shape. Different hypotheses have been proposed to explain this phenomenon in [21] and [27]. The study's mean velocity and turbulence kinetic energy contours depict this behavior, as shown in Figure 2.4.

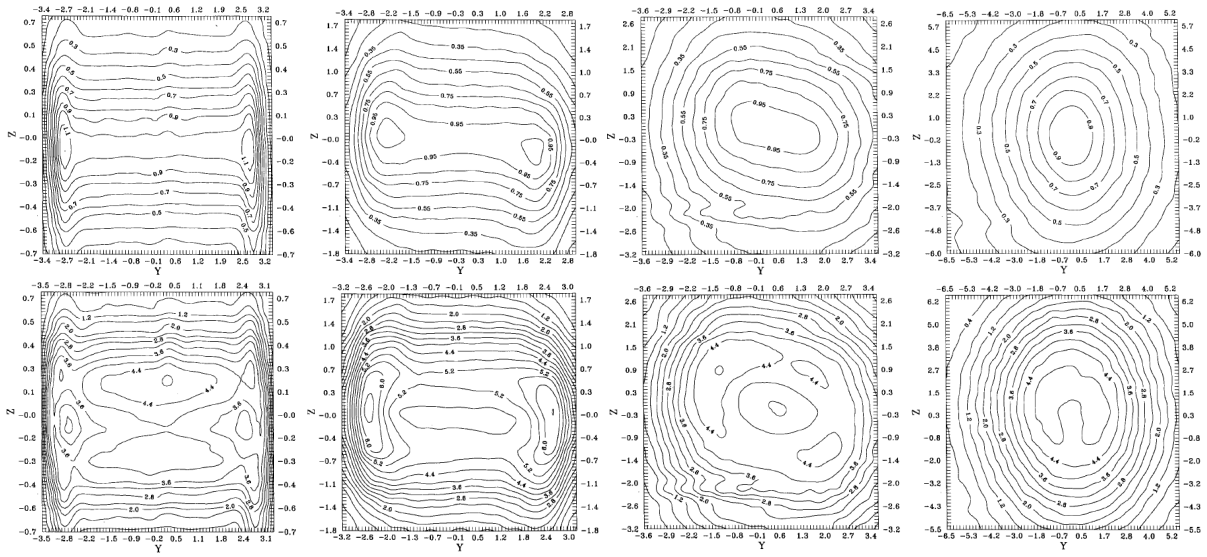

Figure 2.4: Mean Velocity Development Contour Plots (top) and TKE Development Contour Plots (bottom) [26]

2.2.3. Jet Centerline Velocity Decay

Jet characterization is essential, and one key metric is the maximum velocity at the jet's core and its decay rate as the jet progresses. The flow field of a jet, as shown in Figure 2.1, is divided into specific regions based on the centerline velocity decay rate. The locations of x_{PC} and x_{AD} are identified by the discontinuities in the velocity decay profile. The first discontinuity represents x_{PC}, and the second represents x_{AD}. In an experiment presented in [19], it is shown that the values of x_{PC} and x_{AD} depend on the initial half-width and half-length of the orifice in a relatively orderly fashion. Figure 2.5 demonstrates the sensitivity of centerline velocity decay to the nozzle outlet Eccentricity (e) (1/AR) and compares that to the centerline decay of an axisymmetric jet. The results show that the decay rate and extent of the **CD** and **PC** regions vary for jets of constant outlet area but different eccentricity. By closely observing Figure 2.5, it can be seen that the centerline

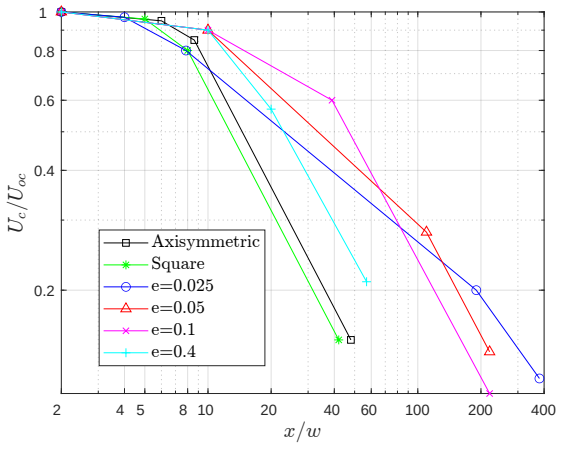

Figure 2.5: Centerline Velocity Decay Variation with Jet Eccentricity [19]

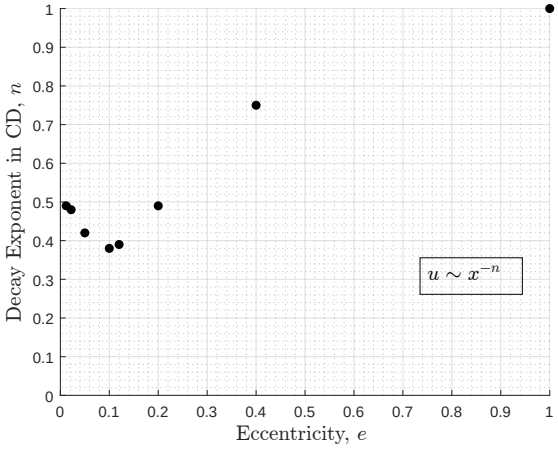

Figure 2.6: Characteristic Decay Exponent n Variation with Jet Eccentricity [19]

velocity is constant for a few nozzle diameters representing the potential core. In the **CD** region,

the centerline velocity decay becomes nonlinear and follows a power law ($U_c \sim x^{-n}$), where n varies as a function of jet eccentricity e as depicted in Figure 2.6. It is evident from this plot that the exponent n does not vary monotonically with the nozzle aspect ratio. A minimum is observed for the nozzle with an eccentricity value of 0.1, indicating the existence of a three-dimensional geometrical configuration that leads to the mildest rate of centerline velocity decay in the **CD** region. The same plot also shows that the axisymmetric (square) jet has the highest decay rate (highest n) in the **CD**. This aligns with the fact that the **CD** region vanishes for an axisymmetric jet [19]. Finally, the decay in the **AD** region becomes linear and, to a large extent, matches that of the axisymmetric jet downstream of the potential core irrespective of the nozzle eccentricity. Regression is used to fit the **AD** linear decay rate data by different researchers, and Quinn proposes the following relation in [26]

$$\frac{U_{oc}}{U_c} = K_u \left(\frac{x}{w} + C_u \right) \tag{2.12}$$

with $K_u = 0.182$ and $C_u = 0.456$ in the range of $28.67 \leq x/w \leq 62.58$. The results presented by Trentacoste in [19] imply a validation of Reynolds number similitude for three-dimensional jets in the foregoing results. In other words, the physical extent of the **CD** and **PC** regions of the various nozzle outlets are independent of their initial velocity (and thus exit Reynolds number condition), at least in the range of velocities where the flow can be deemed incompressible and turbulent.

2.2.4. Jet Half Width Growth Rate

Jets spread in two planes of symmetry: the xz and xy planes in confined jets or only the xz plane in planar jets, as shown in the schematic in Figure 2.1. Due to the challenge associated with determining the exact lateral location of the jet boundary as it develops, a more common way researchers use to quantify the spreading behavior of a jet is by monitoring its half-width growth. The jet half-width is defined as the y position (for xy plane spreading - major axis) or z position (for xz plane spreading - minor axis) at which the streamwise velocity equals half the jet centerline velocity at a particular streamwise location. The half-width is usually denoted by λ for the xy plane spreading and Λ for the xz plane spreading in literature. Experimental studies, such as those presented in [19] and [28], have investigated the jet half-width issuing from various aspect ratio sharp-edged rectangular nozzles. The results indicate that the half-width of the major axis (y) initially decreases while the half-width of the minor axis (z) grows.

Figure 2.7 presents an illustration of the growth profiles of λ and Λ for jets emanating from nozzles of 0.1 and 0.025 eccentricity. The plot depicts a crossover point where Λ surpasses λ at a certain distance from the nozzle outlet, a phenomenon referred to as axis-switching in the literature. This interchange of jet axes is known to be one of the main underlying mechanisms for vigorous entrainment in asymmetric jets. Notably, in confined jets (non-planar), the crossover point coincides with the transition from the **CD** region to the **AD** region. Previous studies, including the work in [29], [30], [27], and [26], have explored and quantified the phenomenon of axis-switching in rectangular and elliptic jets. Other studies have investigated the mechanisms underlying axis-switching and examined the impact of initial conditions, nozzle aspect ratio, and existing vortex dynamics on the deformation of jet cross-section [31], [32], [33]. In rectangular and elliptic jets, self-induced motion resulting from the non-uniform curvature of azimuthal vortex rings is thought to be the primary mechanism driving enhanced turbulence and, consequently, better momentum transport and axis-switching [30, 27, 33]. The presence of streamwise vortices due to upstream secondary flows can either favor or resist axis-switching, depending on their strength and orientation. Downstream of the cross-over point, the half-width profiles still grow with λ growing

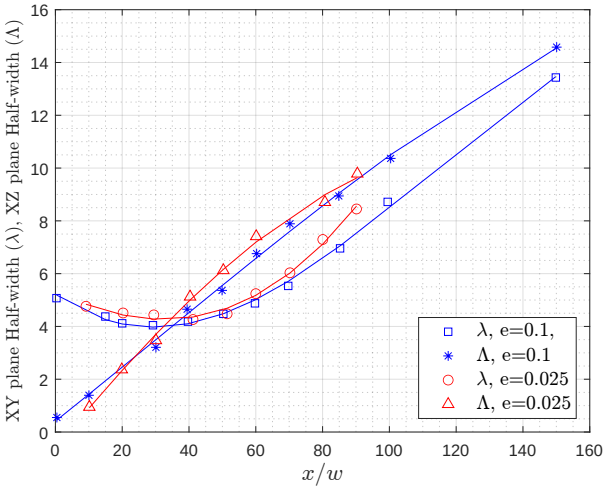

Figure 2.7: Half-width of Major (λ) and Minor (Λ) Axes for Rectangular Jets of Eccentricities $e = 0.1$ & $e = 0.025$ [19]

at a higher rate. However, the two curves tend to converge as the jet approaches axisymmetry further downstream from the nozzle exit.

2.2.5. Jet Entrainment Rate

The instability along the jet shear layer triggers mass and momentum transfer between the jet and the quiescent surrounding. The rate at which the transfer happens is an indication of the mixing efficiency of the jet. Experimental work is carried out in [19], [34], and [35] on quantifying the entrainment rates of three-dimensional and axisymmetric jets. Figure 2.8 and Figure 2.9 show the variation of the normalized mass entrainment and momentum entrainment, respectively, as a function of the axial distance x from the nozzle outlet. The entrainment rates reported are for an axisymmetric and a 0.1 aspect-ratio nozzle. It can be observed that the mass entrainment rate for the axisymmetric jet varies linearly with streamwise distance x but exhibits a change in slope at a point corresponding to the onset of axisymmetric decay at $x = 3$ [in] or where the **PC** region ends, and **AD** region starts. Mass entrainment rates for the slot of $e = 0.1$ were also found to vary linearly with x but at an initially higher rate than the axisymmetric jet. The mass entrainment rate then drops until a point where both the axisymmetric and $e = 0.1$ jet's mass entrainment rates become indistinguishable; this point corresponds to the onset of **AD** region for the asymmetric jet. The Mass entrainment rates reported in [34] are deemed to be Reynolds number dependent for $Re < 2.5 \times 10^4$. On the contrary, the data in Figure 2.9 shows a near-constant momentum entrainment throughout the jet column, which can be attributed to the fact that the jet is issuing into a large stagnant environment and expanding under zero pressure gradient due to the absence of external forces; this observation holds for different aspect ratio nozzles. This can be proven mathematically by multiplying the momentum equation (2.11) by ρ and integrating from $z = 0$ to $z = \infty$ as follow,

$$\rho \int_0^\infty u \frac{\partial u}{\partial x} dz + \rho \int_0^\infty w \frac{\partial u}{\partial z} dz = \int_0^\infty \frac{\partial \tau}{\partial z} dz \tag{2.13}$$

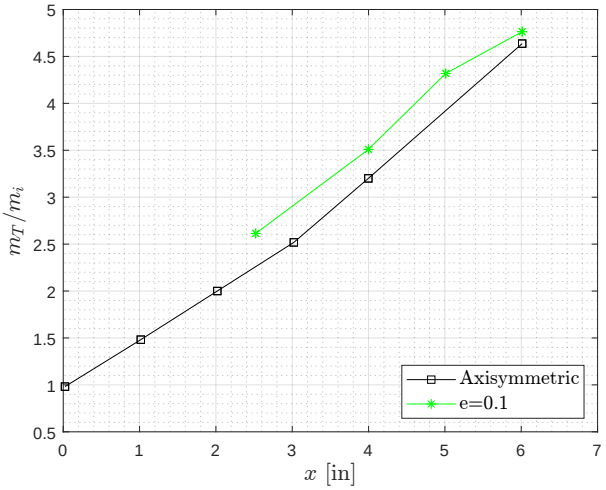

Figure 2.8: Mass Entrainment Streamwise Evolution For an Axisymmetric and a Rectangular Nozzle of $e = 0.1$ [19]

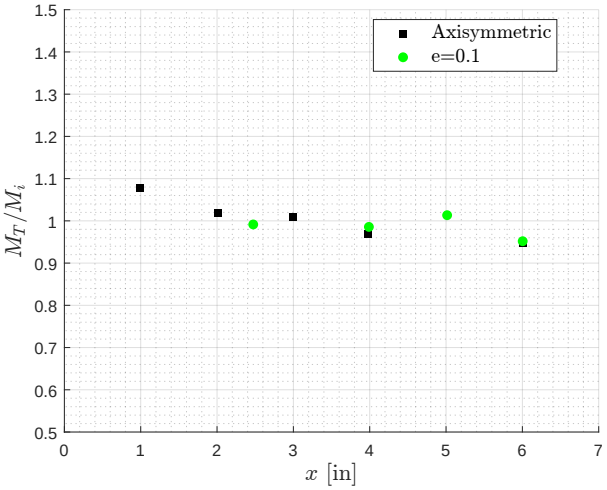

Figure 2.9: Momentum Entrainment Streamwise Evolution For an Axisymmetric and a Rectangular Nozzle of $e = 0.1$ [19]

The LHS terms of the equation above can be written as

$$\begin{aligned} &\Rightarrow \rho \int_0^\infty u\frac{\partial u}{\partial x}\,dz = \frac{1}{2}\int_0^\infty \frac{\partial}{\partial x}(\rho u^2)\,dz = \frac{1}{2}\frac{d}{dx}\int_0^\infty \rho u^2\,dz \\ &\Rightarrow \rho \int_0^\infty w\frac{\partial u}{\partial z}\,dz = \rho\left(|uw|_0^\infty - \int_0^\infty u\frac{\partial w}{\partial z}\,dz\right) = \rho\left(\int_0^\infty u\frac{\partial u}{\partial x}\,dz\right) \end{aligned} \tag{2.14}$$

since for $z = 0$; $u = U_c$, $w = 0$ and for $z \to \infty$; $u = 0$, $w = w_e$, where w_e is the entrainment velocity. Hence,

$$\rho \int_0^\infty w\frac{\partial u}{\partial z}\,dz = \frac{1}{2}\frac{d}{dx}\int_0^\infty \rho u^2\,dz \tag{2.15}$$

The LHS of (2.13) becomes as in (2.16), while the RHS of the same equation can be written as in (2.17). The two sides of the equation indicate that the rate of change of the momentum flux in the x-direction is zero or the moment flux in the x-direction is conserved.

$$\frac{d}{dx}\int_0^\infty \rho u^2\,dz \tag{2.16}$$

$$\int_0^\infty \frac{d\tau}{dz}\,dz = |\tau|_0^\infty = \underbrace{\tau(\infty)}_{=0,\text{symmetric jet}} - \underbrace{\tau(0)}_{=0} = 0 \tag{2.17}$$

When a jet is sliced, it becomes evident that both the mass and momentum vary laterally. Figure 2.11 presents the measured momentum entrainment ratio as a function of the normalized local axial velocity at various streamwise stations of the jet. The results show that 70% of the momentum is contained within the half-width of the jet, where $u/U_\circ = 0.5$. In contrast, Figure 2.10 displays the mass entrainment across the jet section at multiple streamwise locations. Unlike the momentum entrainment rate, the experiment shows a linear relationship between the entrained mass and the velocity ratio. Therefore, while a significant percentage of momentum is contained in the innermost "half," the same cannot be said for mass entrainment. This observation highlights the importance of the outer region of the jet for any streamwise station, as it contributes significantly to the total mass of the jet, just like the inner portion.

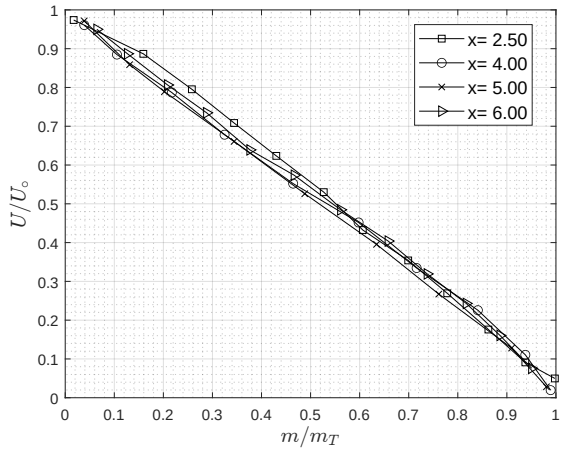

Figure 2.10: Mass Entrainment Ratio Across the Jet Diameter at Different Streamwise Positions [19]

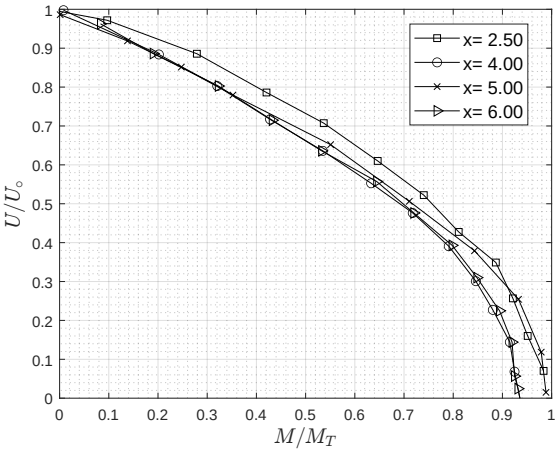

Figure 2.11: Momentum Entrainment Ratio Across the Jet Diameter at Different Streamwise Positions [19]

2.3. Free Turbulent Subsonic Twin Jets

Multiple-nozzle flows are often used in engineering applications, such as HVAC systems, fuel injectors, and mixing chambers, to increase mass flow rates and improve fluid mixing. However, as the jets issuing from these nozzles develop downstream of the exit plane, they interact with each other, resulting in a significantly more complex shear flow pattern than a single free jet. Despite their practical importance, the available literature on twin-jet interaction is limited compared to that on single jets, leading to an inadequate understanding of this subject. In fact, most of the available literature on this topic consists of systematic and parametric studies, which necessitates that this section adheres to the same structure. This section begins by examining the fundamentals of free twin jets, covering both parallel and intersecting free jets, before delving into the literature on the impact of geometric parameters on each.

Figure 2.12 shows a typical schematic of two parallel jets. Similar to the convention presented in Figure 1.4, the center-to-center spacing between the nozzle outlets is denoted by s, and the width of each outlet is denoted by w. In this setup, the streamwise and lateral (minor axis) directions are denoted by x, and y, respectively, with the nozzle origin being on the symmetry plane bisecting the spacing distance s between the two outlets. A two-dimensional twin-jet is formed when two parallel, incompressible, turbulent air jets are discharged into a quiescent surrounding at a velocity $U_\circ$ and at an equal offset from the centerline. As the jets exit the nozzle, air entrainment through the free boundary between the jets creates a sub-atmospheric pressure zone close to the nozzle spacing surface. This low-pressure zone, coupled with the spreading of the inner shear layers, causes the individual jets to curve towards each other, forming the converging region. As a consequence, the inner shear layers of the two jets meet at the so-called "merging point" (**mp**) located on the symmetry line of symmetric jets. **mp** is where the mean streamwise velocity, on the x-axis, equals zero. The distance from the nozzle exit to the **mp** is commonly used to define the length of the converging region. In the converging region, the spread of the inner and outer shear layers at a given streamwise location is measured using the half-velocity width, defined as the distance from the symmetry line to the position where the mean velocity is one-half the local maximum. This convention slightly differs from the one used in the case of single free jets discussion earlier, where the half-width is measured from the centerline of the individual jet itself. As shown in Figure 2.12,

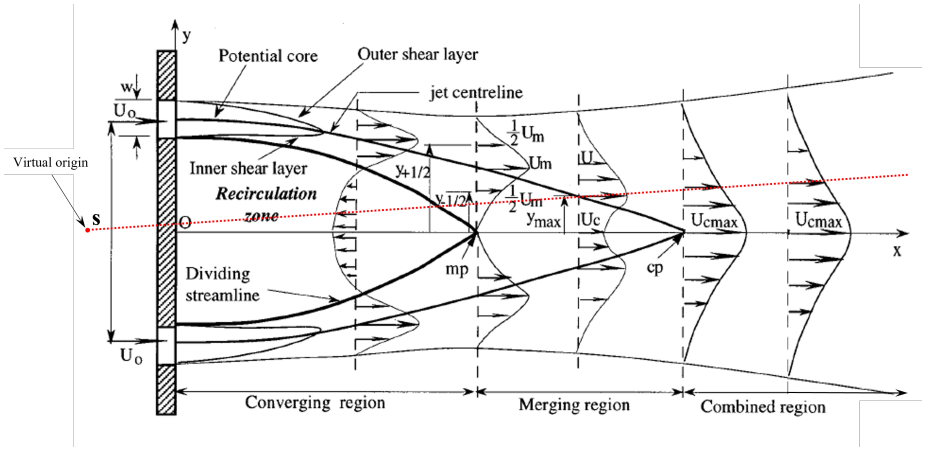

Figure 2.12: Parallel Planar Jets Schematic[36]

for the inner and outer shear layers of the individual jets, the half-velocity width in the converging region is denoted by $y_{-1/2}$ and $y_{+1/2}$, respectively.

Downstream of the **mp**, the inner counter-rotating vortical structures of the top and bottom jet boundaries interact. To compensate for the momentum deficit between the jets, the trajectories of the jets' centerlines bend towards the nozzle centerline. The lateral profile of the mean streamwise velocity transitions from a dual-peak to a single-peak shape downstream of the **mp**. The exact streamwise location where the single-peak pattern appears in the mean velocity profile of the merged twin jets is referred to as the "combined point" (**cp**); the region between the **mp** and the **cp** is referred to as the merging region. **cp** is where the mean streamwise velocity on the x-axis (U_c) reaches its maximum value (U_{cmax}). Downstream of the **cp**, the characteristics of the single-peaked velocity profile become increasingly similar to those of the self-similar single jet appearing in the characteristic decay region. One can expect higher-order (second order and above) turbulence statistics to continue developing and eventually show a full resemblance to a self-similar single jet further downstream [36].

2.3.1. Free Parallel Twin Jets

Research on two-dimensional twin jets has attracted considerable attention in the fields of combustion and fluidics. Among the early investigations of twin jets, Miller et al. [37] conducted experiments on momentum fields for dual jets. They compared twin parallel jets with a single free jet in the near and far fields and found that the core of each pre-merged jet through the twin jet's converging region is similar to that of a single free jet. However, the flow in the combined region exhibits all the characteristics of a single free jet except for the self-preservation of turbulence characteristics, which is attributed to the inconsistency in the upstream conditions.

In order to better understand the similarity between the far-field region of twin jets and single jets, researchers in [38] conducted a study comparing the nature of the region downstream of the **cp** for a bounded parallel twin jet with nozzle spacing of $s = 12.5$ to a single jet. Although the velocity profiles of the combined and single jets were found to be similar in the experiment, complete similarity was not reported until $120w$ downstream. Moreover, the mean centerline velocity decay profiles of the two jets were found to match to a high extent, except that the velocity magnitude for the parallel jets was higher. Additionally, the jet half-width was reported as a linear function with a spreading rate slightly lower than that of the single jet; Elbanna attributed this to

the streaming effect of the entrainment fluid, dependent on the nozzle spacing and bounding plate dimensions. As summarized in Table A.1, a great deal of research has investigated two parallel plane jets using point-wise measurement techniques, including HWA and LDA; it was not until the end of the 20th century that researchers could resolve the entire flow field and capture the transient spatial structures of parallel jets using numerical methods [39]. Subsequently, Particle Image Velocimetry (PIV), a high-resolution measurement technique, was used to quantify and visualize the flow field. The first PIV experiment conducted on parallel twin jets is presented in the work of Fujisawa [40].

Similar to single jets, the main metrics to consider when characterizing a merging jet are the mixing efficiency represented by the spreading rate (half-width growth rate (λ)), the velocity at the **cp** (corresponds to the maximum velocity along the centerline) and the decay rate of this maximum velocity. As previously discussed, twin jets effectively behave similarly to single jets once the merging process is complete. This observation makes understanding the virtual origin ($x_\circ$) and spread rate of this equivalent single jet essential. Early literature by Tanaka in [41] claims that the virtual origin ($x_\circ$) of an equivalent single jet can be found by intersecting the nozzle centerline with a line passing through the half-width locations downstream of the **cp** as depicted by the red line in Figure 2.12; this convention is then employed by later literature. The mixing and turbulent characteristics of twin jets, which determine the previously mentioned metrics, strongly depend on geometric and flow features such as the spacing distance between the two outlets (s) and the outlet velocity ratio (r). Subsections to follow discuss the impact of these parameters on twin merging jets.

I. Outlet Spacing Effect on mp and cp Locations

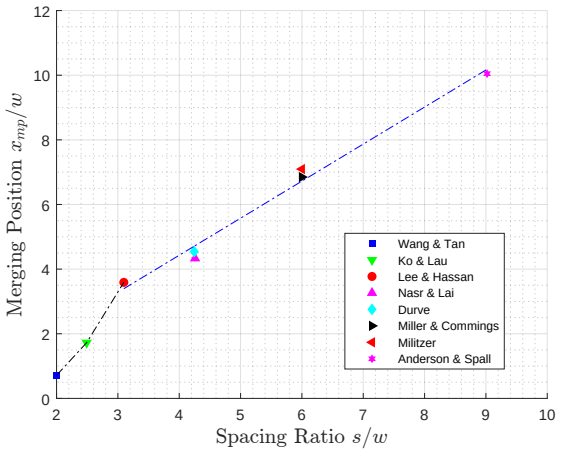

Figure 2.13: Merging Point Locations for Different Spacing Ratios [42]

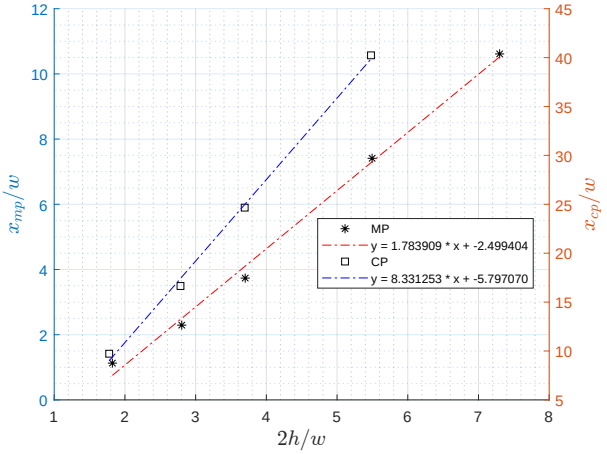

Figure 2.14: Combined and Merging Point Location for Different Spacing Ratios [42]

Saya Lee et al., investigated the flow field of twin parallel plane jets near the merging point for $s/w = 3.07$ at $Re_w = 4900$ using PIV in [42]. This manuscript summarizes previous experimental studies performed on twin parallel plane jets with spacing ratios $s/w < 10$. Based on a compilation of available literature data, Lee and Hassan suggested two trends for the location of the merging point with respect to nozzle spacing as shown in Figure 2.13. For $s/w < 3$, a nonlinear correlation between the merging point and nozzle spacing was observed. For nozzle spacing ratios $s/w > 3$, a merging point location linearly varied with the spacing ratio at a slope of 1.15. In the potential core region, each of the individual jets typically maintains a straight direction normal to the outlet

plane. This indicates that the onset of the jet merging is governed by the interaction between the shear layers, rather than the curvature, of the closely spaced jets resulting in a nonlinear variation of the merging point location with small nozzle spacing s/w. A similar observation was made by Naseri in [43], who realized that increasing the nozzle spacing ratio resulted in a linear increase in the locations of the merging and the combined points through a PIV experiment comprising setups with spacing ratios s/w = 3, 4.5, 6, 9 and 12 at a fixed Reynolds number of $Re_w = 6000$. While the **mp** location is a function of both nozzle spacing and the jet spread rate (i.e., jet exit conditions), the location of the **cp** is found to be a function of just the spacing ratio for jets with velocity ratio $r = 1$. The **cp** location is also shown to be more sensitive to the spacing ratio than its **mp** counterpart; this is evident by the slopes of the experimental data fitting shown in Figure 2.14. The trajectory of the individual jets' centerline is shown in [44] to be on the arc of a circle with a radius that is a function of nozzle spacing for large spacing ratios. The literature claims that for $s/w < 16$, the converging region is typically short enough that the jets are still developing; therefore, high velocities with large gradients are expected. In this spacing range, the negative pressure region between the jets mainly depends on the discharged jets' dynamic pressure. As a result, the curvature of the jets is not a function of the spacing between the nozzles but rather the jet exit conditions.

II. Outlet Spacing Effect on Momentum Flux

The momentum principle states that, for a selected control volume, the rate of change in momentum flux equals the sum of the forces acting on the control volume. For steady state conditions, the total momentum can be expressed as the sum of the momentum flux integral J_u , pressure integral P and turbulence fluctuations integral J_t as in (2.18). This sum should be conserved at any streamwise position downstream of nozzle as shown in Figure 2.15. The momentum integral can be broken down into its components as follows,

$$J_{total}/J = J_u/J + P/J + J_t/J \tag{2.18}$$

where:

$$J_u = \rho \int_{-\infty}^{\infty} u^2 dy, \qquad P = \int_{-\infty}^{\infty} p dy, \qquad J_t = \rho \int_{-\infty}^{\infty} u'^2 dy, \qquad J = \rho U_o^2 v \tag{2.19}$$

Tanaka in [41] affirms through experiment that the momentum flux integral J_u is constant for single jets and combined jets with spacing ratio $< s/w = 8.5$, as the spacing ratio increases beyond 8.5, J_u decreases. This reduction in momentum flux is attributed to the pressure recovery from negative to atmospheric pressure. As mentioned earlier, the pressure gradient across the merging point becomes more pronounced as the spacing increases making the pressure recovery more substantial; for that, the momentum flux needs to drop to maintain a constant J_{total}. The variation of the momentum integral components for a parallel twin jet with a spacing ratio of 20 is shown in Figure 2.15. Moreover, Tanaka et al. noticed that the constant value J_{total} drops as the outlet spacing distance increases; the numerical study in [45] validated this finding. The integral constant for the largest spacing ratio is realized to be 15% lower than the smallest spacing ratio. This observation is not surprising as the interaction of twin jets is a dynamic and nonlinear process, accompanied by enhanced turbulent mixing of momentums and increased viscous dissipation. As nozzle spacing decreases, more intense interactions are expected, hence a more pronounced total momentum integral constant.

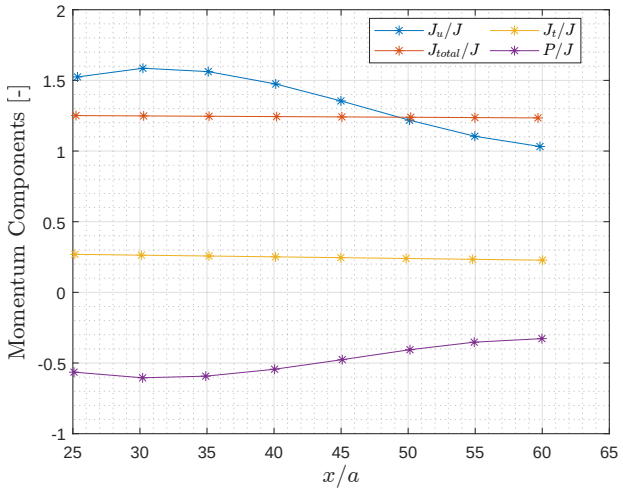

Figure 2.15: Momentum Components Evolution for Outlet Spacing Ratio $s/w = 20$ [41]

III. Outlet Spacing Effect on Centerline Velocity Decay and Spreading

In an effort to understand the influence of the jet outlet spacing on the merging jet bulk flow, the work presented in [44] and [41], as shown in Table A.1, was among the first to experimentally investigated the variation in the flow characteristics of the near-field region of twin parallel plane jets with changing the nozzle spacing. Spacing ratios of $8.5 \leq s/w \leq 26.5$ were tested across a Reynolds number range of ($4290 \leq Re_w \leq 8750$) using HWA. The experimental results show that the location of the maximum pressure and the magnitude of the maximum mean streamwise velocity along the symmetry line were independent of Reynolds number. Figure 2.16 reports the variation of the centerline velocity decay for the parallel twin jets of different spacing ratios. The literature shows that the centerline velocity along the streamwise axis (x-axis) decays proportional to $(x+x_o)^{-m}$ where m is the decay exponent, x_o is the virtual origin location and x is the streamwise location. The experimental results show that the decay exponent value is independent of the spacing ratio for $s/w < 8.5$, has a constant value, and becomes more pronounced beyond $s/w = 12$ as shown in (2.20). Similarly, the virtual origin is found to be independent of the spacing ratio for $s/w < 8$ is always 10.6w, however it becomes dependent on the spacing ratio at $s/w > 12$ as shown in (2.3.1.3).

$$m = \begin{cases} 0.5 & \text{s/w< 8.5} \\ 0.055\,(s/w) & \text{s/w>12} \end{cases} \qquad (2.20)$$

$$x_o/w = \begin{cases} 10.6 & \text{s/w< 8.5} \\ 0.055\,(s) & \text{s/w>12} \end{cases} \qquad (2.21)$$

In [41], Tanaka also investigated the impact of the spacing ratio on the jet spreading rate by reporting the half-width growth quantities for combined jets as a function of the spacing ratio. The presented results show that increasing the spacing ratio increases the slope of the half-width growth, which can be attributed to the virtual origin position as well as the prolongation of the converging zone as the merging point shifts downstream. The manuscript shows that the normalized virtual origin varies with spacing as follows, indicating that the virtual origin recesses proportionally as the spacing increases.

The responses of the velocity decay rate and the half-width growth to the change in the spacing ratio are depicted in Figure 2.16 and Figure 2.17, respectively. The characteristics of a single jet are also presented on the same plots for reference.

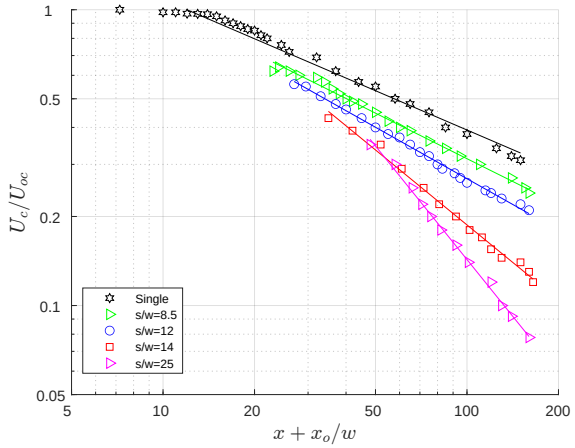

Figure 2.16: Effect of Outlet Spacing on Centerline Velocity Decay Along the Axis of Twin Parallel Jets [41]

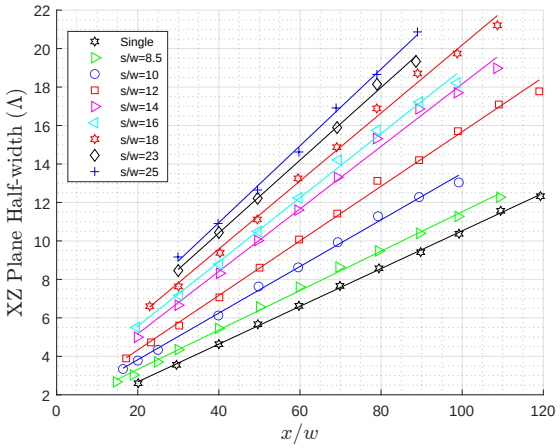

Figure 2.17: Effect of Outlet Spacing on Half-width Growth of Twin Parallel Jets [41]

Regardless of the spacing ratio range, the author claims that the max centerline velocity U_m decreases with increasing the spacing distance as $U_{cmax}/U_\circ = 1.96(s/w)^{-0.5}$. The decay rate of the maximum velocity, evaluated for a streamwise extent of $0 < x/w < 15$, was higher for the twin jets than for its single jet counterpart, and the disparity between the observed decay rate for the twin jets and single jet increases with an increase in nozzle spacing conforming with the exponent values in (2.20). However, the same study's results revealed that for a spacing ratio $s/w > 16$, the decay rate no longer depends on the nozzle spacing ratio.

IV. Outlet Spacing Effect on Jet Stability

The work in [37] presents a fundamental study on the surrounding fluid entrainment by the discharged turbulent flow of dual jet flow. In this paper, Miller and Coming explain that the entrainment is a consequence of the growth of the jet mixing layers downstream of the nozzle outlets. As the ambient air trapped between the two emanating jets gets entrained, a region of sub-atmospheric pressure zone is formed between the two jets and downstream of the spacing surface, which leads to the deflection of the jets towards one another. A few nozzle diameters downstream exists a region of super-atmospheric pressure due to the merge of the two jets (stagnation point). The aggressive pressure gradient across the stagnation point results in nonlinear fluctuations of the merging jet in streamwise and lateral directions. This nonlinearity triggers jet instability, which increases the pressure gradient across the stagnation point. As stable jets are often desirable, it is essential to understand the dynamics of the recirculations within the converging region to mitigate instabilities. As presented in [46], the converging region comprises two counter-rotating tandem vortex cores located in the recirculation region depicted in Figure 2.12. The top clockwise rotating vortex is formed due to the shear between the upper jet and the reverse flow emanating from the **mp**, and the bottom counter-clockwise rotating vortex is formed due to the lower jet and the reverse flow emanating from the **mp**. The steadiness of the vortex core centers controls the converging region's and, in turn, the merging jet's stability. Parallel plane and offset jets are contrasted in an intriguing analogy offered in [36]. In offset jets, flow exits a single nozzle parallel to an offset wall tangent to the jet centerline. Nasr et al. suggest that the symmetry plane between two parallel plane jets may seem to affect the flow field, similar to how a solid wall might affect a reattaching offset jet. Offset jets are addressed in more detail in Section 2.4. This research has

indicated that the recirculation zone for parallel jets is substantially smaller than that of offset jets. In contrast, the parallel jets' turbulence generation in the recirculation zone is much higher.

V. Velocity Ratio Effect

The first attempt to experimentally study the effect of the velocity ratio (r) of two parallel jets on the jet flow field is conducted by Elbanna in [47] using Hot Wire Anemometry (HWA). This investigation is achieved by fixing the discharging velocity of one jet and reducing that of the other. The experiment is conducted for velocity ratios of 0.25, 0.5, and 1. The same study is replicated numerically in [46]. The effect of velocity ratio r on the mixing of two parallel jets can be observed from Figure 2.18, which shows the jet centerline trajectories for the velocity ratios range of $[0.25-1]$. For $r \neq 1$, the weaker jet (with lower outlet velocity) is deflected towards the power jet (with higher outlet velocity). This deflection can be attributed to the different pressure gradients experienced by the two jets. Due to stronger jet boundary shear, the faster velocity jet entrains more surrounding fluid; more flow entrainment leads to a larger pressure decrease in the area of the power jet border. In the converging region between the two jets, the rate of entrainment

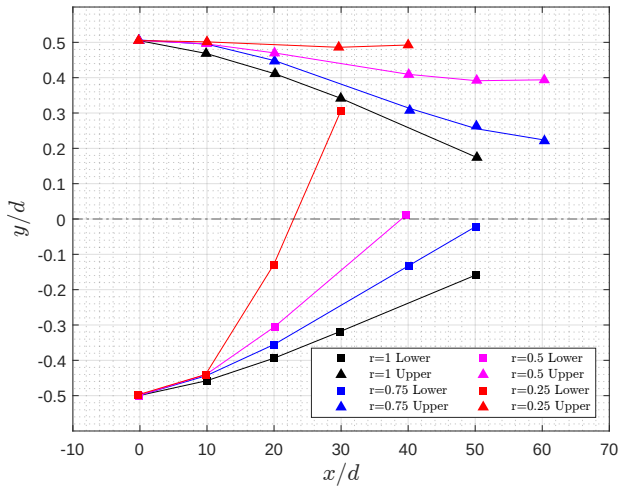

Figure 2.18: Trajectory of Adjacent Non-equal Jets' Centerlines [47]

and hence the suction become substantial. However, the pressure gradient experienced by the stronger jet across its boundaries, in the lateral direction, is smaller than that experienced by the weaker jet, which causes the weaker jet to deflect towards the stronger jet. Consequentially, for $r \neq 1$, the merge point is displaced not only in the streamwise direction but also laterally. The merge point for $r \neq 1$ shifted upstream, indicating that the mixing between the jets of unequal velocities starts early compared to jets of equal velocities.

Table 2.1: Effect of Spacing and Velocity Ratio on the Location of Merge Point and Combined Points [46]

2h/w	Y_{mp}/d (r=1)	Y_{mp}/d ($r \neq 1$)	X_{mp}/d (r=1)	X_{mp}/d ($r \neq 1$)	X_{cp}/d (r=1)	X_{cp}/d ($r \neq 1$)
9	0	-2.15	11.5	7.9	17.95	17.32
13	0	-3.54	14.9	11.8	22.84	20.47
18.25	0	-5.81	18.7	14	27	26.63

In the same manuscript, the effect of jet spacing ratio on the merge point location for equal ($r = 1$) and unequal ($r = 0.25$) outlet velocity ratios is investigated and summarized in Table 2.1.

For $r = 1$, the merge point always occurs along the plane of symmetry. For $r \neq 1$, the increase in the jet spacing causes the merge point to shift towards the stronger jet. The combined point for $r \neq 1$ was identified by plotting the lateral distribution of the axial velocity at different axial locations beyond the merge point. The point where velocity profiles begin to resemble the profiles of a single jet can be considered the combined point. The author also reported the effect of jet spacing on the combined point for $r = 1$ and $r \neq 1$. For $r \neq 1$ it can be observed that even though the merge points occur earlier axially, the combined point occurs at approximately the same location as that for $r = 1$. This is because, at the merge point of jets with $r \neq 1$, the pressure is lower as compared to $r = 1$. As a result, the velocities and the mixing rate in the merging region of $r \neq 1$ are lower. Thus, it can be said that the jets with $r \neq 1$ require a longer time to mix than $r = 1$. Regardless of the velocity ratio among the two outlets, it is evident that the negative static pressure is consistently occurring upstream of the merging region, while the highest pressure is developed in the merging region. In the absence of the wall shear stress effects, the total momentum is constant at each cross section along the two interacting jets independently of the velocity ratio and spacing, and the momentum conservation principle holds.

2.3.2. Free Intersecting Twin Jets

In the following years, researchers devoted more attention to confluent jets as more applications began employing the twin jets to accomplish directionality and jet characteristics control that is unachievable with single jets. This is accomplished by altering the number of jets emitted from the nozzles and their relative orientations. The twin oblique jet nozzle is one of the simplest examples of confluent jets. Figure 2.12 depicts an intersecting twin jet with a discharge angle of 90°, resulting in a parallel flow of the jet streams as opposed to a partially impinging flow. Similar to merging parallel jets, the negative-pressure zone between the originating jets drives the confluent jets to deflect toward each other until they converge and merge into a single jet.

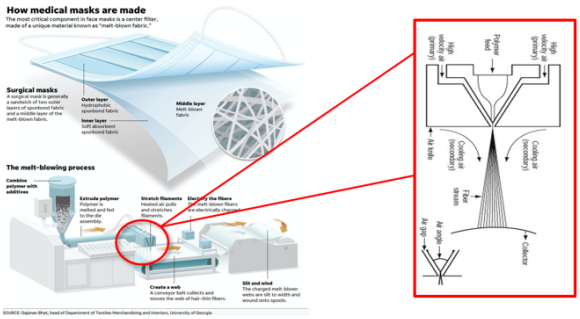

Figure 2.19: Melt Blowing Process Schematic [1]

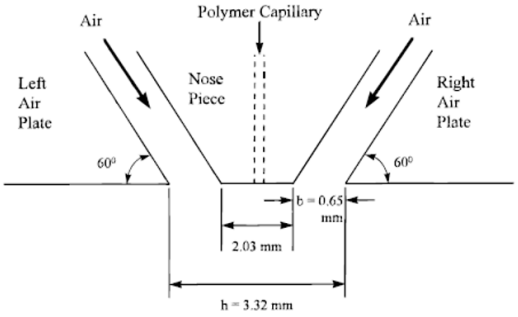

Figure 2.20: Example of an Intersecting Twin Jet Setup [48]

Elbanna et al. in [49] and [50], detail some of the earliest experimental investigations of the collision of two two-dimensional jets. Experiments including HWA and measurements of mean velocity, turbulence intensities, and Reynolds shear stress were conducted in this work. Similar to the free parallel twin jets, the study indicates that the mutual entrainment of the surrounding air by the free-standing intercepting jets generates a sub-atmospheric area between the two jets, which causes the jets to combine upstream of their geometric interception point. In accordance

[1] Gajahan Bhat, head of Department of Textiles Merchandising and Interiors, University of Georgia

with the literature on parallel twin jets, another finding of the same study is that the merged jet behaves as a single jet downstream of the merging region. When the two jets exit their respective channels at different velocities, the combined jet's centerline is angled away from the nozzle's symmetry line. In this instance, the centerline deviation is caused by both the power jet suction and the momentum orientations of the individual jets. In the same study, Elbanna demonstrates that the jet deflection angle can be described analytically as (2.22), where α is the angle between the incident velocity vectors, γ is the angle between the merged jet and the weaker jet, U_{o1} and U_{o2} are the discharge velocity centerline vectors, respectively, and U_c is the vector representing the centerline of the merged jet, as depicted in Figure 2.21. Figure 2.22 depicts a sample profile of angle change with velocity ratio for a configuration with 45° discharge angle outlets ($\alpha = 90°$).

$$\gamma = \cot^{-1}\left[\cot\alpha + \left(\frac{U_{o2}}{U_{o1}}\right)^2 \frac{1}{\sin\alpha}\right] \tag{2.22}$$

Towards the end of the 1990s, a procedure known as Melt Blowing was adopted for fiber production.

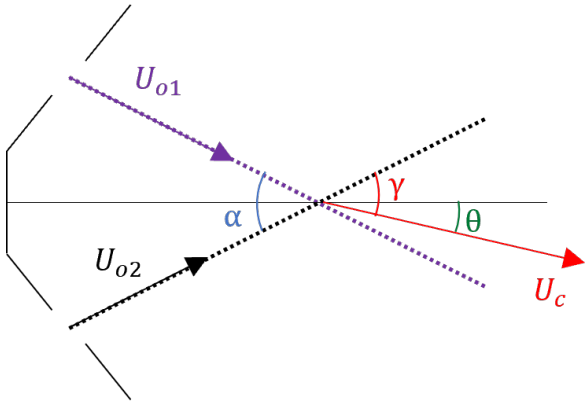

Figure 2.21: Jet Angle Variation Schematic

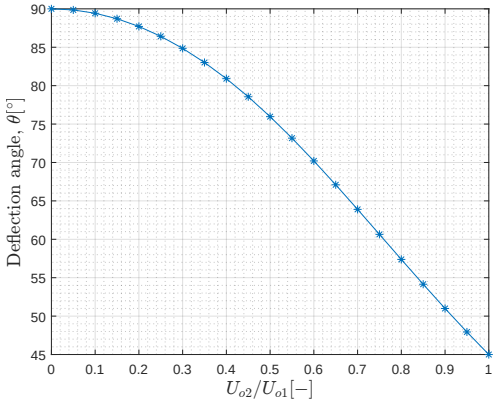

Figure 2.22: Jet Angle Variation with Velocity Ratio

Melt blowing is a single-step process used to generate fibers from a polymer melt. As shown in Figure 2.19, the resin material is pushed through a fine capillary positioned at the geometric center of the nozzle and immediately struck by two relatively high-velocity hot air jets of elevated temperatures. The polymer is then promptly attenuated into the fibers and laid over the collection screen. The widespread use of this technology in manufacturing prompted researchers to dig deeper into intersecting jets resulting in a fairly rich pool of literature. The aspect ratio of the nozzles used in this process is typically greater than fifty [51]. Hence most research work targeting this application tends to be two-dimensional. The two-dimensionality of this configuration motivated the author to consult the literature on the subject to elucidate the behavior of colliding jets under various conditions.

Harpham, in[48], is among the first to attempt to experimentally examine the flow field beneath twin intersecting jet nozzles using the arrangement seen in Figure 2.20 at a discharge angle of $\alpha = 60°$ and centerline-to-centerline distance ratio of about $s/w = 4$. The nozzle utilized in the studies has a "flush blunt nose," which refers to the flat spacing surface between the outlets on the same plane as the outlets as demonstrated by Figure 2.20. This study is foundational to the rest of the literature on intersecting nozzles for Melt Blowing application, therefore, used by the author to treat intersecting jet characteristics in detail in this section. Figure 2.23's black curves illustrate the

evolution of the near-field velocity profile for the 60° blunt-nose nozzle. At $x = 0.25\,\text{mm}$, where there are two separate peaks, a behavior resembling that of parallel jets is observed. For greater x distances ($x > 2.5\,\text{mm}$), the two peaks combine into a single peak with a maximum centerline velocity of around $1.3U_o$, corresponding to the combined point **cp**. Figure 2.24 demonstrates that once the two velocity peaks combine, the dimensionless velocity profile becomes self-similar and independent of the nozzle geometry parameters, as demonstrated by Harpham et al. Both equations proposed in [52] and [24] are used to fit the non-dimensional velocity profile, with Bradbury's equation providing a superior fit. Figure 2.25 demonstrates the centerline velocity decay of the examined setup near-field x-positions. Similar to parallel jets, the velocity increases as the distance downstream increases, peaks, and then drops again further from the combined points. The same study found that the non-dimensionalized half-width growth for a jet with a blunt tip intersecting at 60° could be represented using the following linear relation.

$$\frac{\lambda}{d} = k_1 \left[\frac{x}{d} + k_2\right] \qquad \text{where;} \quad k_2 = -\frac{x_o}{d} \tag{2.23}$$

Figure 2.26 depicts the least-squares best fit of (2.23) to the data, shown by the solid lines. The calculated values for k_1 and k_2 for the 60° blunt-nose nozzle are 0.118 and 1.05, respectively, and the R2 of the fit is 0.990. According to [48], these k_1 and k_2 values are extremely close to those predicted for a single rectangular jet with a slot width of d. According to research conducted on melt blowing with dual slots, the outlet spacing, the discharge angle of dual slots, the surface recession, and the nose sharpness (zero outlet spacing) are all key criteria that substantially impact the bulk flow characteristics. The findings of the preceding parameter studies on the merging jet characteristics are reported in the following subsections. The effect of outlet spacing is expected to be similar to that of parallel jets, for this reason, it is skipped in the upcoming discussion.

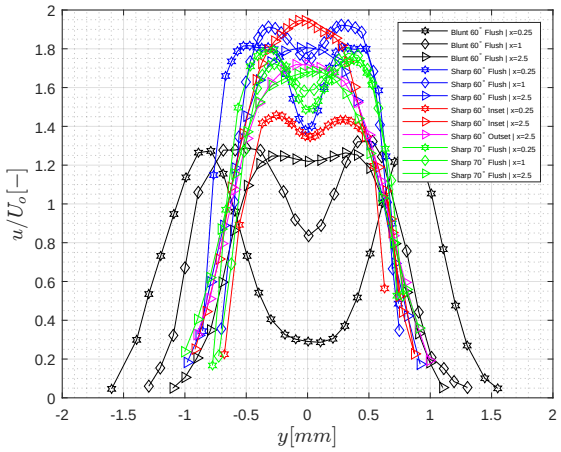

Figure 2.23: Velocity Profile Evolution at Near-field Streamwise Positions for Different Nozzle Configurations [48],[53]

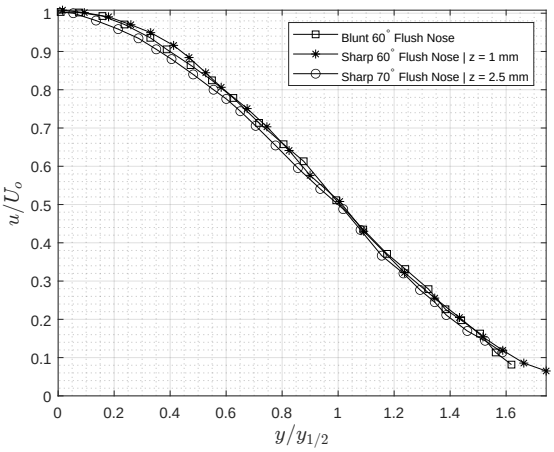

Figure 2.24: Normalized Velocity Profiles of Developed Combined Jets for Different Nozzle Configurations [48],[53]

I. Nose Sharpness Effect

Tate claims to be the first to study the effect of the sharpness of the spacing surface between the nozzle outlets with their work in [53]. Unlike the setup examined by Harpham in [48], the distance between the outlets of this setup is zero resulting in a sharp-edged nozzle. The near-field velocity profiles show that for the sharp 60° nozzle, the two peaks merge at positions nearer to

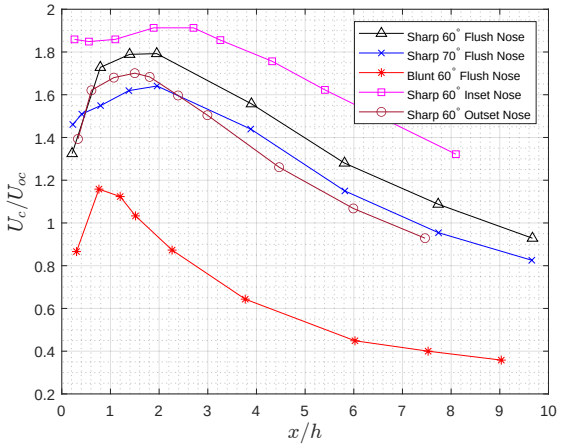

Figure 2.25: Near-Field Centerline Velocity Decay Profiles for Different Nozzle Configurations [48],[53]

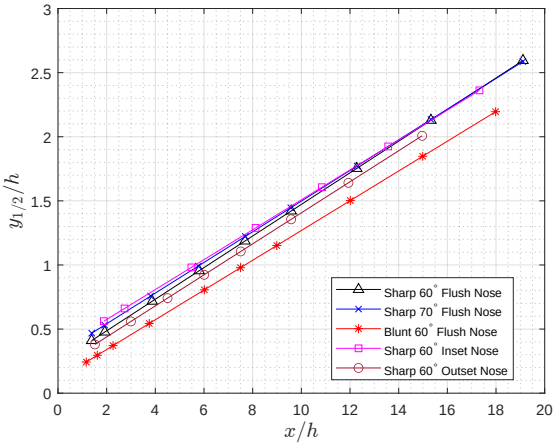

Figure 2.26: Half-width Growth Profile for Different Nozzle Configurations [48],[53]

the nozzle plane as compared to the "blunt" nozzle. The two jets merge more rapidly due to the zero spacing between the two outlets. The faster-merging leads to **mp** and **cp** getting closer to the nozzle outlet, hence maximum velocity is also higher for the sharp-edged nozzle, as evident from the results shown in Figure 2.23. Additionally, Figure 2.24 shows self-similarity for merged jets emanating from sharp and blunt nose nozzles of the same effective outlet heights d by plotting the dimensionless lateral velocity profiles at intermediate streamwise positions. Figure 2.25 shows that the sharp and blunt versions of the same nozzle have similar centerline velocity decay profiles, with the curves being offset for different configurations. The offset in their respective curves is attributed to the higher velocity achievable by the sharp nozzle due to early merging, as discussed. By observing the half-width growth plot corresponding to the sharp nozzle depicted in Figure 2.26 it could be seen that reducing the nose sharpness has almost no impact on the jet's half-width growth (k_1 in (2.23)). However, the k_2 value of the sharp nozzle is twice as large as the of the blunt nozzle indicating an increase in the magnitude of the virtual origin. In other words, the sharper nose has an effect on the half-width growth equivalent to that of emanating a jet from a recessed position as k_2 is proportional to x_o as shown in (2.23). The experimental work presented in [53] on the nose sharpness effect is numerically replicated by Krutka et al. in [51]. The numerical analysis demonstrates that turbulence models such as $k-\varepsilon$ standard model, the $k-\varepsilon$ realizable model, and the RSM fail to forecast the quantitative properties of the flow field when the default model parameters are used. Since experimental measurements for specific cases were available, it was easy to identify the values of the model parameters that produced the best results. Following additional testing, the RSM turbulence model was fine-tuned to reach a quantitative and qualitative agreement with the experimental findings for the blunt nozzle. According to this research, the tuning was limited to the coefficients associated with the dissipation equation, which were set to $C_{\varepsilon 1} = 1.24$ and $C_{\varepsilon 1} = 2.05$. This change of constants also improved the simulation's fit for the sharp nozzle cases. The same study shows a strong correlation between experimental and numerical predictions of dimensionless velocities U_c/U_{oc} at the jet centerline for both blunt and sharp nozzles.

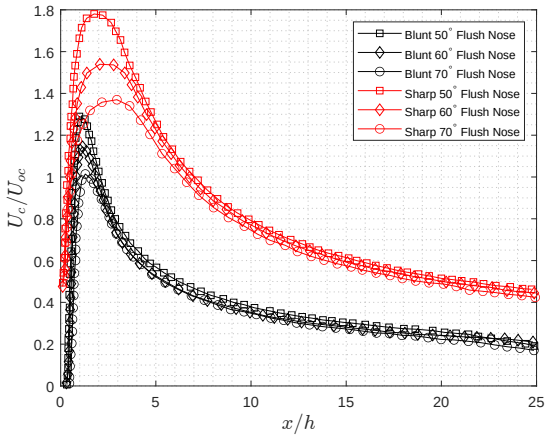

Figure 2.27: Centerline Velocity Decay Profiles at Different Discharge Angles for Both Sharp and Blunt Nose Nozzle Configurations [51]

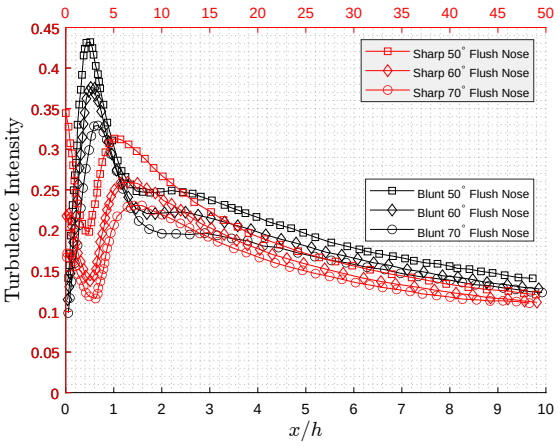

Figure 2.28: Centerline Turbulence Intensity Decay profiles at Different Discharge Angles for Both Sharp and Blunt Nose Nozzle Configurations [51]

II. Discharge Angle Effect

The mixing process of the individual jets in the converging zone is altered by changing the angle of the intersecting jet outlets, which impacts the characteristics of the combined jet. Numerous studies have been conducted to understand the angle effect of jets better and tune the nozzle outlet angles for optimal velocity, temperature, or mixing performance. Some of the early research on the flow characteristics of crossing jets is presented through Murai's work in [54]. This study shows that the combined point **cp** position advances upstream as the jet angle increases to become more convergent. Tate in [53], expanded on this research by examining the flow bulk characteristics of two sharp-edged nozzles with different discharge angles, namely, 60° and 70°. Figure 2.23 depicts the profile evolution near the nozzle outlet for a sharp 70° nozzle. Similarly, there are initially two peaks, which then combine into a single peak at about $1\,\text{mm} \leq x \leq 2.50\,\text{mm}$ yielding approximately the same streamwise merging distance as that of the sharp 60° nozzle. The two jets tend to act as parallel jets that combine slowly as the nose angle approaches 90°. Because of the slightly slower merging of the jets in the sharp 70° case, the maximum velocity achieved is less than that in the sharp 60° case, as illustrated in Figure 2.25. It is important to note that the flow rates and slot widths are matched for the different configurations in Figure 2.25. Figure 2.26 compares the half-width growth for the 70° sharp jet to the 60° sharp jet. The slope of the two geometries is nearly identical to that of the blunt-nose 60° nozzles, with the k_2 value being slightly higher for the sharp nozzles due to the prompt merging. The marginal reduction in the jet spread of the 70° nozzle jet can be explained by the more mild impact of the jets exiting the 70° nozzle relative to its 60° counterpart. Again, Krukta in [51], numerically studies the effect of the discharge angle on the jet characteristics for both the blunt and sharp nozzle. Figure 2.27 provides a comparison of the dimensionless velocities (U_c/U_{oc}) of the different discharge angles along the jet centerline of the sharp nozzle. The results indicate that the maximum velocity is reached closer to the outlet plane for smaller angles. This is expected behavior as the two jets meet sooner for smaller angles. Smaller jet angles result in higher maximum velocities for both blunt and sharp noses. This trend and the peak velocity x-position match the results of the experiment shown in Figure 2.25. However, the absolute values of the peak velocity for the 60° and 70° nozzles are slightly under-predicted by CFD.

Comparing Figure 2.28 to Figure 2.27, the author asserts that in the sharp-nozzle case, the locations of maximum turbulence occur earlier, at about half the corresponding x values, than the locations of highest velocity. The turbulence intensity begins at zero and steadily increases as the shear layer for the two jets develops. For all nozzle configurations, the turbulence intensity reaches a maximum value at $x/h < 1$; this maximum represents the high turbulence in the converging region. As the x distance increases, each curve goes through a minimum, rises to a local maximum, and then starts to drop down again. Figure 2.27 shows that the maximum speeds correspond to the x location of the minimum turbulence intensity. This is to be expected since the production of turbulence tends to stop when the slope of the average speed approaches zero. As the mean velocity profile slope becomes more negative, the turbulence intensity curves re-climb to local peaks. Generally, it's important to be very critical when analyzing or presenting turbulence-related metrics, as they are often inaccurate. In experiments, it is hard to capture turbulence and tell it apart from measurement errors. Some measurement methods are better at doing this than others. HWA is typically the way to go for collecting flow fluctuation data; however, it comes with the burden of calibration and the need for spatially traversing to capture a useful region of the flow. On the other hand, steady-state simulations don't typically do the best job of capturing turbulence for a number of reasons. The first is the lack of the ability to capture temporal effects, and the second is that they are run at a fairly low resolution. An LES with a high-resolution grid might be needed to accurately capture and resolve the turbulence length scale, which is the size of the large energy-carrying eddies in a turbulent flow. The energy exchange corresponding to different turbulence eddy sizes and fluctuation frequencies is found to be critical to the cooling capability and the thermal comfort delivered by a jet. However, this turbulence spectral analysis is beyond the scope of the current study as the focus is more on the bulk flow characteristics.

III. Nose Recession Effect

The previous analyses were performed on flush nose nozzles, also known as zero-inset nozzle, a configuration wherein the tip of the nose piece is on the same plane as the jet outlets. Tate et al. in [53], investigate the effect of sharp nose recession by comparing the previously presented flush 60° sharp-edged nozzle to inset and outset variants of the same nozzle. These configurations are obtained by varying the offset distance from the jet outlet plane (a) values by a few outlet heights in both directions. This study is conducted with the same flow rate $Q = 100\,\mathrm{L/min}$ and the same single outlet width $w = 0.56\,\mathrm{mm}$ for all configurations. Figure 2.23 shows a comparison of the velocity profiles of a flush 60° sharp nozzle to an inset 60° sharp nozzle at $x = 0.25\,\mathrm{mm}$. For the inset nozzle, effective outlet width d is smaller than that with a flush nozzle with the same w setting. Hence, flow is constricted, and the velocity would be expected to be higher, as shown in Figure 2.23. The same figure compares inset, flush, and outset nozzle results at $x = 2.50\,\mathrm{mm}$. At this larger x, the inset, flush, and outset peaks have all merged into single peaks, with the velocity peak highest for the inset nozzle and lowest for the outset nozzle. Similarly, for the outset nozzle, the outlet width d is larger than that with the flush nozzle at the same w setting. Hence, the jet flow is slower, and more spread out. Figure 2.25 shows the effects of the surface recession on the centerline velocity profile of a 60° sharp nozzle. The maximum normalized velocity values for the inset, flush, and outset nozzles are 1.9, 1.8, and 1.7, respectively. Figure 2.26 compares the jet spread of the three configurations. The slopes k_2 are found to be very close for different configurations. However, the intercept for the inset is about double the intercept for the outset, indicating that the virtual origin of the inset nozzle is located at a larger distance.

The work presented in [55] computationally studies the effect of nose piece recession. The

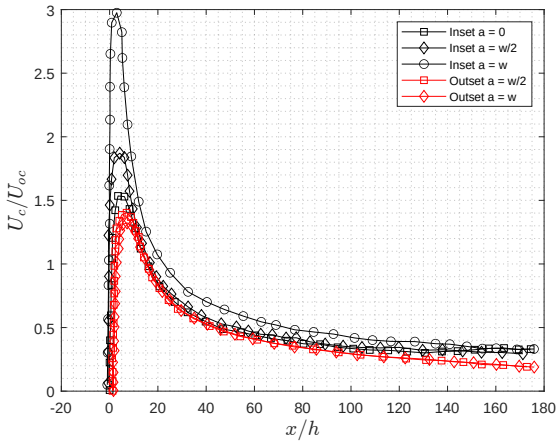

Figure 2.29: Centerline Velocity Decay Profiles at 60° Discharge Angle for Sharp Flush, Inset and Outset Nozzle Configurations [55]

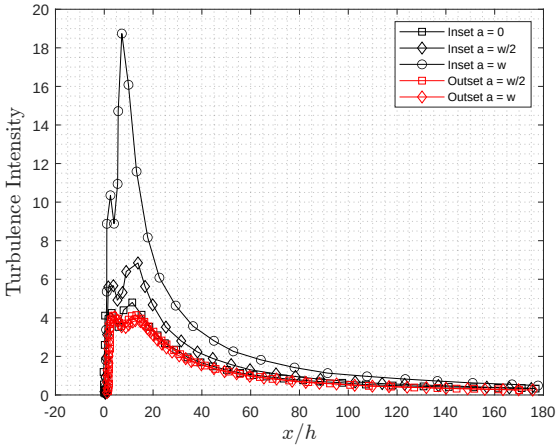

Figure 2.30: Centerline Turbulence Intensity Decay Profiles at 60° Discharge Angle for Sharp Flush, Inset and Outset Nozzle Configurations [55]

previously discussed turbulence model and settings are used for this study. For different inset/outset values, Figure 2.29 shows how the nose piece recession affects the dimensionless centerline velocity. Increasing the nose piece recession (more inset) clearly increases the maximum centerline velocity; the velocity at the highest recession $a/w = 1$ is almost double the velocity for a flush nose $a/w = 0$. This result is expected because increasing the nose piece's recession leads to a smaller effective nozzle width d assuming fixed w as discussed earlier. With the same flow rate, a smaller opening would result in a higher mean velocity. An opposite effect could be expected for outset nozzles. The same figure compares this centerline velocity for two different outset nozzles. The maximum centerline velocity is found to decrease as the nose piece extends beyond the nozzle plan. This study shows that the change in the velocity profiles is less for the case of outset versus inset noses as Figure 2.29 shows. Besides the obvious differences in the velocity peaks, all along the velocity profiles, there are large differences between the centerline velocities for different inset nozzles. In contrast, the outset nozzle has very similar centerline velocity profiles except for the relatively-small profile differences at positions near the velocity maxima. Figure 2.30 presents a comparison between the turbulence intensity nature along the line of symmetry for the different sharp nozzles. The turbulence intensity measures the relative strength of the velocity fluctuations. The maximum turbulence intensity increases as the nozzle inset increases, and exhibits two local maxima that vanish as the nose goes from being recessed to protruding. For inset nozzles, the first local maximum in turbulence intensity occurs near the nozzle plane $x \sim 0$, while the other is at a few nozzles width downstream from the exit plane. The turbulence intensity on the centerline increases as the jet travels through the merging region (between the **mp** and **cp**). At the first half of this region (upstream of the effective outlet), the airflow is forced to accelerate as the jets mix and move through the constriction, which increases the turbulence intensity and results in the first observed intensity maximum. As the fluid exits the constriction at the nozzle face, the turbulence decreases and the intensity shows a local minimum at a location corresponding to the **cp**. Downstream of the **cp**, the intensity increases again due to turbulence production, which is proportional to the slope of the mean velocity. The maximum turbulence intensity exhibited by the nozzle with an inset of $a/w = 1$) is significantly higher than that corresponding to the lower inset nozzles.

As the nose extends beyond the nozzle face for the outset nozzles, the effect of the nose offset distance becomes less pronounced. Figure 2.30 shows the turbulence intensity along the centerline of the different outset nozzles. The average outset nozzle intensity is an order of magnitude less than the average intensity for the inset nozzle. Similar to the case with the centerline velocities, there is little difference between the turbulence intensity in the flow fields from the nozzle with outsets of $a/w = 1$ and $a/w = 1/2$. This large variation in performance between inset and outset nozzles can be attributed to the effective outlet size as well as the surrounding condition where the merging takes place (upstream of the exit plane for inset nozzles and downstream of that for outset nozzles).

2.4. Overview of Offset Jets

An offset jet is defined as a single incompressible, turbulent air jet with mean exit streamwise velocity ($U_\circ$) issuing from a two-dimensional nozzle with width (w) into a quiescent ambient surrounding above a wall that is parallel to the discharge jet axis and offset by a distance (h). As the jet exits the nozzle, the air entrainment through the free boundary below the jet and above the plate creates a sub-atmospheric pressure zone causing the jet to bend towards the wall in the converging region and eventually attaches to it at what is known as the reattachment point (x_{rp}). A portion of the flow volume reverses into the cavity as the jet strikes the surface. The final configuration is one in which the mean volume flow entrained from the cavity by the jet's inner edge is balanced by the mean volume flow injected back into the cavity at the jet's reattachment point. Figure 2.31 shows a schematic representation of a planar offset jet, illustrating how a portion

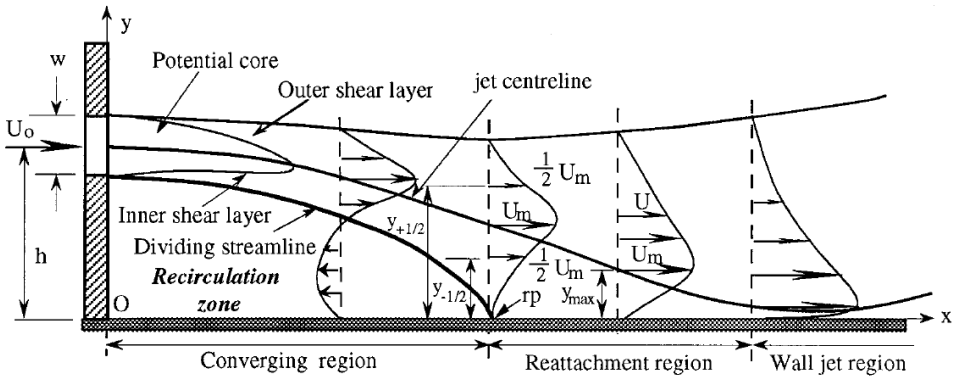

Figure 2.31: Single Offset Jet Schematic [36]

of the fluid in the inner shear layer is redirected upstream from the reattachment point into the recirculation zone due to an adverse pressure gradient. In the reattachment region, the flow is subjected to the adverse effects of the pressure gradient and strong interaction with the offset wall. Far downstream from the nozzle plane, the flow continues to develop in the wall jet region and resembles a wall jet flow [36]. The flow geometry of an offset jet is encountered in many engineering applications, and one configuration that Tesla relies on in its air vent design makes studying it relevant to this thesis. The majority of previous research on 2D offset jet flows has focused on the jet's mean flow characteristics. The first comprehensive investigation into the mean flow characteristics of a turbulent offset jet was published in [56]. This work proposed a theoretical model for a plane, incompressible, turbulent offset jet; this model shows that the flow characteristics become independent of the offset height (h), length of the offset surface (x_p),

and the nozzle's Reynolds number Re_w when these parameters are sufficiently large. A similar theoretical model was developed in [57] for a plane offset jet assuming a uniform pressure within the recirculation zone. Based on this assumption, the author approximated the curved portion of the offset jet as a plane-free jet and further simplified the analysis by considering the centreline of the jet as a circular arc assuming a thin jet width. The experimental data of the same study suggests that the location of the reattachment point coincides with the location of the maximum pressure on the offset surface. In a further investigation in [58], the same author examined varying entrainment rates at the jet's two edges, resulting in a more precise model prediction of the reattachment length and the recirculation zone's average pressure.

[59] presents detailed experimental results on the mean flow and turbulence characteristics in the converging and reattachment regions for a plane offset jet of an offset ratio $h/w = 6.5$. When the jet width-to-radius of curvature ratio was investigated in this study, the large ratio of the magnitude of the curvature strain rate to the shear strain rate implied that the flow could not be modeled as a thin shear layer for the offset ratio considered. Later, Pelfrey et al. experimentally studied the influence of jet curvature on the turbulence of a plane offset jet in [60]. Due to the flow curvature in the converging region, the measurements revealed that the jet flow had both stabilizing (lower side) and destabilizing (upper side) effects. The experimental results from a comparison between a wall-attaching offset jet and a plane wall jet presented in [61] shows that the offset jet is quite comparable to the plane wall jet in the wall jet zone, especially with regard to the decay of maximum velocity and the jet half-width.

Various types of submerged nozzle geometries have been investigated to study the impact of the nozzle geometry on the flow features of surface-attaching jets. The literature on circular nozzles [62], [63], square nozzles in [64], [65], rectangular nozzles in [64] and plane nozzles in [66], [24] are all good examples contributing to this investigation. For instance, [66] reported mean streamwise velocity measurements for three surface jet configurations: a plane, a circular, and a rectangular surface jet of the same offset ratio of $h/d = 0.5$. No significant differences were reported in the downstream evolution of the bluff (circular and rectangular) jets, but their spread and maximum mean velocity decay rates were significantly lower in comparison to the plane surface jet, which aligns with the previous observations made for free jets. Wen et al. in [67], [68] applied more advanced statistical analysis tools, such as the proper orthogonal decomposition (POD) method, to quantify the jet-surface interaction while Tay et al. in [64] and [69] presented detailed two-point correlation and surface velocity measurements, the same literature has comprehensively reviewed most of the previously mentioned studies. In a more recent study, Rahman et al. in [70] studied the impact of nozzle geometry on offset jets' mixing characteristics and turbulence structure.

Recent numerical research has focused on jet turbulence modeling; however, the geometries and operational parameters vary by application. Ideally, jets would be modeled numerically using DNS or experimental boundary conditions, eliminating the need for a nozzle in the solution domain or boundary layer resolution. Nonetheless, optimizing the nozzle shape requires including it in the solution domain, making this method impractical for industrial situations. On the other hand, LES modeling is appropriate for many flow problems because of its ability to model anisotropic flows. For specific applications, LES is unfeasible due to mesh size limits for appropriate resolution of turbulent eddies and wall modeling, rendering RANS turbulence models more suitable. RANS models use generic coefficients to provide accurate results for typical flow regimes. These coefficients are empirically derived for various general flow regimes, which is accurate in many

cases but not necessarily in capturing the spread rate of free jets. In order to optimize the RANS model coefficient, the full nozzle geometry must be included in the solution domain to accurately describe the shear layer along the nozzle wall and boundary layer separation. To numerically simulate the offset jet flow, [71] discretized the convective terms of the RANS equations (standard $k-\varepsilon$ turbulence model) with the use of hybrid, QUICKER, and skew-upwind schemes, with the QUICKER scheme showing to be the most superior when validated against experimental data from [72] and [59]. The flow field of a two-dimensional offset jet was numerically simulated in [73] using the unsteady RANS equations and the conventional $k-\varepsilon$ model. The simulation revealed that the reattachment point location becomes permanently stable following initial unsteadiness.

A few investigators have also studied a single offset jet in combination with a parallel adjacent wall jet (termed a wall-offset jet in the literature). In the case of wall-offset jet flow, after issuing from the two nozzles, the two jets merge together at the merge point (**mp**), forming a converging region between the merge point and the jet's exit plane. Also similar to free twin jets, the two jets initiate to interact with each other at the **mp**, and this interaction extends up to the combined point **cp**, forming the merging region. Downstream of the combined point **cp**, in the combined region, the flow field behaves similar to a classical wall jet flow in case the nozzle is at a close h distance from the surface.

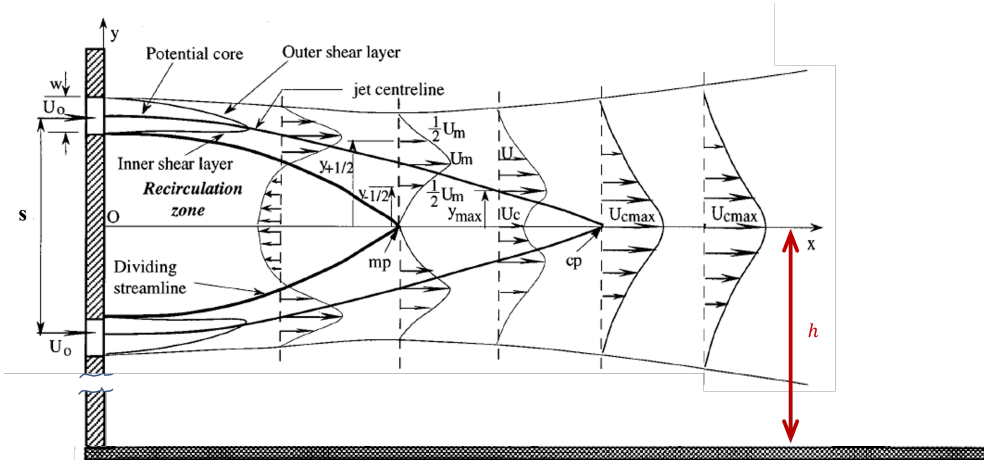

Figure 2.32: Twin Offset Jet Schematic [36]

Gap in literature: The previous review shows that major differences exist in the behavior of two-dimensional single and twin jets, especially in their mixing characteristics. However, the studies on twin jets are mainly focused on isolated parallel or intersecting jets, with a number of studies done on parallel wall-offset jets. To the author's knowledge, the research on installation effects on twin jets is limited to the recent numerical work done in [74] on parallel planar twin offset jets, illustrated in Figure 2.32. This creates an opportunity to both experimentally and numerically investigate the installation effects on intersecting planar twin jets.

Most-to-win: The relevance of this topic stems from the Tesla air vent configuration presented by the problem statement in Section 1.2. The installation effects related to the interaction of the vent with the decor or any A-surface represent a significant problem to be tackled in the design process. To this extent, a significant role is played by the dynamic structures of the jet interacting with the surface in the vicinity leading to the loss of control authority. A better understanding

of this phenomenon is needed to mitigate this risk which motivates the objective of this research outlined in Section 1.3 and the associated research questions.

To the authors' knowledge, this would be the first experimental study covering intersecting twin offset jets. The setup to be studied comprises two equal-width ($w = 7\,\text{mm}$) jets spaced at fixed distance ($s = 21\,\text{mm}$) and are set to an equal discharge angle ($\theta = 45^\circ$). The offset surface is detachable, allowing for varying the offset distance (h) throughout the experiment. The spacing surface is blunt and has a fixed recession distance ($a = 4\,\text{mm}$). The setup involves a bias flap that controls the flow rate into each nozzle channel to achieve a mass flow ratio ($MFR = [0-1]$). **This renders a two-variable research problem with the variables being (h) and (MFR).** More on the test setup is provided in the upcoming chapters.

3

Experimental Setup

Techniques for measuring mean velocity and turbulent fluctuations can be classified as either intrusive or non-intrusive and as either point or whole-field measurements. Airflow velocity measurements are generally performed using one of three principles: pressure measurement, thermal anemometry, or tracer particles. Pressure and thermal anemometry are both intrusive and point measurement techniques, while tracer particles allow for non-intrusive and often whole-field measurements. Particle Image Velocimetry (PIV) is a widely used example of non-intrusive flow measurement techniques with high spatial and temporal resolution [75]. PIV involves illuminating small particles seeded in a fluid with a laser light sheet, and the motion of the particles is captured by a high-speed camera. By processing the resulting images, velocity vectors of the fluid can be obtained as illustrated in Figure 3.1. Since its introduction by Adrian et al. in 1981, significant developments have been made to improve PIV's accuracy, and versatility [76]. However, PIV has limitations, such as its inability to measure flow properties in regions with low seeding density or high particle concentration. Despite these limitations, PIV remains a standard tool in experimental fluid mechanics due to its ability to measure instantaneous velocity fields accurately, making it an appealing choice to study the present problem.

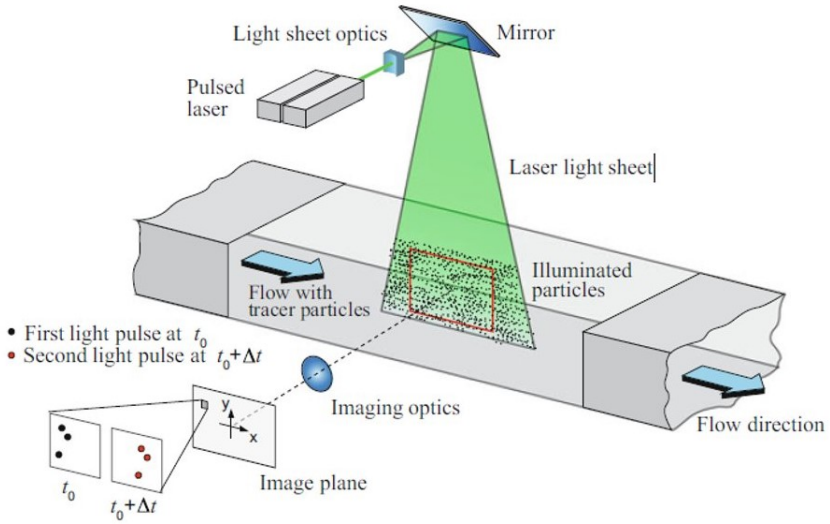

Figure 3.1: PIV Setup Illustration [77]

3.1. Experimental Facility and Measurement Technique

The experiment performed in this study is carried out at the A-tunnel located in the Low-Speed Laboratory (LSL) at TUDelft. The A-tunnel is a subsonic, open-walled, and closed-return wind tunnel allowing for a quick and convenient set-up and alteration of the experimental apparatus. This tunnel employs two centrifugal fans powered by 30kW electrical motors **(M)** to regulate airflow. The fan-generated airflow passes through a smooth ramp **(A)** into the nozzle inlet lip **(B)** followed by a honeycomb flow straightener **(C)** and four anti-turbulence screens **(D)** to reduce the flow's turbulence intensity. The airflow then undergoes a 15:1 contraction-ratio nozzle before exiting through a 0.6 m-diameter exhaust **(E)**. The exhaust can be fitted with interchangeable added nozzle geometries **(F)**, enabling the airflow to pass through desired geometries/test sections **(G)**, placed in an Anechoic plenum **(J)**, before traveling to the return leg of the chamber **(K)**. A schematic of the tunnel and the respective dimensions (in mm) are shown in Figure 3.2.

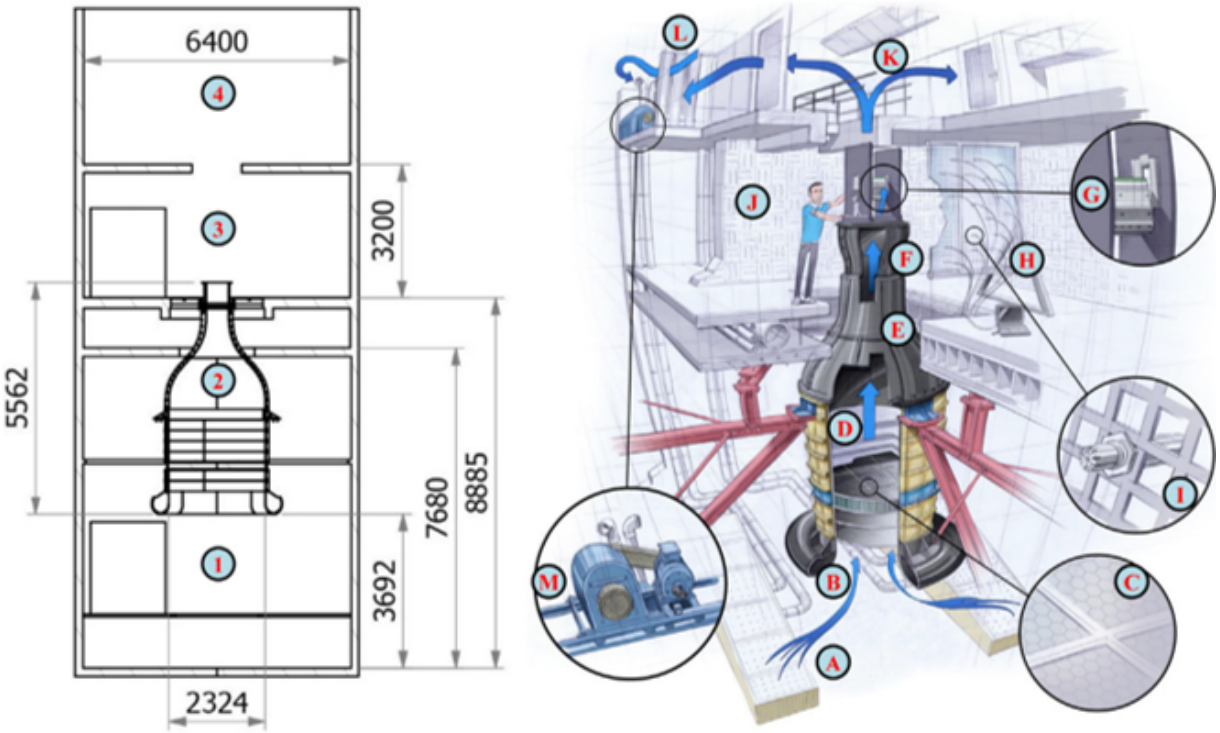

Figure 3.2: TUDelft A-tunnel Schematic [78]

The A-tunnel is capable of delivering velocities up to 45 $\mathrm{m\,s^{-1}}$ at the exhaust and turbulence intensity as low as 0.22% at the exit of any added nozzle geometry, and any flow velocity [78]. The light source used to conduct the PIV experiment is the Quantel Evergreen 200 laser. The laser system is a double pulsed Nd:YAG laser that comprises two cavities producing infrared lights of $\lambda = 1064\,\mathrm{nm}$ each. The two beams combined form a visible green laser light of $\lambda = 532\,\mathrm{nm}$. This laser produces light in the form of short-duration pulses, enabling the collection of picture pairs. After being discretized into smaller interrogation windows, these image pairs undergo post-processing in a statistical procedure known as cross-correlation. The cross-correlation logic compares the light intensity between the first and second images. The logic outputs signal peaks when the second image is shifted to align with the first due to tracer particles overlapping at certain locations. The displacement vector yielding the largest peak represents the average particle displacement within the designated interrogation area as illustrated in Figure 3.3. The PIV images

are captured using the Imager sCMOS cameras with the laser and cameras both controlled and synced using the acquisition software DaVis [79].

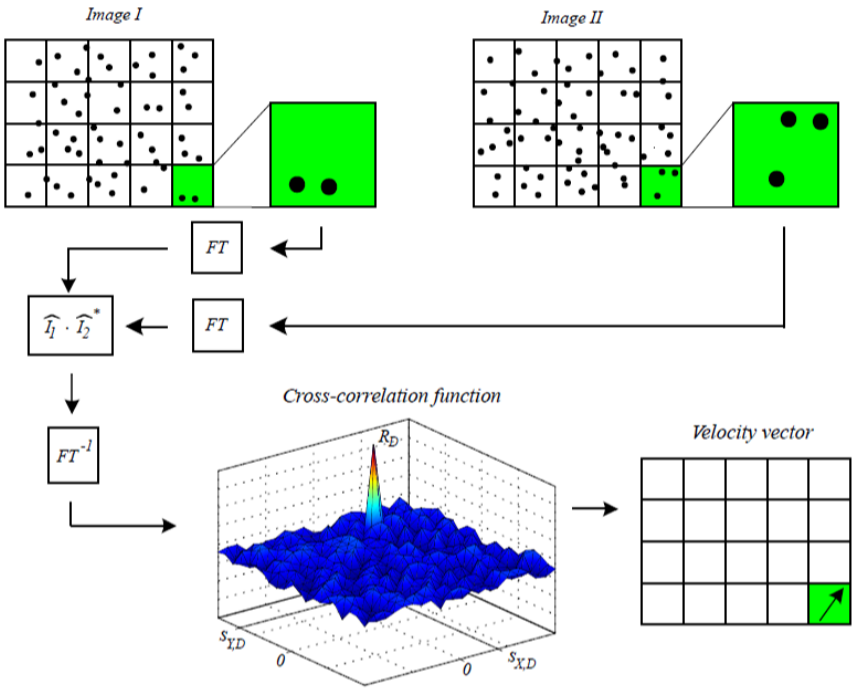

Figure 3.3: Schematic of vector calculation in PIV measurements [80]

3.2. Test Subject Description

As previously mentioned, a contraction is placed downstream of the 0.6-m diameter exhaust to transition the airflow cross-section from the 60cm diameter nozzle to a 25cm x 40cm rectangular section. This section is further reduced by another contraction to interface with a machined aluminum straight channel with a uniform cross-section of 0.14cm x 40cm. Finally, a claw-shaped nozzle is employed to split the airflow into two equal streams that merge at the nozzle outlet, as depicted in Figure 3.4. The flap mounted on the trailing side of the claw's core controls the airflow split across the claw. Furthermore, a slotted mount is fixed to the setup, allowing a flat plate to be placed tangential to the nozzle's centerline. The slots on the mount are evenly spaced perpendicular to the jet centerline. The design and dimensions of the nozzle's end section are illustrated in Figure 3.5. All components of the nozzle, including the flat plate and the mount, are 3D printed using SLA technology.

3.3. Setup and Calibration

The experiment uses planar PIV, a measurement setup comprising a single laser source and two tandem cameras with lines of sight at a slight angle to the laser sheet. Two cameras are used to capture a larger field of view without compromising the resolution of the samples. The bottom camera shown in Figure 3.4 captures the near-outlet flow field, while the top one captures the field slightly downstream of that. About 12% overlap between the two images is maintained to avoid data loss between the two fields of view; the two images are then stitched and post-processed by DaVis combined. The cameras and laser systems are both mounted on a number of 80/20's as

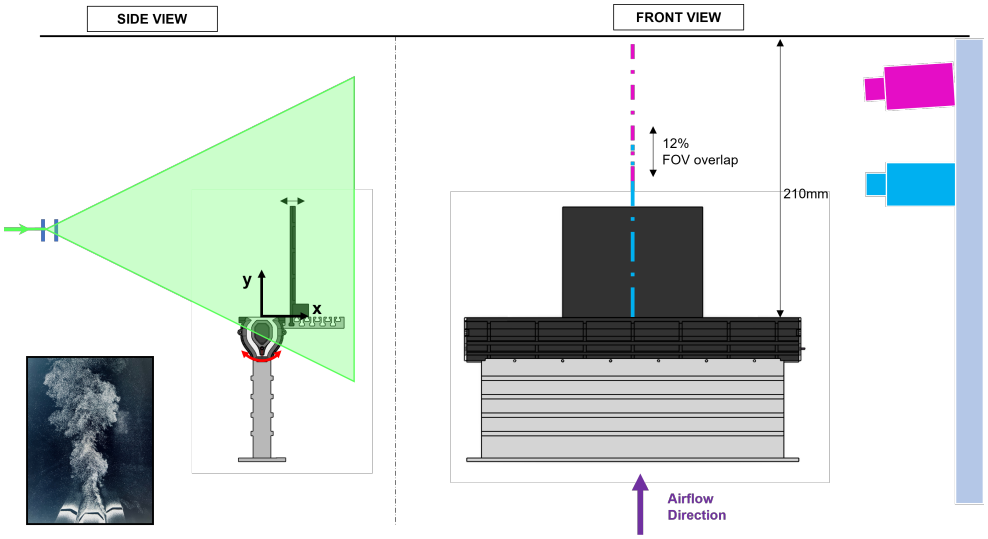

Figure 3.4: PIV Experimental Setup Schematic

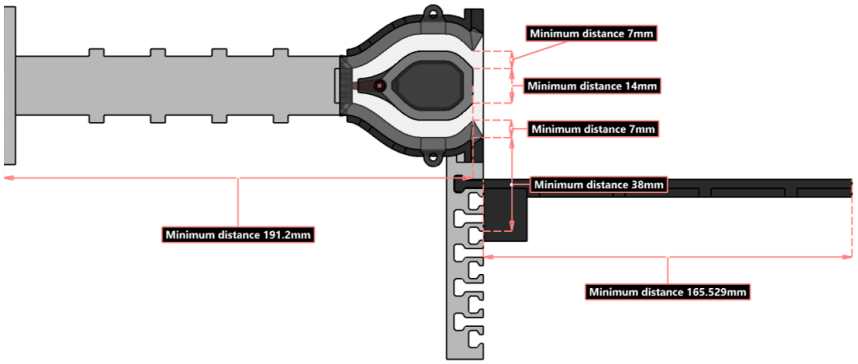

Figure 3.5: Test Subject Dimensions

illustrated in Figure 3.4. For most of the experiment, the laser sheet was aligned with the geometric center of the test subject for most of the experiment. The laser sheet is shifted for the measurements taken at different planes while maintaining the test subject fixed. This required re-calibrating the imaging system every time to ensure the criteria presented in the following sections of this chapter are all satisfied. Before discussing the design of the experiment and post-processing routines used, the setup parameters selected to ensure high confidence in the measurements are outlined.

FOV and Magnification Factor The field of view (FOV) is the size of the image and is typically defined with respect to the object of interest. In this analysis, the field of view desired is 30 times the channel width of the test subject. The channel width is 7 mm; hence, the field of view length in the streamwise direction is 210 mm. The PIV images are captured using a camera with a resolution of 2560×2160 pixels with 6.5 µm PixelSize/PixelPitch (pix_size). By definition, the magnification factor (M) is the ratio between the size (length) of the object in the image and that in reality. In this experiment, the magnification factor is determined using an image of a millimeter paper to map a known distance (dist) in [mm] to a distance in pixels (dist_px). This is performed by identifying two points on the calibration image, the distance between the points, and the pixel size. The magnification factor is then computed using the expression in (3.1). This value

is verified by checking the divider's length between the channels in the nozzle image obtained.

$$\mathrm{M} = \frac{\mathrm{dist\_px} \cdot \mathrm{pix\_size} \cdot 10^{-6}}{\mathrm{dist} \cdot 10^{-3}} = 0.141 \tag{3.1}$$

f-stop The f-stop, also denoted by $f_\#$, is the ratio between the focal length of the lens (f) and the diameter of the camera's aperture (d). The aperture's diameter controls how much light the lens lets in and the depth of the field captured (δz). Since the focal length is fixed by lens choice, $f_\#$ can only be varied by varying the aperture diameter. Increasing the aperture diameter allows more light into the lens resulting in a small depth of field, while decreasing the aperture diameter reduces the amount of light passing through the lens and increases the depth of field. Since the camera captures a projection of the particle, the particle's image size differs from its physical size. The size of the particle projection is estimated by (3.2).

$$d_{\mathrm{proj}} = \mathrm{M} d_p \tag{3.2}$$

where d_p is the particle physical diameter. Since a small hole of the camera is used to capture the scattered light from the particles, in addition to the particle projection on the sensor, there is also a contribution from diffraction, which occurs owing to light's wave-like behaviour. The diffraction effect also influences the particle image diameter. The diffraction of an imaged particle is characterised by a band of alternating dark and bright regions known as the airy disc. The diameter of the airy disc (d_{diff}) is what particularly influences the particle image diameter (d_τ). d_τ can be calculated as shown in (3.3).

$$d_\tau = \sqrt{(d_{\mathrm{proj}})^2 + (d_{\mathrm{diff}})^2} \tag{3.3}$$

Where the airy disc diameter (d_{diff}) can be correlated to the f-stop value ($f_\#$), magnification factor (M) and the laser wavelength (λ) through (3.4).

$$d_{\mathrm{diff}} = 2.44 \lambda \, (1 + \mathrm{M}) \, f_\# \tag{3.4}$$

By substituting (3.4) and (3.2) into (3.3), the for $f_\#$ can be given by (3.5)

$$f_\# = \frac{\sqrt{d_\tau^2 - (\mathrm{M} d_p)^2}}{2.44 \lambda \, (1 + \mathrm{M})} \tag{3.5}$$

All the parameters in (3.5) needed for computing the f-stop are known except for the particle image diameter d_τ. Choosing the right particle image diameter is critical for obtaining high-accuracy results. A particle image diameter that is smaller than a pixel size would result in what is known as pixel locking, which affects the accuracy of the measurement [77]. A rule of thumb is to set the particle image diameter to 2 times the pixel size to ensure that the displacement of a particle is captured by crossing a pixel. The particle image diameter for the current experiment then becomes,

$$d_\tau = 2 \cdot \mathrm{pix\_size} \cdot 10^{-6} = 13 \cdot 10^{-6}$$

By subbing d_τ along with the physical diameter of the seeding particles used is ($d_p = 1\,\mu\mathrm{m}$), the magnification factor calculated ($\mathrm{M} = 0.141$) and the laser wavelength ($\lambda = 532\,\mathrm{nm}$) into (3.5), the f-stop value is estimated to be,

$$f_\# \sim 8$$

Light pulse separation Δt calculation Image pairs are needed to translate the captured images into meaningful velocity maps. The light pulse separation time, or the interval between the two images of a pair, is a key parameter in calculating the velocity of the flow. The accuracy of the results remarkably depends on the chosen Δt. A too-larger or too-small Δt would both result in an undefined velocity field. As the objective of this technique is to construct a map of velocity vectors, the light pulse separation and the interrogation window size become correlated and equally important. A good PIV experiment practice known as the one-quarter rule recommends allocating a (Δt) that allows for a maximum displacement of a particle to be 1/4 of the interrogation window size (ws) at freestream velocity (U_∞) [77]. Using this criterion, the light pulse separation can be expressed as follows,

$$\Delta t = \frac{\text{displacement}}{\text{freestream velocity}} = \frac{0.25 \cdot \text{ws} \cdot \text{pix\_size}}{U_\infty \cdot \text{M}}$$

The experiment in hand is performed at $\Delta t = 30\,\mu\text{s}$, to ensure a sufficient transport of a particle between the two images of a pair ($\sim$8 pixels). The interrogation window size (ws) is then evaluated as follows,

$$\text{ws} = \frac{U_\infty \text{M} \Delta t}{0.25\text{pix\_size}} \approx 43$$

This windows size, however, does not include the effect of overlap between the interrogation windows, therefore it is more of a conservative estimate.

Depth of field The $f_\#$ value influences both the amount of light admitted by the lens and the depth of the field captured. The cameras can only clearly capture the motion of particles falling within a certain depth of field, requiring the depth of field to be larger than the laser sheet thickness. The depth of field can be expressed as a function of the magnification factor, the $f_\#$ and the laser wavelength and calculated as follows,

$$\delta_z = 4.88 \lambda f_\#^2 \left(\frac{\text{M}+1}{\text{M}} \right)^2 = 0.064\,\text{m} \tag{3.6}$$

The PIV setup parameters are summarized in Table 3.1

Table 3.1: PIV Experiment Setup Parameters

Parameter	Value	Parameter	Value
PIV Method	2D-2C	Imaging Resolution px/mm	21.76
FOV1 y_1 [mm]	-90	Magnification Factor (M)	0.1414
FOV1 y_2 [mm]	20	Depth of Field (δ_z) [mm]	64
FOV2 y_1 [mm]	-5	Pixel Size (pix_size) [µm]	6.5
FOV2 y_2 [mm]	120	f-stop (f#)	8
FOV y Overlap [mm]	12%	Light Pulse separation (Δt) [µsec]	30
FOV width [mm]	105	Window Size @ 0% Overlap - 1/4 Rule [mm]	43

3.4. Design of Experiment

The proposed PIV measurement campaign is carried out according to the test matrix in Figure B.1. The matrix is broken down into blocks and sub-blocks. The first block is dedicated to measurements to check for airflow two-dimensionality and Reynolds number independence. The second block involves independently varying both the tangential surface offset distance and the combined jet angle to quantify the influence of the surface offset distance on the jet's vertical control authority. The main jet characteristics obtained from the PIV experiment for the uninstalled, zero-degree jet case are validated using the results in existing literature and analytical solutions to establish the worthiness of the rest of the collected data as shown in Chapter 5.

3.5. PIV Data Post-processing

The collected data is then all post-processed in Davis concurrently; the settings used for vector post-processing are summarized in Table 3.2. The selected window sizes and overlap percentages for the vector calculation passes are chosen after trying different variants. These settings yielded the best vector resolution for the measurement at hand.

Table 3.2: PIV Raw Data Post-processing

Parameter	Value
Vector Calculation Method	Multipass
Initial pass window size	64x64 - 75% OL
Final pass window size	12x12 - 75% OL
Remove groups with vectors <	5

As the experiment conducted is non-time-resolved, it only allows for the analysis of the statistical behavior of the jet. To achieve this, the average and standard deviation of all 500 frames for each measurement point on the test matrix is computed and stored on a server. These lightweight files are further processed using a MATLAB script that computes several jet attributes, including the jet centerline velocity, half-width, jet angle, flow rate split between the two channels, reattachment point on the plate for the installed cases, merging point, and combined point. Two rounds of filtration are carried out to reduce noise in the measurements. Firstly, a low pass filter is set for velocity magnitude values that are below $0.5\,\mathrm{m\,s^{-1}}$, assigning these vectors a velocity of $0\,\mathrm{m\,s^{-1}}$. Secondly, masking for the surrounding environment is performed to eliminate any data captured within the test subject geometry or areas of no interest in the field of view. This was defined using a polygon consisting of the test subject's geometry and the region behind the plate for the installed cases, as shown in Figure 3.6. Once the statistical data is cleaned up, the jet metrics are computed as described in the following paragraphs.

Mass Flow Ratio (MFR) MFR is a parameter introduced to replace the flap input angle. The MFR is found to be a more robust metric as the flap used to vary the jet angle in this setup was manually controlled, resulting in higher measurement uncertainty. The high sensitivity of the jet angle to the flap position suggests that the flap angle needs to be very precisely mechanized for the measurements to be reliable. Computing the MFR after performing the experiment helps eliminate the uncertainty associated with the flap position. After applying the previously mentioned filters,

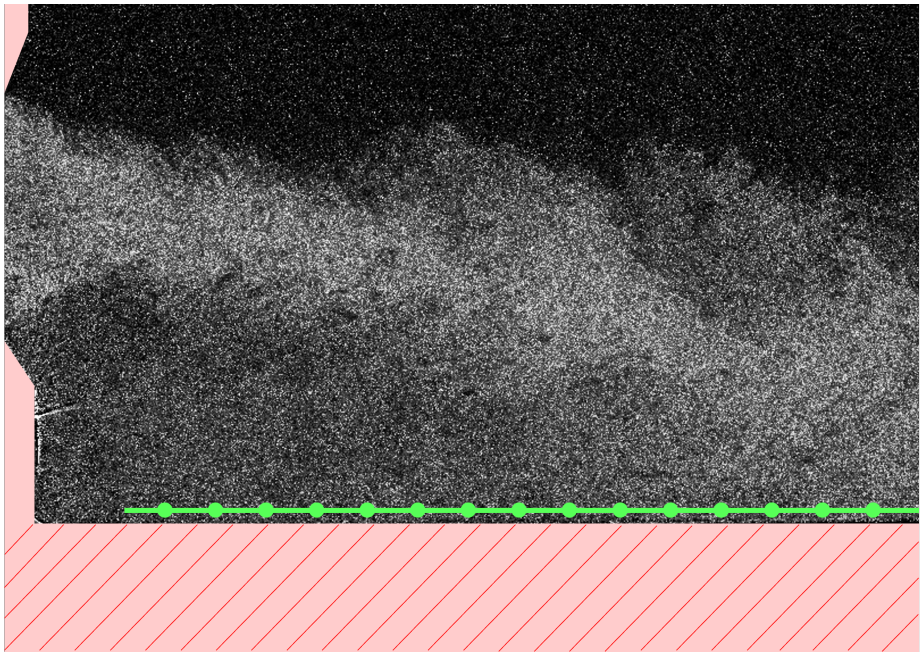

Figure 3.6: PIV Data Masking

the mean velocity contours are used to measure the MFR by placing line probes across the widths of the outlets. The velocity magnitudes are then extracted along these probes and then numerically integrated using the `trapz` function in Matlab as shown in Figure 3.7. The MFR is then computed as follows;

$$MFR = \frac{MF_{01}}{MF_{01} + MF_{02}} \tag{3.7}$$

Where MF_{01} is the flow rate at the bottom outlet and MF_{02} is the flow rate at the top outlet. With the assistance of the CFD model, a flap angle-to-MFR map is developed to understand the sensitivity of the outlet jet angle to the input flap angle. This map is shown in Figure 3.8

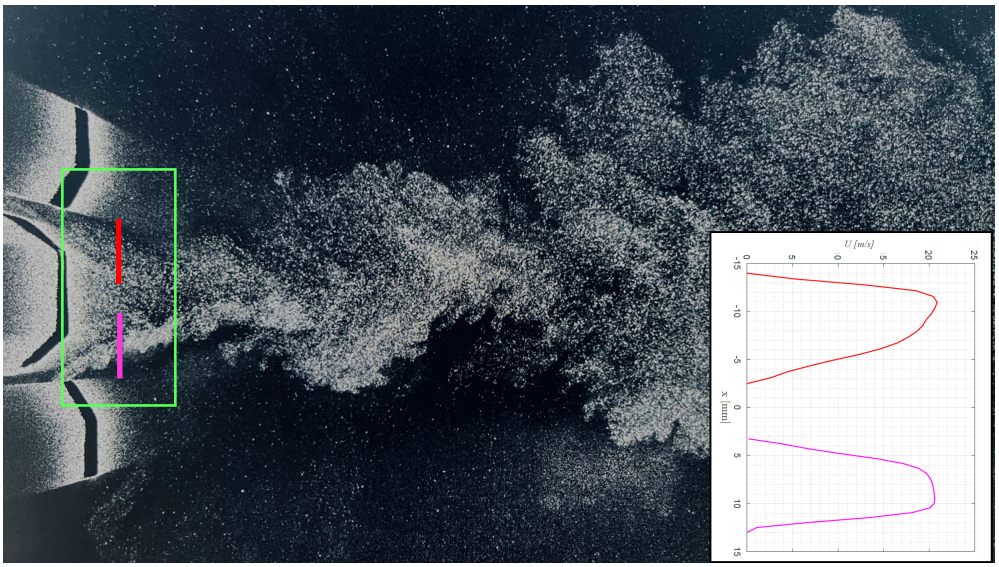

Figure 3.7: MFR Evaluation Schematic

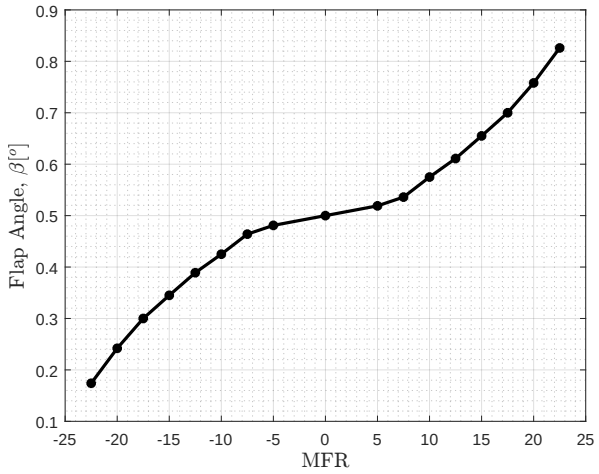

Figure 3.8: Flap Angle-MFR Map

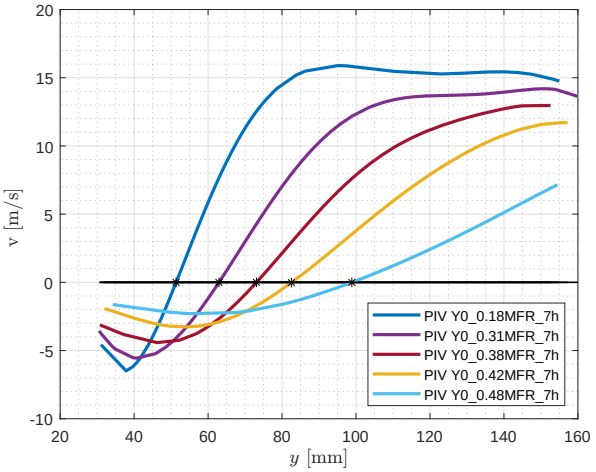

Figure 3.9: RP location Evaluation

Jet Centerline Velocity/ Half-Width Growth The jet centerline velocity is extracted from the 2D velocity contour by incrementally marching through the y-direction and extracting the maximum velocity magnitude values along a y-position. The maximum velocity values and their respective x-positions are then stored in 1D arrays. The half-width growth is defined as the x-position at which the velocity magnitude is half that of the centerline at a given y-position. Another array is created for the half-width x-position for an input flow field.

Jet Angle The angle of the jet is defined as the angle the centerline of the jet makes with the y-axis. For the uninstalled jet case, the jet angle is independent of the y region selected for computing this angle, as the centerline with the x-position varies linearly with the y-position of the jet. On the contrary, as shown in Chapter 5, the centerline velocity x-position varies non-linearly with the y-distance beyond a certain point as a function of the mass flow ratio and the surface offset distance. Hence, the jet centerline is evaluated upstream of this point; the onset of this point is defined based on the case where the nonlinearity of the profile develops the soonest. For the setup in hand, the region suitable for evaluating the jet angle is found to be between $6w - 8.5D$. For the different measurement points, the centerline velocity across this region is linearly curve fitted, and the angle of that curve is claimed to be the slope of the jet angle curve.

Reattachment Point (RP) The reattachment point refers to the point at which the jet shear layer boundary touches the installation surface. This point is critical to monitor as it relates to the control authority of the jet. The location of this point could be identified by monitoring the y-velocity profile right above the installation surface by placing a line probe along the surface as shown in Figure 3.6. The reattachment point is determined by the location at which the y-velocity switches signs or, in other words, the location at which $v = 0$. This point corresponds to the stagnation point on the plate where the edge of the shear layer intersects the plate. This reattachment point for the different cases is identified from the PIV measurement by extracting an axial velocity profile along a line probe placed parallel and close to the plate. The intersection of this velocity curve and the zero axial velocity line yields the point at which the axial velocity along this line switches signs representing the boundary between the jet stream direction and the recirculation zone, or the reattachment point.

4

Computational Setup

A CFD setup is generated to address the second aspect of the research objective. The 3D CFD setup is built to match the experimental conditions very closely. The 2D-assumed geometry consists of a single airflow inlet that splits into two outlets to form a claw-shaped nozzle, discharging the flow into the zero-gauge ambient domain. Figure 3.5 depicts in detail the nozzle geometry. The geometric dimensions, including the outlet heights, angles, and spacing, all adhere to the geometry used in the experimental setup. STAR-CCM+, the finite-volume solver, is used to execute the computational simulations for this study. The runs performed for this work use the segregated solver (solves momentum equations successively one at a time) and pressure-based formulation while employing an implicit pseudo-time-marching scheme for steady-state computations [[81], [82]].

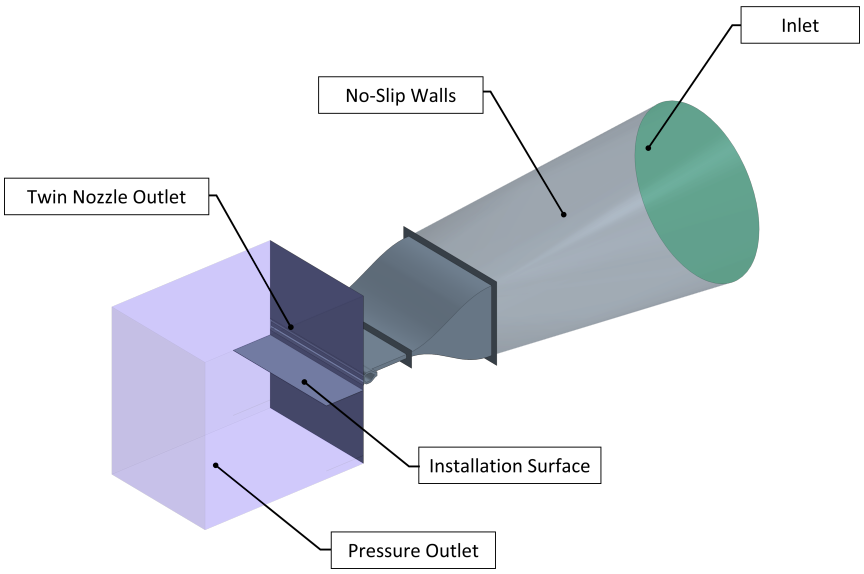

Figure 4.1: Iso-View of the Domain Geometry

4.1. Numerical Methodology

The behavior of anisotropic turbulence is observed in jet flow experiments due to strong boundary layer separation at the nozzle exit. This type of flow is difficult to model and has been demonstrated in numerical simulations using LES in [83]. RANS turbulence models use a common linear viscous

Boussinesq approximation, which assumes that turbulence's momentum transfer can be modeled by an eddy viscosity. This approach is similar to the hypothesis used for Newtonian flows, where viscous stresses are proportional to shear stresses and velocity gradients. Although this model assumes that eddy viscosity is direction-independent, there is still anisotropic turbulence because the Reynolds averaged strain rate tensor of the velocity field in the Navier–Stokes equations is not necessarily isotropic. While there is an expected error in using RANS approaches due to anisotropy, achieving results sufficient for understanding flow behavior is still possible if an average quantification is captured.

Numerical modeling of turbulent jets has been challenging since the early days of RANS turbulence modeling, as it often mispredicts spreading rates. This issue has been documented in numerous papers, including those by Pope [18], Quinn and Militzer [84], Launder and Spalding [85], as well as in David C. Wilcox's widely recognized book on turbulence modeling for CFD [86]. RANS turbulence models rely on empirical coefficients that are calibrated for general flow conditions. Although it would be ideal to derive these coefficients from fundamental principles, such as the kinetic theory of gases, the models are instead based on dimensional analysis and theoretical intuition, resulting in empirical coefficients that produce acceptable results for a wide range of flow conditions. The flow field of the current research problem is governed by the NS equations detailed in (2.2),(2.3) and (2.4), which together can be written using the compact Einstein notation as,

$$\frac{\partial u_j}{\partial x_j} = 0 \tag{4.1}$$

$$\cancel{\frac{\partial u_j}{\partial t}} + \frac{\partial}{\partial x_j}\left(u_j u_i\right) = -\frac{\partial}{\partial x_i}\left(\frac{p}{\rho_0}\right) + \frac{\partial}{\partial x_j}\left[\nu_m\left(\frac{\partial u_i}{\partial x_j} + \frac{\partial u_j}{\partial x_i} - \cancel{\frac{2}{3}\frac{\partial u_k}{\partial x_k}\delta_{ij}}\right)\right] \tag{4.2}$$

where, δ_{ij} is known as the Kronecker delta. It should be noted that the assumptions of steadiness and incompressibility led the first RHS term and the last LHS term to zero. The latter term is still included in the formulation for the solution boundedness.

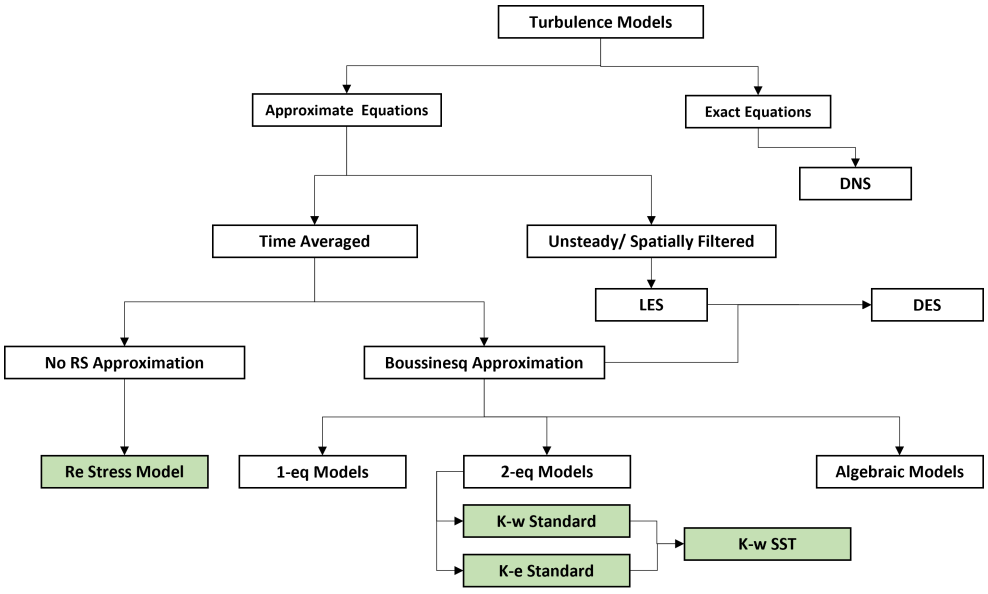

Figure 4.2: RANS Turbulence Models Map

Direct Numerical Simulations (DNS) is a method used to calculate turbulent flows for each point in the flow field by solving (4.1) and (4.2) directly. However, this method requires an extremely fine mesh with many mesh points to accurately resolve all the spatial and temporal turbulent scales, with a number of mesh points satisfying $N^3 \sim Re^{9/4}$, making it computationally expensive. Less expensive alternatives such as Reynolds Averaged Approach (RANS) or Large Eddy Simulation (LES) can be used to reduce computational time. The RANS approach involves solving for the mean pressure and velocity fields, while the LES approach models the subgrid-scale turbulence and solves for the large scales directly. The Navier-Stokes equations can be reduced to the RANS equations by assuming that the velocity and pressure can be described by the mean and fluctuation components as $u = \overline{u} + u'$ and $p = \overline{p} + p'$. With some lengthy reductions, the Navier–Stokes equation becomes the RANS equation below,

$$\frac{\partial \overline{u_j}}{\partial t} + \frac{\partial}{\partial x_j}\left(\overline{u_j}\,\overline{u_i}\right) = -\frac{\partial}{\partial x_i}\left(\frac{\overline{p}}{\rho_0}\right) + \frac{\partial}{\partial x_j}\left[\nu_m\left(\frac{\partial \overline{u_i}}{\partial x_j} + \frac{\partial \overline{u_j}}{\partial x_i} - \frac{2}{3}\frac{\partial \overline{u_k}}{\partial x_k}\delta_{ij}\right) \underbrace{-\overline{u_i' u_j'}}_{\tau_{ij}/\rho}\right] \tag{4.3}$$

By examining the difference between the classic Navier–Stokes equation in (4.2) and the Reynolds Averaged version in (4.3), it can be realized that an extra term, $\overline{u_i' u_j'}$, appears in (4.3). This term, multiplied by the density of the fluid, yields what is known as the Reynolds stress tensor, commonly denoted by (τ_{ij}). The other difference appears in using the mean pressure and velocities instead of instantaneous in (4.2). This is an important realization as this additional term is essential in RANS and LES turbulence treatment. The Reynolds stress term needs to be modeled to close the RANS equations. The term can be calculated directly with the addition of six transport equations, one for each unique term in the symmetric matrix using the Reynolds Stress Model (RSM); this approach is, however, still considered expensive. This motivated researchers to propose models that approximate this term as a cheaper alternative. Although single transport equation models like the mixing length and Sparlat-Allmaras offer high computational efficiency, their accuracy is limited. The Boussinesq Eddy Viscosity Model (EVM) is the most popular choice for turbulence modeling due to its balance between accuracy and required computational resources. The EVM reduces the six transport equations of the RSM to two, and the $k-\varepsilon$ and $k-\omega$ models, along with their variants, are some of the most popular examples of EVMs. This model approximates the Reynolds stress tensor for subgrid LES and RANS turbulence models. The eddy viscosity model assumes that the Reynolds stress tensor can be approximated as follows:

$$-\overline{u_i u_j} = \tau_{ij} = 2\nu_T S_{ij} - \frac{2}{3}k\delta_{ij} \tag{4.4}$$

where ν_t is the eddy viscosity, S_{ij} is the strain rate tensor, and the last term is an outcome of the isotropic turbulence assumption. The strain rate tensor is defined as:

$$S_{ij} = \frac{1}{2}\left(\frac{\partial u_i}{\partial x_j} + \frac{\partial u_j}{\partial x_i}\right) \tag{4.5}$$

where u_i is the velocity component in the i-direction. This approximation assumes that the turbulent fluctuations' average effect on the flow's momentum transfer can be modeled as a kind of molecular diffusion process. In this process, the transfer of momentum can be described by an effective viscosity that varies with the turbulence characteristics of the flow. The analogy

with molecular diffusion arises from the observation that turbulent fluctuations are similar to the random motion of molecules in a fluid, which also leads to the transfer of momentum and heat.

The strain rate tensor in the eddy viscosity model is related to the fluid flow rate of deformation, which can be viewed as the stretching and twisting of fluid elements. This deformation rate is analogous to the rate of deformation in molecular diffusion, which describes the rate at which molecules move and diffuse in a fluid. In regions of high strain rates, the flow is stretched and sheared at a high rate, which can lead to the development of large turbulent eddies. In regions of low strain rates, the flow is relatively quiescent and may be dominated by smaller eddies or fluctuations. In molecular diffusion, the diffusion rate depends on the properties of the molecules, such as their size and shape, as well as on the local concentration gradient. Similarly, in the eddy viscosity model, the eddy viscosity is assumed to depend on the properties of the turbulent eddies, such as their size, shape, and orientation, as well as on the local strain rate tensor. The eddy viscosity, ν_t, is related to the turbulent kinetic energy (k), also commonly referred to as TKE, and the dissipation rate of the turbulent kinetic energy (ε) through (4.6). The TKE is a measure of the kinetic energy associated with the velocity fluctuation per unit mass of flow.

$$\nu_t = C_\nu \frac{k^2}{\varepsilon} \tag{4.6}$$

where ρ is the fluid density, C_ν is a model constant that varies depending on the specific turbulence closure model being used. The term k^2/ε represents the ratio of the TKE to the dissipation rate of the TKE, which is used to estimate the length scale and time scale of the turbulence. k is expressed mathematically as:

$$k = \frac{1}{2}\langle u_i'^2 \rangle \tag{4.7}$$

The Boussinesq eddy viscosity assumption for the Reynolds Stress with incompressibility is given by

$$-\overline{u_i u_j} = \tau_{ij} = \nu_t \left(\underbrace{\frac{\partial u_i}{\partial x_j} + \frac{\partial u_j}{\partial x_i}}_{2S_{ij}} - \frac{2}{3}\frac{\partial u_k}{\partial x_k}\delta_{ij} \right) - \frac{2}{3}k\delta_{ij} \tag{4.8}$$

where the first term on the right-hand side is the deviatoric part, the second is the isotropic part, and k is specific kinetic energy. (4.8) is then plugged into (4.3) to obtain the Navier–Stokes momentum equation used in CFD solver codes.

$$\frac{\partial \overline{u_j}}{\partial t} + \frac{\partial}{\partial x_j}\left(\overline{u_j u_i}\right) = -\frac{\partial}{\partial x_i}\left(\frac{\tilde{p}}{\rho_o}\right) + \frac{\partial}{\partial x_j}\left[(\nu_m + \nu_t)\left(\frac{\partial \overline{u_i}}{\partial x_j} + \frac{\partial \overline{u_j}}{\partial x_i} - \frac{2}{3}\frac{\partial \overline{u_k}}{\partial x_k}\delta_{ij}\right)\right] \tag{4.9}$$

$$\tilde{p} = \overline{p} + \frac{2}{3}\rho_o k \delta_{ij} \tag{4.10}$$

where $\tilde{p}$ is a modified mean pressure that has absorbed the isotropic part of the Reynolds stress term. Based on (4.6) the eddy viscosity models work on solving additional transport equations for scalar quantities, such as k and ε, that enable the turbulent viscosity ν_t to be derived. The most commonly used two-equation eddy viscosity turbulence models are k-ε and $k-\omega$ and their variants. These models use an equation to solve for turbulent kinetic energy, k, and another one for solving the turbulence length scale, typically using the turbulent kinetic energy dissipation rate ε or specific dissipation rate ω.

k-ε Turbulence Model k-ε is the more popular of the two previously mentioned models. The standard k-ε uses a modeled transport equation for k, given by (4.11), which is based on the exact transport equation. In the standard k-ε model, the following assumptions are employed for the derivation of the transport equations of k: the production term is modeled using the Boussinesq approximation, and the turbulent diffusion is approximated with a gradient-diffusion hypotheses

$$\frac{\partial(k)}{\partial t}+\frac{\partial(u_j k)}{\partial x_j}=\underbrace{\tau_{ij}\frac{\partial u_j}{\partial x_j}}_{\text{k production}}-\underbrace{\varepsilon}_{\text{k dissipation}}+\underbrace{\frac{\partial}{\partial x_j}\left[\left(\nu+\frac{\nu_t}{\sigma_k}\right)\frac{\partial k}{\partial x_j}\right]}_{\text{k diffusion}}+\underbrace{S_k}_{\text{k source term}} \tag{4.11}$$

The terms in (4.11) has the following physical interpretation

- $\frac{\partial(k)}{\partial t}+\frac{\partial(u_j k)}{\partial x_j}$: Represents the temporal change and the convective contribution.
- **k production**: Through this term, energy is extracted from the mean flow to large eddies and converted from mean kinetic energy to turbulent kinetic energy.
- **k diffusion**: relates to turbulent transport, pressure diffusion and molecular diffusion
- **k dissipation**: This term represents the rate of dissipation, i.e., the conversion rate of k to heat (mainly at small scales) per unit time and mass.
- **k source**: This term appears to add the contribution of an extra source of turbulence added to the system

A transport equation for the dissipation rate is also needed to close the equation system. It is possible to derive an exact ε-equation, but it is not useful as a starting point for a modeling equation [18]. Instead, the ε equation is based on the assumption that its principal appearance is similar to the modeled k-equation, with additional modeling constants added. In order to achieve dimensional correctness, the production and dissipation terms are multiplied by the factor ε/k. The resulting transport equation for ε writes as follows,

$$\frac{\partial(\varepsilon)}{\partial t}+\frac{\partial(u_i\varepsilon)}{\partial x_j}=\underbrace{C_{\varepsilon 1}f_1\frac{\varepsilon}{k}\tau_{ij}\frac{\partial u_j}{\partial x_j}}_{\varepsilon\text{ production}}-\underbrace{C_{\varepsilon 2}f_2\frac{\varepsilon}{k}\varepsilon}_{\varepsilon\text{ dissipation}}+\underbrace{\frac{\partial}{\partial x_j}\left[\left(\nu+\frac{\nu_t}{\sigma_\varepsilon}\right)\frac{\partial \varepsilon}{\partial x_j}\right]}_{\varepsilon\text{ diffusion}}+\underbrace{S_\varepsilon}_{\varepsilon\text{ source}} \tag{4.12}$$

where f is a damping function, and C is a model coefficient.

The standard k-ε model is considered to be a complete turbulence model with relatively low complexity and is widely incorporated in commercial CFD software. It is known to be user-friendly and computationally efficient when combined with wall functions, according to Pope in [18]. The standard k-ε model's performance has been heavily valid against various practical flows, making it the most widely used and verified turbulence model. Nevertheless, the model produces inaccurate results in certain cases, particularly in flows with strong streamline curvature or boundary layers with strong pressure gradients (near-wall flows). The Boussinesq assumption causes the model's inaccurate predictions in certain cases, particularly in flows with strong streamline curvature or of the Boussinesq assumption, which ignores Reynolds stress anisotropy. Additionally, the standard k-ε model is known to mispredict the spreading rate of a single-round jet.

k-ω Turbulence Model $k-\omega$ model is another two-equation model that solves the transport equations for the turbulent kinetic energy k and the specific dissipation rate ω. The specific dissipation rate can be described as the dissipation rate per unit kinetic energy or ($\omega \sim \frac{\varepsilon}{k}$). The concept of a two-equation turbulence model for kinetic energy and dissipation per unit turbulence kinetic energy was first suggested by Kolmogorov in 1941 [87]. However, Saffman [88], who was unaware of Kolmorgorov's work, later produced a $k-\omega$ model that showed better agreement and has since been the basis of modern $k-\omega$ turbulence models. David C. Wilcox has significantly contributed to developing the $k-\omega$ turbulence model, which is widely used today. The standard transport equations for the $k-\omega$ model are expressed as;

$$\frac{\partial(k)}{\partial t}+\frac{\partial(u_j k)}{\partial x_j}=\underbrace{\tau_{ij}\frac{\partial u_j}{\partial x_j}}_{\text{k production}}-\underbrace{\beta^* f_{\beta^*}\omega k}_{\text{k dissipation}}+\underbrace{\frac{\partial}{\partial x_j}\left[(\nu+\nu_t\sigma_k)\frac{\partial k}{\partial x_j}\right]}_{\text{k diffusion}}+\underbrace{S_k}_{\text{k source term}} \tag{4.13}$$

$$\frac{\partial(\omega)}{\partial t}+\frac{\partial(u_i\omega)}{\partial x_j}=\underbrace{C_{\varepsilon 1}f_1\frac{\varepsilon}{k}\tau_{ij}\frac{\partial u_j}{\partial x_j}}_{\varepsilon\text{ production}}-\underbrace{\beta f_\beta\omega^2}_{\omega\text{ dissipation}}+\underbrace{\frac{\partial}{\partial x_j}\left[(\nu+\nu_t\sigma_\omega)\frac{\partial\omega}{\partial x_j}\right]}_{\omega\text{ diffusion}}+\underbrace{S_\omega}_{\omega\text{ source}} \tag{4.14}$$

The $k-\omega$ model is known for its superiority in capturing near-wall, and boundary-layer flows under adverse pressure gradients. On the other side, this model has been found to be more sensitive to the free stream dissipation rate ω, making the solution predicted by this model more sensitive to inlet conditions. This sensitivity is less prominent in the $k-\varepsilon$ model.

k-ω SST Turbulence Model The challenge of dealing with intersecting jets arises due to the existence of three different flow regions, each with distinct flow physics. While computationally efficient two-equation models have been developed and optimized for simple turbulent flows, their applicability to different geometries has revealed their limitations. Although no single model has yet produced a definitive solution, a hybrid turbulence model can be constructed by combining multiple models to create a compromise solution. This involves selecting a model that has been successfully tested for the specific flow region (free jet, stagnation, or wall jet) and seamlessly merging the results obtained from multiple models at the boundaries. This approach allows for the utilization of the strengths and reducing weaknesses of each model to produce a more accurate solution.

The goal of the $k-\omega$ SST turbulence models is to use the $k-\omega$ model due to its robustness near the wall and then transition to the $k-\varepsilon$ model for its effectiveness in the far field [81]. This is achieved by applying a blending parameter, $F1$, which is a function of wall distance to the dissipation equations of the $k-\omega$ and $k-\varepsilon$ models. When the value of F_1 equals one, the $k-\omega$ proposed by Wilcox in [86] is used. When F_1 equals zero, a transformed version of the standard $k-\varepsilon$ model of Launder and Spalding [85] is used. It should be noted here that the "transformed" $k-\varepsilon$ model is typically stated to be an exact transformation of the $k-\varepsilon$ model, but this is erroneous to state because terms are dropped in the derivation. The dissipation transport equation for the $k-\omega$ SST model writes as

$$\frac{\partial(\omega)}{\partial t}+\frac{\partial(u_i\omega)}{\partial x_j}=\underbrace{P+2(1-F_1)\sigma_{\omega 2}\frac{1}{\omega}\frac{\partial k}{\partial x_j}\frac{\partial \omega}{\partial x_j}}_{\omega\text{ production}}-\underbrace{\beta f_\beta \omega^2}_{\omega\text{ dissipation}}+\underbrace{\frac{\partial}{\partial x_j}\left[(\nu+\nu_t\sigma_\omega)\frac{\partial \omega}{\partial x_j}\right]}_{\omega\text{diffusion}}+\underbrace{S_\omega}_{\omega\text{source}} \tag{4.15}$$

Based on the previous discussion and literature on computational investigations of similar flows, the two-equation eddy viscosity models and the six-equation RSM, highlighted in Figure 4.2, are evaluated for capturing the statistical jet characteristics. The outcome of this evaluation is presented in Chapter 5.

4.2. Flow Physics & Model Closure

The computational model implemented in this study uses the default STAR-CCM+ incompressible constant-density setting. The modeled air is assumed to have a constant density of $1.184\,\mathrm{kg\,m^{-3}}$, a constant dynamic viscosity of 1.855×10^{-5} Pa/sec, and a reference pressure of 101 325.0 Pa. The energy equation is disabled in the model as the research focuses on the jet's aerodynamic behavior rather than its heat transfer characteristics. In practical flow problems, the interaction between walls and flow can induce vorticity, and accurately predicting flow and turbulence parameters across the wall boundary layer is crucial. Three common wall treatment methods are high-$y+$, low-$y+$, and all-$y+$ wall treatments. The high-$y+$ wall treatment is suitable for large Reynolds number flows and assumes that the near-wall cell lies within the log layer of the boundary layer. In contrast, the low-$y+$ wall treatment is only suitable for low Reynolds number flows and requires a fine mesh to resolve the viscous sublayer. The all-$y+$ wall treatment, which uses blended wall functions, is the most appropriate approach for a wide range of near-wall mesh densities and the one employed in the analysis of this study. The momentum and continuity equations are then coupled using a predictor-corrector approach. In conjunction with the SIMPLE scheme, the formulation adopts a collocated variable configuration (rather than staggered), and a Rhie-and-Chow-type pressure-velocity coupling [89]. This approach is better suited for flows with constant density. The incompressible flow assumption is valid for low Mach, hence the constant density setting used in this study. [90].

4.3. Boundary and Initial Conditions

As shown in Figure 4.1, the inlet of the domain is prescribed at the green circular surface upstream of the contraction, while the outlet is represented by the purple box. The boundary conditions are defined as follows The initial conditions for free stream velocity and pressure are left at their default values of 0 Pa and 0 m/sec, respectively. Additionally, the values of the initial and boundary turbulent quantities are determined based on guidelines for fully turbulent flows, as all presented simulations are deemed to be fully turbulent. Moreover, the infinitely wide assumed geometry permitted prescribing a pressure-outlet boundary condition wherever that is not the nozzle surface, installation surface, or nozzle inlet. The boundary condition settings used are summarized in Table 4.1

4.4. Meshing Scheme

This model employs a baseline mesh as a starting point for democratizing the problem domain. A refinement volume in Figure 4.3 is utilized in the static mesh instance to improve the mesh

Table 4.1: CFD Boundary Condition Settings

Boundary Condition	Parameter
Inlet	• Initial Gauge pressure = 0 Pa • Mass Flow Inlet = 350 CMH • Turbulent intensity = variable • Turbulent viscosity ratio = 10
Outlet	• Gauge pressure = 0 Pa
Nozzle Wall	• Stationary wall • No Slip

resolution in the jet's near-field. The size of the static refining zone is set to capture the turbulence interactions in the spreading shear layer, requiring a cone angle of about 15° to guarantee capture jet spreading. As shown in Figure 4.3, the computational domain outlet is rectangular with an x-dimension of $\sim$ 22 nozzle outlet heights (d) and a z-dimension of $\sim$ 20 nozzle outlet heights.

The surface remesher model is applied to the imported surfaces to build a smooth, high-resolution triangular surface suitable for the CFD mesh. In the core volume of the fluid domain, the polyhedral mesher model is used to generate arbitrary polyhedral cells at a gradual growth rate. The base size of the polyhedral cells is preliminarily set to 4 mm, and the volume growth rate (the rate at which the cell size transitions from the border to the core of the mesh) is set to 1.2 in order to improve the resolution of flow gradients and bulk characteristics. The mesh base size is varied, as shown in the upcoming grid sensitivity study section, before a final size is chosen. The maximum cell size in the domain is set to orders of magnitude higher than the base cell size to ensure a reasonably homogeneous far-field discretization. In addition, the prism layer mesher model is used to create conformal prismatic cells at the wall surface to resolve the boundary layer. The size and number of prismatic cells are selected to ensure that the cell nearest the wall has a near-wall height of ($Y+ < 1$). The prism cell size and stretching factor are specified to prevent excessive increases in cell size during the transition from prism to core cells. Due to the relatively long lead-in contraction resulting in a large boundary layer development, 8 prism layers with a total thickness of approximately 0.5 mm were utilized. The parameters mentioned above resulted in a baseline mesh with 1.5 million cells; a section of the mesh's center plane is illustrated in Figure 4.3. The cell volumetric control region is added to this mesh to limit the size of the contained cells resulting in a higher near-field resolution illustrated by the sample mesh in Figure 4.4. To accurately capture the jet-surface interactions, the current setup requires either enlarging the refinement zone to enclose the flat plate at all different heights. This would lead to a significant increase in the cell count of the domain. Alternatively, the refinement cone could be shifted following the plate. The latter is assessed and yielded asymmetric results about the nozzle centerline for the uninstalled $MFR = 0$ case. This asymmetry is attributed to asymmetric mesh, which introduced variations in the spreading behavior of the upper and lower shear layers. Therefore, the more expensive option is chosen in this study for higher confidence in the results.

4.5. Solution Convergence Criteria and Data Extraction

The stopping criteria for convergence in all simulations require the driving pressure at the flow inlet to have an asymptotic variance of less than 0.01 over the last 500 iterations or a total of 2000 iterations. The CFD data is extracted along the planes used for collecting the PIV data. The data

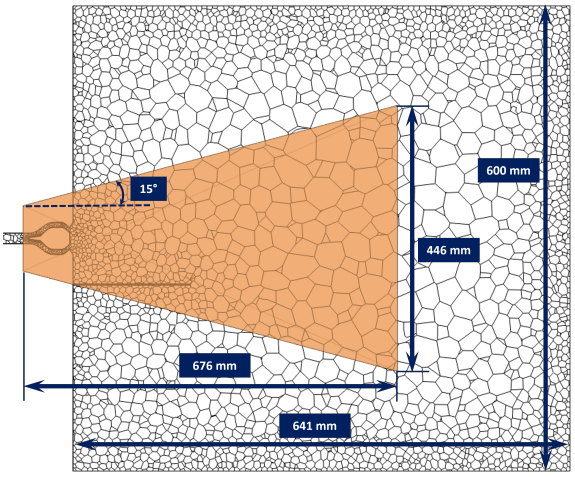

Figure 4.3: Domain Outlet and Refinement Volume Dimensions

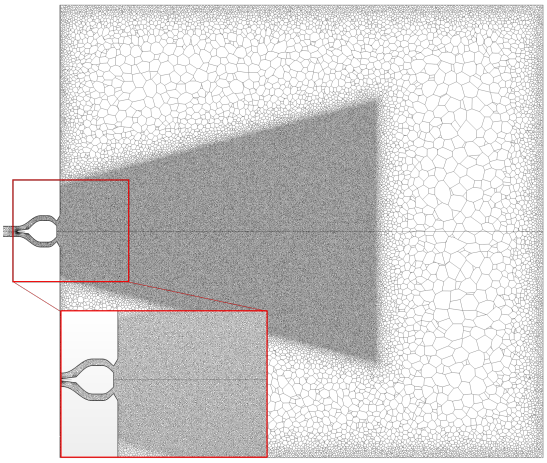

Figure 4.4: Base Mesh with Refinement Volume

is exported using a 500×500 representation grid, shown in Figure 4.5, structured in a way to match the PIV data, which facilitates the parameter extraction process, the comparison, and the validation.

Figure 4.5: Representation Grid for Extracting CFD Data

4.6. CFD Model Validation and Sensitivities

Model validation and sensitivity analyses are essential to ensure the accuracy and reliability of CFD simulations. The validation involves comparing the simulation results to experimental data or validated numerical simulations, ensuring the model accurately represents the physics of the phenomenon studied. While the sensitivity analysis reveals how changing the model's input parameters affects the outcome.

4.6.1. Turbulence Model Validation

Free shear flows are among the most challenging flows to simulate using CFD. The jet characteristics are direct functions of the jet's turbulence generation and dissipation behavior. These are triggered by the instabilities in the shear layer, which enhanced mixing. The instabilities range

from small to large scales, with the small scales significantly contributing to defining the overall jet statistical characteristics. For this reason, an investigation is carried out to assess the influence of the turbulence model on the jet behavior and identify the most promising model for predicting the confluent twin jets and their development. This investigation focuses more on RANS models, especially the two (and higher) equation eddy viscosity models, as they offer relatively lower computational costs and are more suitable for industrial applications than their counterparts. This study uses the converged mesh obtained from the following grid sensitivity study.

Before exploring various eddy viscosity models, the author sought to validate the accuracy of RANS simulations in general in capturing intersecting jets. This was done by comparing RANS results to analytical and experimental data. To conduct this validation, the standard $k-\omega$ SST turbulence model is chosen due to its popularity and versatility for a range of flow problems. As the research aims to identify the most appropriate RANS model and settings for simulating intersecting twin jets, a more detailed analysis of turbulence model sensitivity will be presented in an upcoming chapter of the paper. The simplest possible flow configuration was selected for the RANS validation run, with a 0° jet angle to ensure any unsteady effects due to the bias flap wake on turbulence model predictions are decoupled. The default $k-\omega$ SST model coefficient values in STAR-CCM+ are used for this run. A preliminary run is conducted and confirmed that the selected turbulence model performs directionally correctly when compared to experimental data. The results of this run are implicitly presented through the following grid and inlet turbulence intensity sensitivity sections.

4.6.2. Grid Sensitivity

Shear flows are characterized by high-velocity gradients normal to the bulk flow direction, forming vortices and turbulent structures which affect the bulk characteristics of the jet itself. This renders highly sensitive flows to the smaller length scales captured in the flow field. Minor changes in the mesh resolution can lead to significant differences in the predicted mean flow behavior; hence, a fine mesh is required to accurately capture the small-scale eddies that are seen to be cascading and affecting the large-scale coherent structures. Additionally, shear flows can be unstable, and the growth of instabilities can lead to numerical errors and divergence of the simulation, mandating a properly resolved domain to ensure numerical stability and prevent the formation of spurious oscillations. Air jets typically emanate from nozzles and abruptly enter regions of quiescent air, making the flow behavior strongly dependent on the inlet conditions; this stipulates proper resolution of the boundary layer where the velocity profile changes rapidly near the wall. With the previously mentioned concerns, it becomes apparent that selecting an appropriate grid for the computational model of the present setup is crucial for accurate results. This motivated performing a grid sensitivity study using the five different grids summarized in Table 4.2. The assessed grids represent permutations of the domain's base cell size and the cell size of the refinement volume, starting at 8 mm base cell size and reducing that down to 2 mm, while the refinement cell size sweep started at 4 mm and reduced down to 1 mm for the highest resolution grid. The performances of the different grid candidates are assessed based on their capability to predict the centerline velocity decay and the half-width growth of the free twin intersecting jet at $MFR = 0$. This is considered to be the configuration with the least complexity for the setup in hand, making it a good benchmarking case. First, a quick validation is done on the obtained experimental data by comparing the same parameters to the analytical solution found in the literature. Elbanna in [50], proposes an analytical solution for the centerline velocity decay of intersecting parallel jets, which the current setup could assume to be due to the small spacing distance between the two outlets of

Table 4.2: Free Intersecting Twin Jet Literature

Grid ID	Base Cell Size [mm]	Refinement Cell Size [mm]	Cell Count
G1	8	4	2M
G2	4	2	8M
G3	2	1.5	25M
G4	4	1	40M
G5	2	1	50M

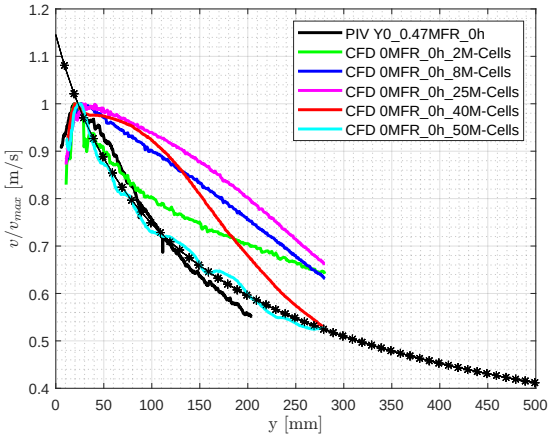

Figure 4.6: Grid Sensitivity, Decay

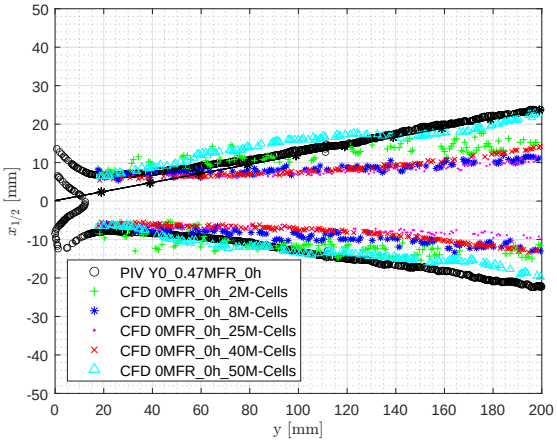

Figure 4.7: Grid Sensitivity, Spread Rate

the nozzle. This analytical solution is expressed mathematically by the following.

$$U_c = \sqrt{y_{cp} + y_o} \cdot (y + y_o)^{-0.5} \tag{4.16}$$

where, U_c is the centerline velocity, y is the streamwise distance, y_o is the virtual origin location for the twin-jet. The virtual origin is evaluated using (2.3.1.3). The first term represents a scaling factor to offset the decay curve and account for the shift of the maximum centerline velocity location from the nozzle outlet for a single jet to the combined point in the case of intersecting jets. The combined point, in this case, is estimated from the experimental data to be around 20 mm. To get a decay curve that is normalized by the centerline maximum velocity, this term is written to evaluate to 1 at the combined point. Similarly, the half-width experimental results are compared to the empirical solution obtained using (2.23) proposed in [50]. The trends of the experimental decay seem to show a very high correlation with the empirical solution, with the absolute values discrepancy reaching about 10% across the velocity decay profile. This discrepancy is expected and considered marginal, given the analytical curve is scaled from fitting the centerline decay curve of a single jet. The half-width growth obtained from PIV also demonstrated a very decent correlation with the analytical solution as the jet started behaving similarly to a single jet beyond the combined point.

On the same plots, solutions of the different grids are overlaid in Figure 4.6 and Figure 4.7, showing a considerably high sensitivity of the jet flow to the mesh resolution. It is apparent from the plots presented that a strong correlation exists between the predicted spread rate of the jet and its corresponding centerline decay profile. **G1**, with the coarsest grid, shows a mismatching trend of the centerline decay, whereas, increasing the grid resolution gradually corrects this mismatch

by showing better trend alignment. The centerline velocity profile does not conform with the experimental data until **G5** is used employing a 1 mm cell size in the refinement volume and 2 mm across the rest of the domain, including the flow inside the nozzle. The corresponding half-width growth profiles also indicate a sufficient correlation between the **G5** grid and the experimental data, with marginal instabilities appearing locally, which could be attributed to the deficient iteration averaging. Conclusively, grid **G5** is proved to be sufficient to capture the turbulent twin jet's statistical characteristics. Refining the grid further showed minimal improvement (results not presented in this paper), suggesting the mesh convergence for this study at **G5**.

4.6.3. Turbulence Intensity Sensitivity

As implicitly shown by the mesh sensitivity study, the way subsonic turbulent jets behave is highly sensitive to their onset conditions which motivated the author to investigate the response of the twin intersecting jet to various inlet turbulence intensities. Turbulence intensity (TI) is a parameter that measures the local velocity fluctuations in relation to the mean velocity by calculating the root mean square, mathematically expressed as in (4.17)

$$TI = \frac{\sqrt{u'^2 + v'^2 + w'^2}}{U_o} \tag{4.17}$$

For the readers reference, high-turbulence flows (5% < TI < 20%) involve rapid flows within intricate geometries such as heat exchangers and rotating machinery. Medium-turbulence flows (1% < TI < 5%) appear in less complex flows such as large pipes or ventilation systems, or low-speed flows with a relatively low Reynolds number. Low-turbulence flows (TI < 1%) are characterized by fluid flows originating from stagnant sources, such as external flows around aircraft and vehicles or high-quality wind tunnels that can produce extremely low turbulence levels. The turbulence intensity sensitivity exercise is conducted by aggressively ranging the specified inlet TI from 1% to 10% to 50%, large increments are used to signify the effect of turbulence on the jet flow since the flow travels through a number of aggressive contractions which dampens the turbulence in the flow before it exits to ambient. It is important to note that these runs are all performed using an eddy viscosity RANS model, which assumes isotropic turbulence, making the effect of TI more pronounced. The variation in the mean behavior of the jet represented by the centerline velocity and half-width growth profiles is monitored for the different intensity percentages. By observing the turbulence intensity profiles in Figure 4.8 and Figure 4.9, it can be noticed that increasing the specified inlet turbulence intensity from 1% to 10% leads to an increase in the instability of the jet, introducing high-amplitude low-frequency oscillations to the centerline profile. Further increasing the inlet TI to 50% shows no impact on the amplitude of the oscillations from the 10% case; however, these oscillations become of lower frequency indicating a less stable jet. Comparing the velocity contours of the three different cases, in Figure 4.10, shows that increasing the turbulence intensity of the jet potentially increases the mixing between the jet and the surroundings leading to a faster breakup of the jet core, as indicated by the arrows. This could be explained by the higher dissipation rate of the jet's kinetic energy as large-scale eddies form in the jet, yielding a more unstable jet that is more susceptible to external disturbances. This study manifests the significance of carefully selecting an appropriate inlet turbulence intensity value for representative CFD results. Turbulence intensity ranges could be obtained from either experiments or literature on a certain application. The previous sensitivity studies encourage using the G5 grid and 1% inlet turbulence intensity settings for the rest of the CFD runs performed in the current work.

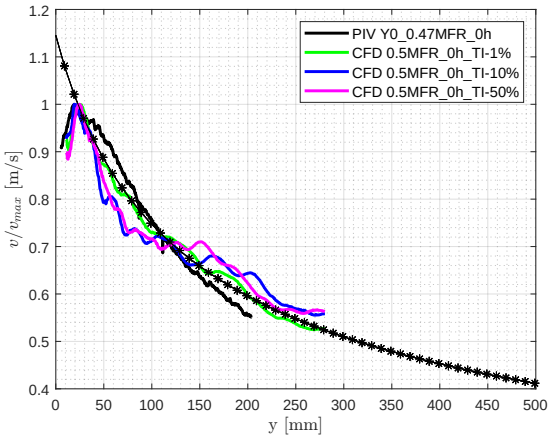

Figure 4.8: TI Sensitivity, Decay

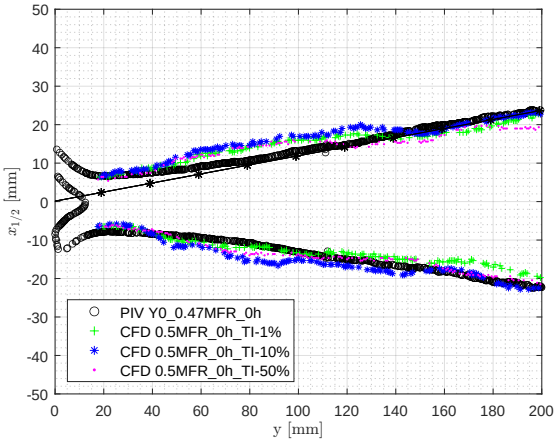

Figure 4.9: TI Sensitivity, Spread Rate

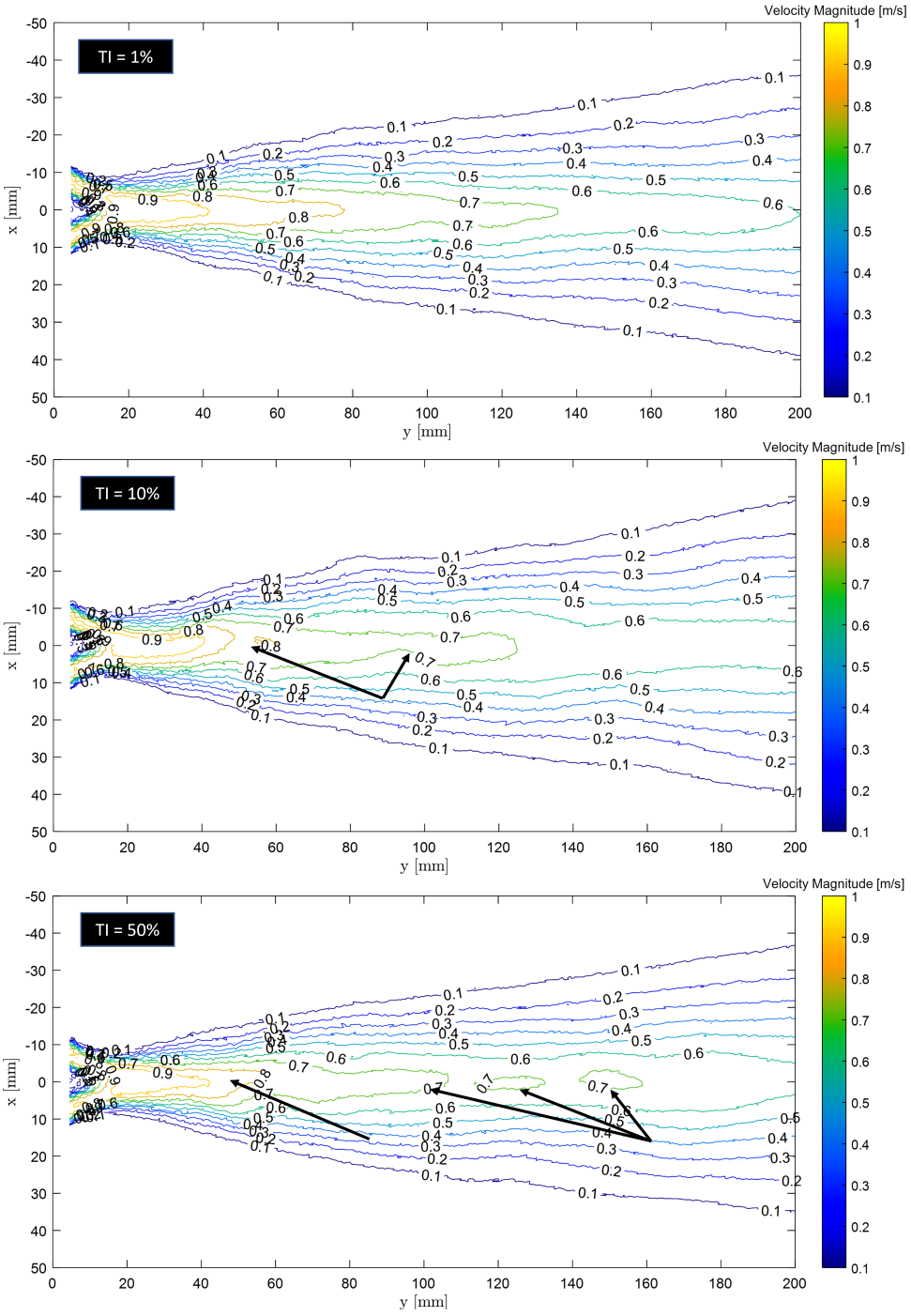

Figure 4.10: Inlet TI Sensitivity - Velocity Contours

5

Results & Discussion

5.1. Free Dual Intersecting Jets

5.1.1. Mean Flow Fields and TKE

The mean flow fields obtain from the PIV measurents show the following; similar to a single jet, When a fluid jet exits a nozzle, there is a sharp gradient in the velocity between the jet and the surrounding air, forming a shear layer at the interface between the two. This shear layer is a region of rapid velocity gradient, with a significant difference in the velocity between adjacent fluid layers. This velocity gradient causes a stretching effect on the fluid particles, which leads to the formation of vortices in the shear layer. the retrograde (counter-clockwise) and prograde (clockwise) vortical structures are formed along the jet shear layers due to Kelvin-Helmholtz instability. The strength of these vortices depends on several factors, including the jet's velocity, the nozzle's diameter, and the fluid's density and viscosity. These vortices tend to diffuse towards the jet centerline downstream of the potential core region. The formation of vortical structures across the jet's shear layers causes the high momentum flow on the jet centerline to advect towards the shear layers and the ambient fluid to be entrained into the jet envelope. The details of these turbulent structures and streaks are fading in the flow field contours in Figure 5.1 as a result of time-averaging. The highest vorticity across the jet is observed at the mixing layer between the potential core of each of the the jets and their boundaries at the nozzle exit, indicating a highly rotational flow region with steep velocity gradients; this is confirmed by plot (b) in Figure 5.1. The vorticity profile also shows that the lower negative and top positive vorticity regions of the individual jets, resulting from the symmetry of the velocity profile about the jets' centerline, vanish as the jets merge, indicating that the combined jet starts behaving similarly to a fully developed single jet.

The turbulence behavior of the intersecting twin jets is identified using the turbulence kinetic energy (TKE) contour. Since TKE is a measure of the kinetic energy associated with the velocity fluctuation per unit mass of flow, it is a metric that is commonly used to monitor the mixing performance of the jet. The third contour plot in Figure 5.1 shows that the TKE is at its highest near the nozzle outlet, specifically the region between the merging region of the twin jet, indicating a strong interaction between the two jets. Two considerably high TKE peaks are also noticed between the individual jets' potential cores and the outer shear layers. These peaks monotonically grow in width as the jet progresses until they merge at the jet centerline downstream of the combined jet core before dissipating. The profile also shows that the two TKE peaks are symmetric about the jet centerline and almost identical in size and magnitude. The decolored band apparent near the 100 mm y-position is an artifact due to the post-processing of the overlap region of the two flow fields using the side-by-side camera function in DaVis.

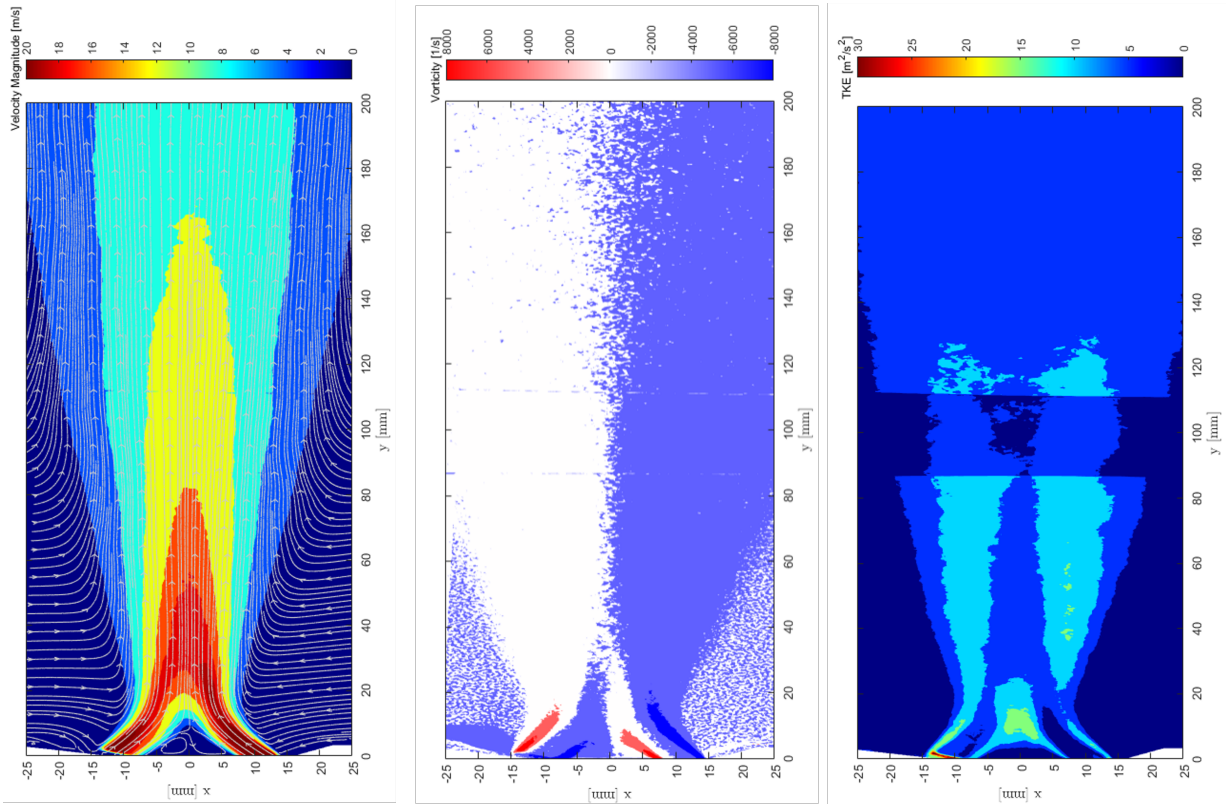

Figure 5.1: (a) Mean Velocity (b) Mean Vorticity (c) TKE Contours

The lateral velocity distribution normalized by the centerline velocity at multiple locations along the jet axial direction is plotted against the jet half-width to realize the jet self-similarity in Figure 5.3. The onset of the self-similarity range is observed to be approximately 1.6 nozzle heights (d) downstream of the outlet. Observing the velocity deficit profiles shown in Figure 5.2, the double velocity peak profile could be identified near the outlet, with the peaks gradually merging into one as the jets develop. The location of the maximum velocity for the single-peak profiles corresponds to the combined point, which based on the plot, falls somewhere around 19 mm. This streamwise location matches that of the centerline velocity decay peak in Figure 4.6.

5.1.2. Jet Centerline Velocity Decay and Spread Rate Variation with MFR

Varying the flap located on the back side of the nozzle splitter allows controlling the mass flow ratio across the two nozzle channels by effectively gradually closing one channel and biasing the airflow to the other channel, as explained earlier. The PIV measurements acquired for various flow ratios are post-processed to generate the centerline velocity decay and half-width growth profiles in Figure 5.4 and Figure 5.5, respectively. The decay profiles show that reducing the MFR increases the centerline velocity decay rate. When observing the flow fields of these cases, the effective minor axis height at the combined point location is reduced with lower MFRs as the combined jet approaches a single jet emanating from a single outlet. This height reduction increases the jet's aspect ratio (reduces eccentricity). Referring back to the literature plot showing the variation of the characteristic decay region decay exponent with eccentricity in Figure 2.6, it can be seen that below eccentricity of 0.1, the decay exponent increases as the eccentricity approaches 0. The twin-jet effective ratio is (28/450 = 0.06 < 0.1); hence the single-channel jet would have a higher

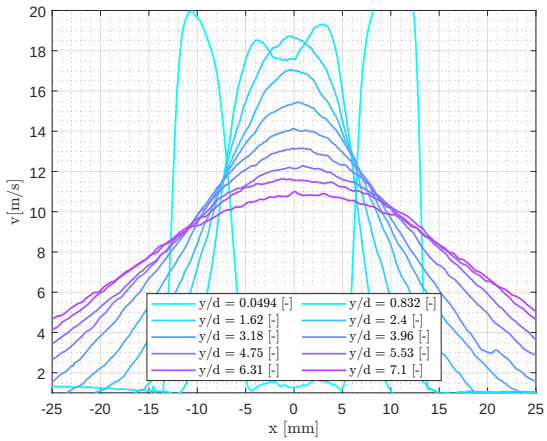

Figure 5.2: PIV - Velocity Deficit Profile

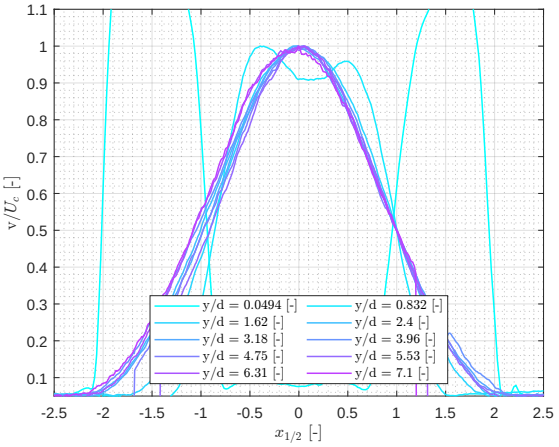

Figure 5.3: PIV - Self-Similarity

n-exponent value and higher characteristic decay rate. It is important to note that higher decay does not indicate lower velocity at a given streamwise position. As the MFR approaches 0, the potential core of the near single jet becomes prominent, extending to about 7w downstream of the nozzle.

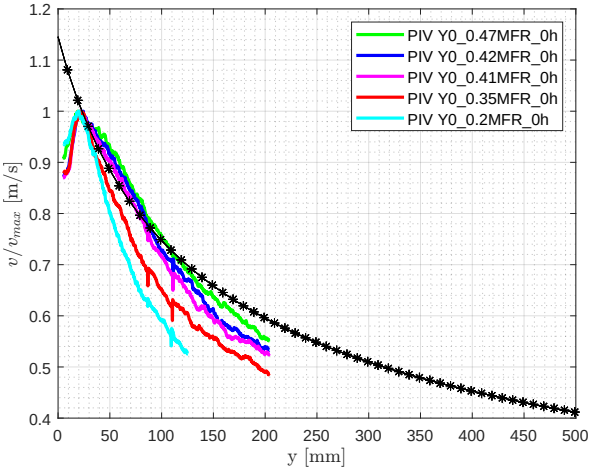

Figure 5.4: PIV - Centerline Velocity vs MFR

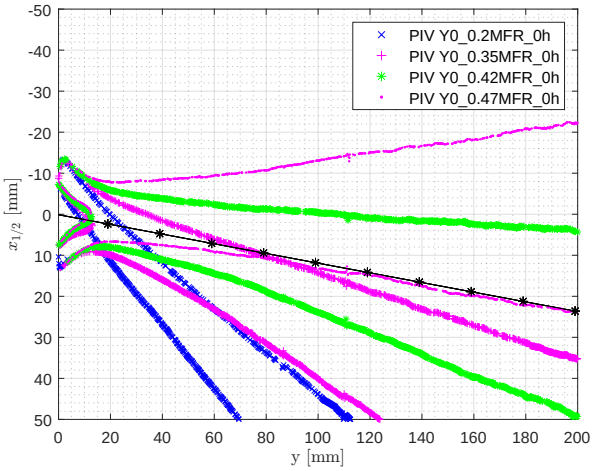

Figure 5.5: PIV - Half-width growth vs MFR

5.1.3. Twin Jet Characteristic Locations

I. Merging Point and Vortex Core Points

As previously explained, the merging point is defined as the location where the inner shear layers of the two jets first intersect, resulting in a zero velocity point. In order to identify this point for the current setup, the $0\,\mathrm{m\,s^{-1}}$ u and v velocity isolines are extracted. The intersection of these two curves yields three points; the point along the jet centerline and the furthest away from the nozzle in the streamwise direction is the merging point. This point is critical to track as it represents the onset of the interaction between the two jets. Additionally, downstream of this point, the centerlines of the two individual jets deflect toward one another until they intersect at the combined jet centerline. Delaying the occurrence of this point could be beneficial in a sense as that would also delays the streamwise position at which the peak velocity takes place when the centerlines of

the two individual jets intersect. Between the inner shear layers of the two jets exists a region of counter-rotating vortex cores resulting from the entrainment of the air in this zone. The stability of the merged jet is a strong function of these vortices' strength and cores' stability. For this reason, tracking the location of these cores and the variation in their position with the mass flow split became interesting to the author. It can also be seen from Figure 5.6, that the zero velocity isolines intersect at two locations other than the merge point located across either side of the jet centerline. These intersection points represent the upper and lower vortex core locations. Figure 5.6 elucidates the shift experienced by these points as the mass flow ratio is varied. One key observation to be made here is the earlier merging of the jets at lower MFR. Moreover, the size of the vortex on the side of the jet deflection shrinks relative to the other vortex. This is evident from the vortex core shifting closer to the nozzle outlet.

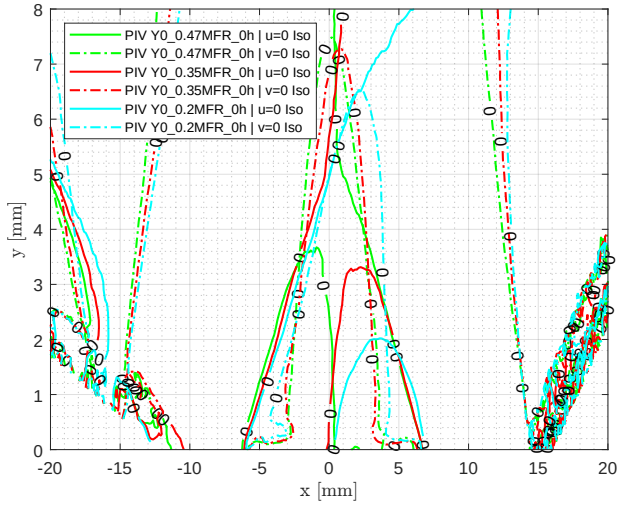

Figure 5.6: PIV - Merging Point Example

II. Combined Point

Slightly downstream of the merging point lies the combined point. As discussed in Section 2.3, this is the streamwise point where the combined jet starts as the centerlines of the two individual jets intersect, reaching its maximum streamwise velocity. The combined region of twin intersecting jets behaves analogously to the characteristic decay region of a single jet, where the decay behavior is a function of the geometry of the jet. With varying the MFR, the merging of the two inner shear layers of the jets is skewed in the x-direction towards the weaker jet in, as apparent in Figure 5.6; this, in turn, as predicted, shifts the combined point of the jets in the same direction. The variation in the combined point location obtained from the PIV measurement is overlaid on the velocity contour plots for the different MFR in Figure 5.7. These plots suggest that the combined point's x-position is more sensitive to MFR than the y-position.

5.1.4. Control Curves

Further validation of the PIV results is done by computing the flow rate split ratio between the two outlets and plotting that against the combined jet angle yielding the red curve in Figure 5.13. This curve is compared to the analytical solution for the deflection angle of two intersecting confluent jets presented by Elbanna in [50]. The analytical solution proposed by ELbanna and addressed in Section 2.3.2 is tweaked to match the MFR and jet angle conventions followed in this study

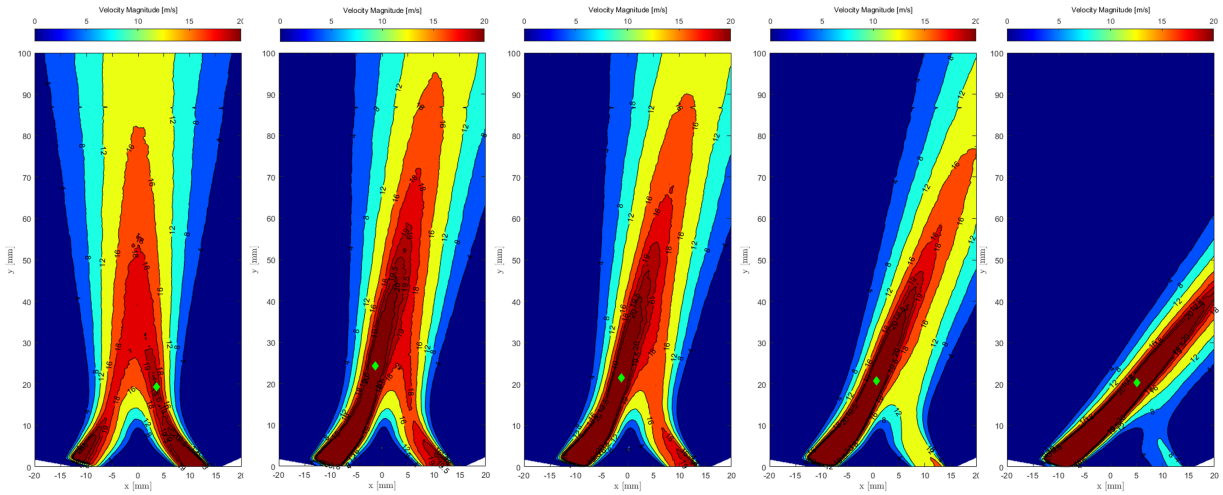

Figure 5.7: Combined Point Variation with MFR

resulting in the curves shown in Figure 5.12. The $\alpha = 45°$ is the one that describes the test subject configuration, hence used for validation. Figure 5.13 suggests that the trends of the two curves match; however, the black solid line would be obtained with simple momentum considerations assuming zero net pressure force acting on the flow field. Mutual air entrainment by the two jets creates low pressure upstream of the merging region, providing a transverse force tending to increase the deflection angle. Nonetheless, due to confluence, high pressure is developed in and near the merging region, adversely affecting the deflection angle. The present results show a slightly smaller deflection angle than what the potential flow suggests as a net effect of the pressure field of the two merging jets. Similar behavior has been noticed in the experimental work of Foss [91] displayed in the work of Elbanna [50]. This behavior is, however, expected to vanish as the MFR approaches zero, and the flow field comprises just a single jet emanating to the ambient at $\theta = 45°$. The measurement points available only cover MFR as low as 0.2, preventing demonstrating the region where the experimental and theoretical control curves collapse.

5.1.5. Jet Two-Dimensionality and Reynolds Dependency

In order to validate the two-dimensionality of the current setup, measurements of the same settings are acquired at three different spanwise locations of the test subject. The laser sheet was shifted to 20 mm along either direction of the geometric center. The half-width growth and velocity decay profiles obtained at two planes are overlaid in Figure 5.8 and Figure 5.9, respectively. The profiles match fairly closely; the slight discrepancy appearing on the half-width profiles is explained by the roll angle mismatch between the two measurements. Such measurement errors result from moving the laser and cameras throughout the test for capturing more than one plane. This suggests avoiding varying the instrumentation location for a given test when possible.

Similarly, for the z=0 spanwise location, the fan speed is varied to vary the outlet velocity $U_{o1} = [10, 15, 25]$ to confirm the jet behavior independency of the Reynolds number. The results in Figure 5.11 show the variation of the velocity deficit profiles of the same jet at different Reynolds numbers. The velocity profile development follows the same trend for the three Reynolds number and is only amplified for the higher-velocity jet. The non-dimensionalized growth rate for the three jets of different speeds, shown in Figure 5.10, seems to collapse very closely, indicating the Reynolds number independence of the mean flow characteristics of the jet.

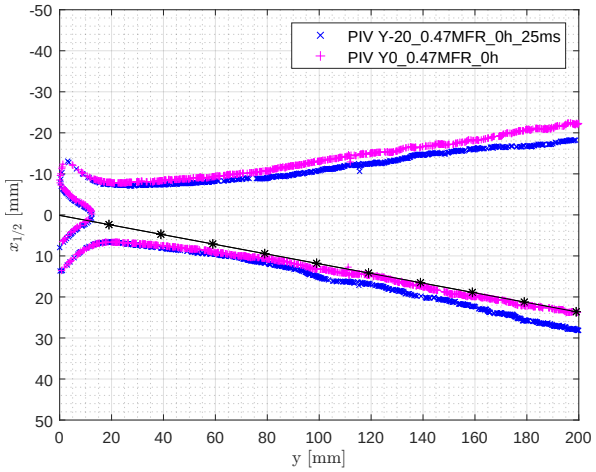

Figure 5.8: Two Dimensionality - Half-Width Growth

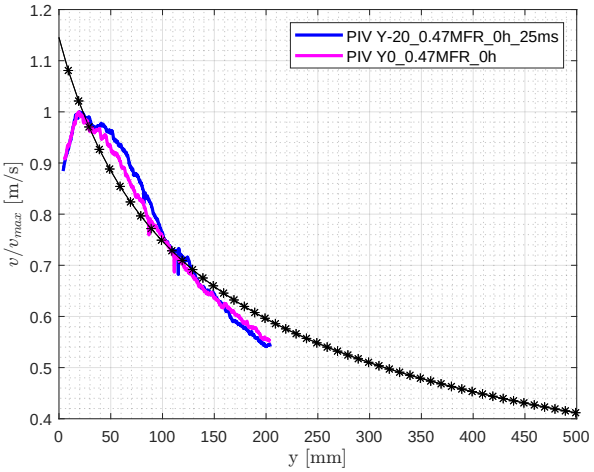

Figure 5.9: Two Dimensionality - Velocity Decay

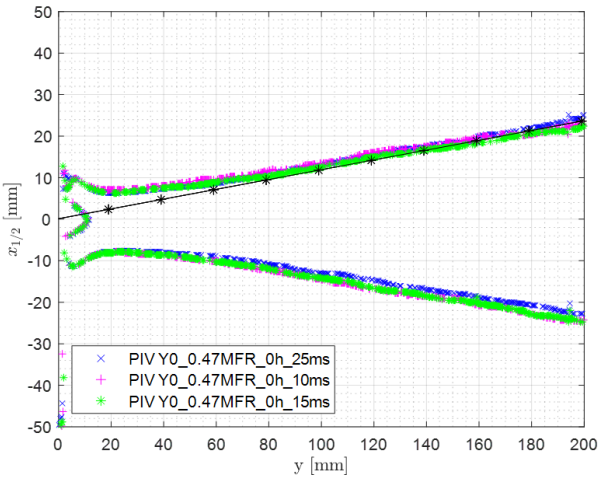

Figure 5.10: Re Dependency - Half-Width

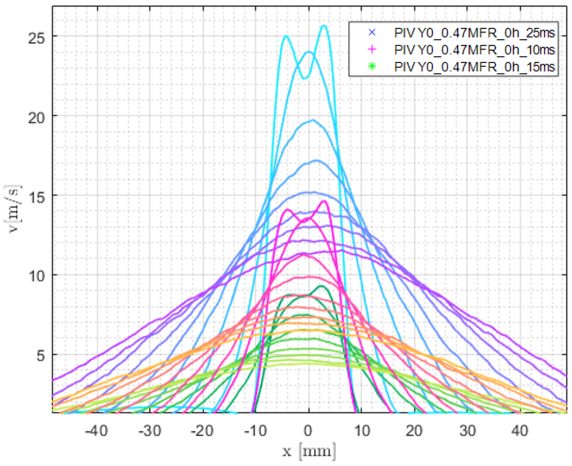

Figure 5.11: Re Dependency - Velocity Deficit

5.2. Installed Dual Intersecting Jets

A flat plate is introduced to the test setup to imitate the effect of a vehicle's interior surface on the control authority of an air vent of the previously described configuration. Although the flat plate is an idealized version of the vehicle's interior surfaces, it still serves as a decent representation for capturing the physics involved in the jet-surface interaction. The test setup is designed to allow sliding the flat plate into a slotted vertical mount integrated with the nozzle geometry. This allows the flat plate to be mounted parallel to the axial direction of the nozzle outlet with the flexibility to vary the offset distance between the plate and the nozzle outlet. The slot locations on the mount are spaced at [7,14,21,28,35] mm, measured from 38 mm below the nozzles geometric center as illustrated in Figure 3.5. The previously described test is performed with the plate installed at the different offset positions. PIV measurements are acquired while incrementally varying the mass flow ratio to identify the deflection angle the jet experiences relative to its uninstalled case counterpart.

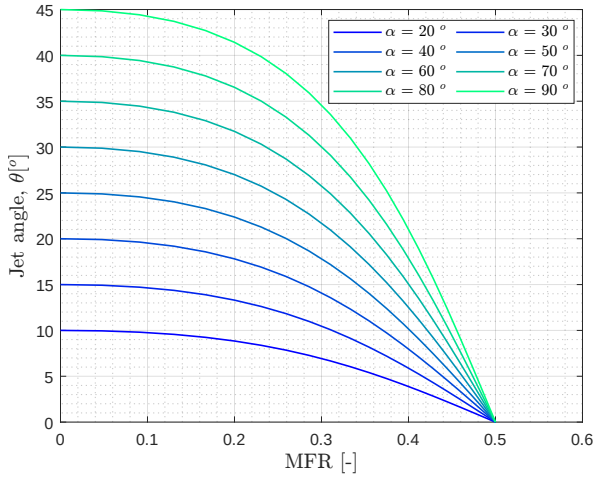

Figure 5.12: Jet Deflection Mass Flow Ratio

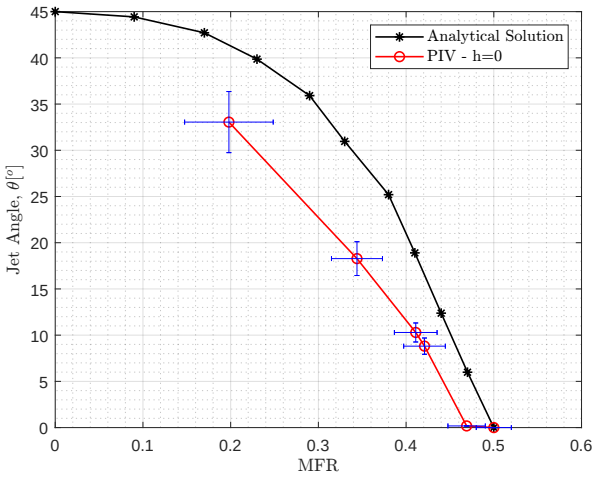

Figure 5.13: Uninstalled Control Curves

5.2.1. Installation Effect on Mean Flow Field and TKE

In order to accentuate the influence of placing a flat plate tangential to the streamwise direction, the case of MFR$\sim$ 0.5 is chosen to discuss the alteration to the flow field. The velocity contour of the flow field obtained from the experiment is shown in Figure 5.14 and overlaid with streamlines. The streamlines help manifest a few important flow features, the first being the two counter-rotating vortex cores inscribed between the two jets and the standoff wall. Moreover, the air entrained by the jet is apparent by the streamlines traveling perpendicular to the streamwise direction and abruptly getting dragged by the jet as they approach the boundary. Tracing these streamlines can be seen as they stack on top of each other as the jet progresses, creating a thicker layer of lower velocity (the intermediate blue shade region). Unlike the uninstalled jet case, the entrainment behavior on the jet's top and bottom sides becomes asymmetric due to the plate limiting the entrainment on the near-wall side of the jet. Additionally, a circulation bubble appears between the bottom shear layer of the combined jet and the wall. Like the uninstalled cases, the vorticity profile shows that the highest z-vorticity occurs as the two jets leave the nozzle, with the individual's lower negative and top positive vorticity layers jets merging as the jets combine. For this installed case, however, the vorticity contour shows that the flow field in the converging and merging region of the twin jet is almost identical to that of the uninstalled jet. However, shortly downstream of the combined point ($\sim$y=25 mm), the interface between the positive and negative vorticity layers of the combined jet starts deflecting towards the wall. This plot also shows that the spread rate of the bottom half of the jet closer to the wall is suppressed relative to the top half, confirming less entrainment. The TKE contour structure is similar to the one associated with the free jet. A significant discrepancy could, however, be seen in the mismatch between the double TKE peak sizes. Plot (c) in Figure 5.14 shows that the jet curvature led to the elongation of the TKE band further from the wall while compressing the length of the near-wall band. Consequently, the widths of each of the bands changed accordingly to ensure the conservation of kinetic energy.

5.2.2. Installation effect on Jet Centerline Velocity Decay and Spread Rate

The velocity contour plots obtained from the PIV experiment reveal that the installation of the flat plate results in a low-pressure region trapped between the jet shear layer and the flat plate surface. This region's boundary behaves like a curved hydrodynamic wall; the jet attaches to this boundary and follows it until it intersects the plate. This mechanism deviates the jet angle from its

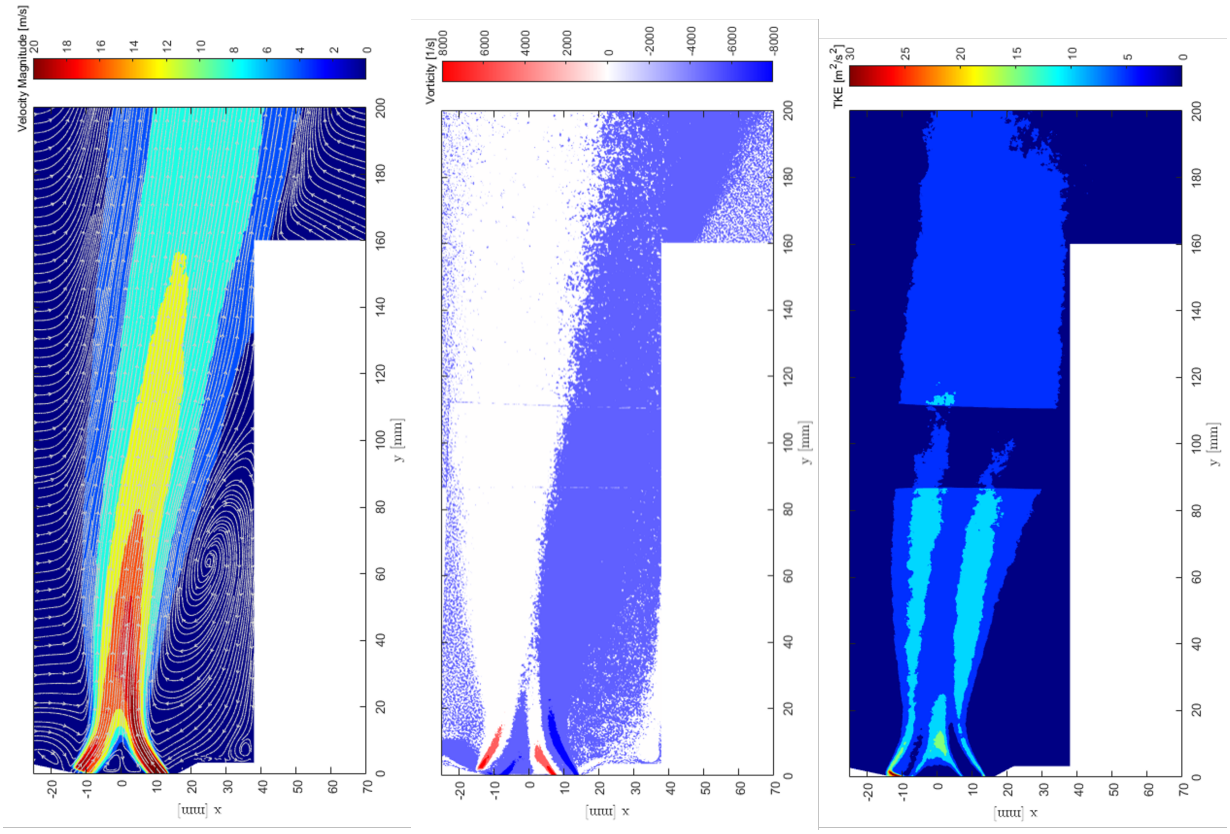

Figure 5.14: (a) Mean Velocity, (b) Mean Vorticity, (c) TKE Contours, for MFR = 0.5 and h=7

uninstalled counterpart for the same MFR.

As the installation surface offset distance is varied in the experiment, the measurements elucidated a non-negligible dependency of the centerline velocity profile on the offset distance. The centerline velocity profiles collapse for the different tested offset heights until about $y = 100\,\text{mm}$ downstream of the nozzle outlet as shown in Figure 5.15. At this streamwise position, the centerline velocity decay curve of the $h = 14$ case shows a sudden increase in the decay rate that quickly recovers at about $y = 150\,\text{mm}$. The range at which the decay rate increases starts at the location where the jet approaches the wall surface after passing the vortex core till the point where the jet attaches to the wall. The reduction in the jet velocity before attachment results in a pressure rise across the jet, with that reaching its maximum at the reattachment point (stagnation point). After the jet attaches to the wall, it accelerates due to the favorable pressure gradient along the wall starting at the reattachment point. As discussed in Section 2.4, once attached to a nearby surface, the jet starts behaving similarly to a wall jet. Since the main contributor to the jet velocity decay is the advection of the momentum from the centerline to the jet boundary, higher velocity gradients at the jet boundary motivate higher momentum transfer. In the wall jet case, the gradient across the wall-attached boundary is higher than in the case of a free shear, enhancing the momentum transfer and resulting in a higher jet decay rate which negates the gains by the favorable pressure gradient. This explains the equivalence in the decay rate of all profiles beyond $y = 150\,\text{mm}$. Although the plot in Figure 5.16 shows variation in the shape of the half-width growth curves with respect to the installation offset distance, the size of the width-growth profile is hardly affected. The variation in the form of the half-width profile is predicted as it follows the jet deflection, being the most severe for the lowest offset distance and reducing as the installation surface is moved further.

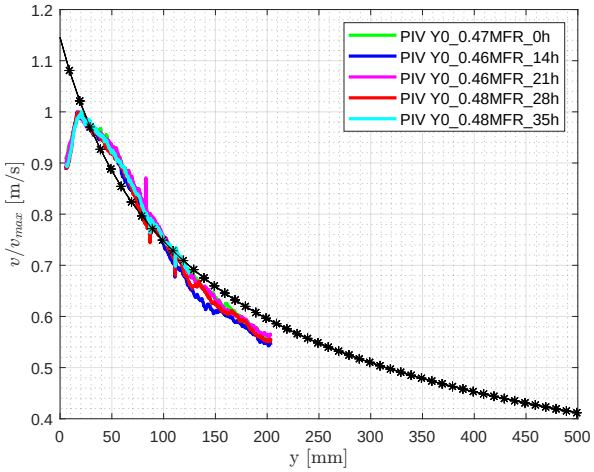

Figure 5.15: PIV - Centerline Velocity vs h

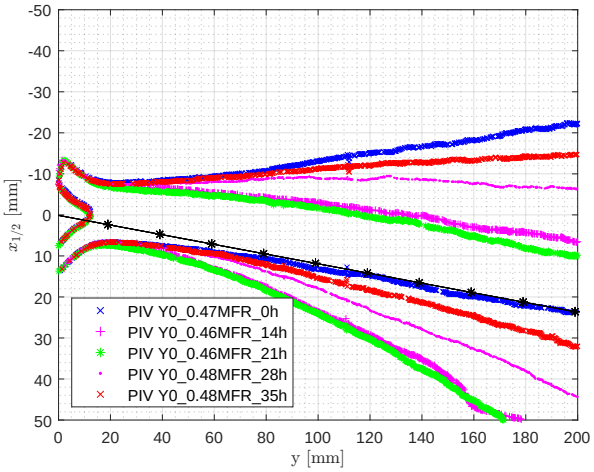

Figure 5.16: PIV - Half-width growth vs h

5.2.3. Installation effect on Twin Jet Characteristic Locations

I. Merging Point and Vortex Core Points

The mean flow fields for the MFR= 0.5, $h = 7$ case examined, showed a minimal disparity in the twin jet's converging region compared to the MFR= 0.5 uninstalled case suggesting marginal impact of the installation surface on the jet's merging point and vortex cores. This observation is confirmed with the zero-velocity isolines alignment for different offset distances shown in Figure 5.17.

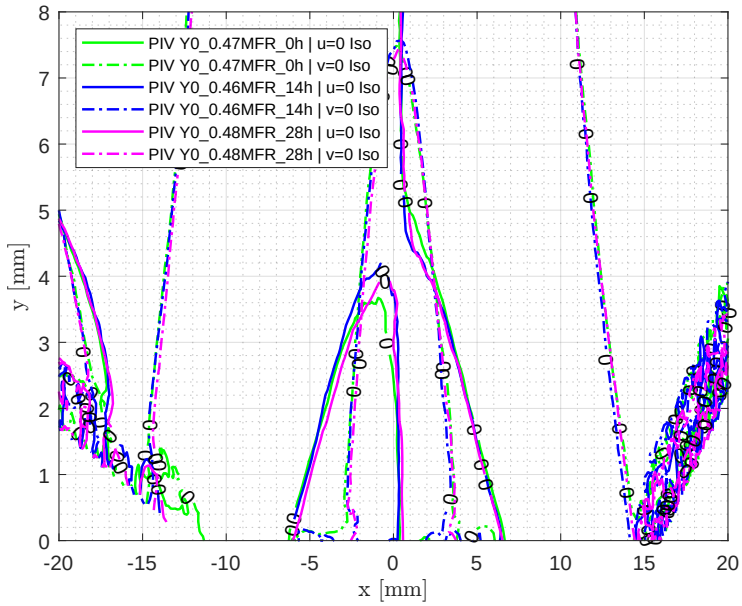

Figure 5.17: PIV - Merging Point and Vortex Cores vs h

II. Combined Point

The combined point streamwise location is tracked for the same MFR and different offset distances to confirm the onset of the jet deflection. The y-position of the combined point seems to show very low sensitivity to the plate position for a given MFR, as shown in Figure 5.18. Similarly, the x-position of the combined point shows little to no variation with offset distance. However,

the skewness of the combined point's x-position, for both the installed and uninstalled cases, is attributed to the imperfection in balancing the mass flow between the two outlets due to the sensitivity of the setup. This finding suggests that the installation does not become remarkable for the tested offset distances until after the jets combine.

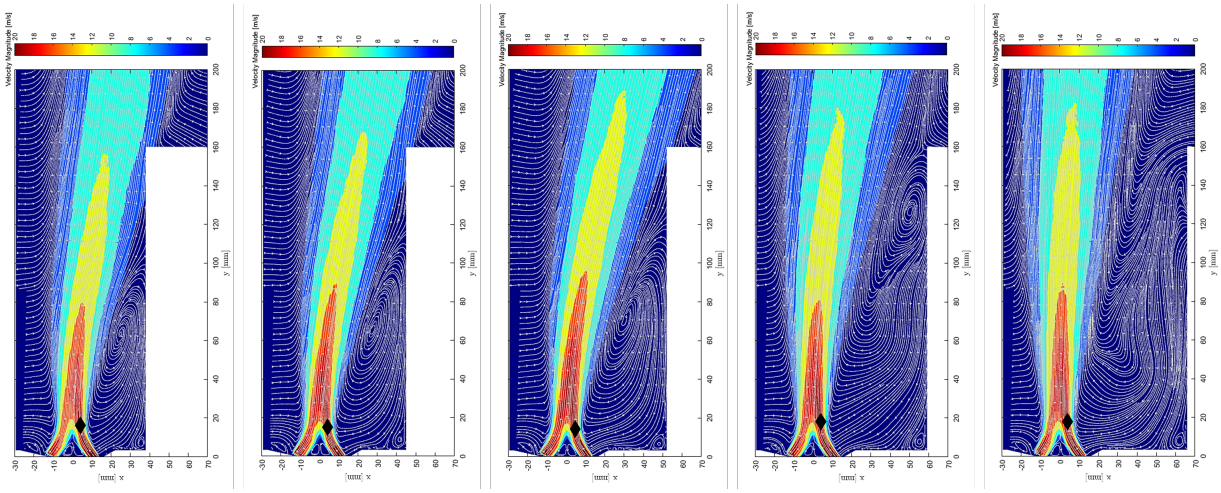

Figure 5.18: Installed Reattachment Point Location Curves - PIV

5.2.4. Control Curves

The sensitivity of the control curve to the offset distance is shown in Figure 5.19. By investigating the $h = 7$ case, It can be seen that for mass flow ratios that are close to 0.5, the control curve shifts in the positive y-axis direction. This suggests an increase in the jet angle for a given MFR and a deviation of the jet from its intended path represented by the $h = 0$ curve. The black arrow highlights the loss of the controllability of the jet imposed by the presence of the plate. This behavior holds for flow split ratios down to 0.3; beyond this point, it could be seen that the profile starts to collapse. By observing the centerline velocity profile, it could be seen that for the $h = 7$ case at these low flow ratios, the jet had already attached to the surface either upstream or within the section of the centerline velocity curve where the jet angle is evaluated. The opposite-direction deflection caused by the jet impingement on the plate, as the jet moves along the plate, reduces the angle of the linearly fitted line, decreasing the evaluated jet angle. This makes the $h = 7$ curve crosses the $h = 0$ close to $MFR = 0.25$. For higher offset distances, the control curves start to gradually move closer in y to the uninstalled curve as the influence of the flat plate becomes less evident. Additionally, the dip observed on the control curves for lower MFR, when the jet is pointed toward the plate, starts to become less distinguishable as the jet impingement y-position on the plate is delayed. It is important to note that even at the highest measured offset distance $h = 35$, the control curve of the jet is still shifted from that at $h = 0$, indicating that the control authority over the jet isn't fully retrieved.

5.2.5. Reattachment Points

The reattachment point on the flat plate is monitored for a better understanding of the installation effect on the jet. As demonstrated earlier in the post-processing section, the reattachment point is defined as the point where axial velocity just above the offset plate switches signs. This point corresponds to the stagnation point on the plate. The plot in Figure 5.20 shows the sensitivity of

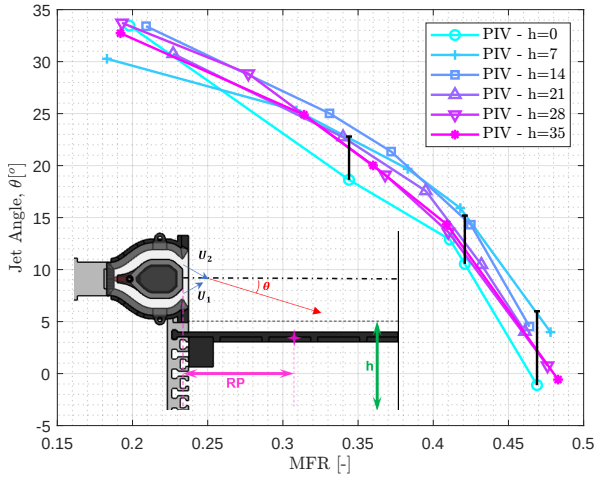

Figure 5.19: Installed Control Curves - PIV

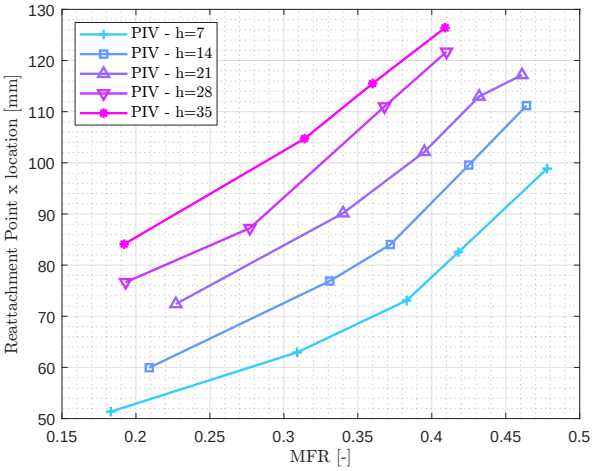

Figure 5.20: Installed RP Curves - PIV

the reattachment point for different MFR jets as a function of the offset distance. The profiles elucidate that for a given MFR, the reattachment point y location (also known as the reattachment length) increases with increasing the offset distance, which could be confirmed through the flow fields in Figure 5.18. The MFR versus reattachment length profiles presented seem to be close to equally spaced for the equally spaced offset distances. This proposes that the reattachment length varies linearly with the offset distance regardless of the jet's MFR. However, the reattachment length varies almost quadratically with the MFR.

5.2.6. Flow Mechanism Leading to Loss of Control Authority

As claimed by the hypothesis and literature on the single offset jet summarized in Section 2.4. As the jet leaves the nozzle it starts entraining the surrounding air. In the case of planar jets or high aspect ratio jets, most of the entrainment occurs along the minor axis direction as the surface area of the top, and bottom shear layers are considerably larger. Placing a plate below the nozzle outlet adds a restriction on how much air mass the moving jet can entrain. This leads to starving that region between the jet and the plate or, in simpler terms creating a relative vacuum in this region. This leads to pulling the jet boundary towards the plate until it attaches. The jet's bottom boundary then impinges on the plate creating a border between the jet's body and the near-triangular-shaped region between the jet and the plate; this border is referred to as the bifurcation line. As a result of the jet entrainment, the air near the edge of the triangular region continues moving along with the jet boundary until it hits the plate and reverses directions moving along the plate's top surface before impinging on the vertical wall to the left and diverting up towards the jet boundary again. More of that air trapped in the triangular region gets entrained again by the jet, and the cycle continues. This phenomenon results in a circulation in the region between the jet and the plate with a core location that varies with the plate offset distance. This circulation is naturally unstable, meaning that it changes size and location slightly over time. The circulation region's instability stems from the jet's instability due to its deviation from the streamwise direction. This deviation increases the centrifugal instability leading to the asymmetric vortex generation on the two sides of the jet [92]. The recirculation region, however, could be statistically averaged by a hump-shaped wall along which the jet's lower boundary travels before it terminates at the wall adjacent to a smaller recirculation region that lies at the bottom left corner of the flow field, where the tangential plate meets with the vertical mounting wall.

By closely observing the structure of the circulation bubble, it can be seen that as the installation surface is pushed away from the nozzle outlet the bubble stretches in both the axial and lateral directions, with the core of the vortex gradually shifting towards the end of the plate following the shift in the reattachment point. In the case of an offset distance $h = 28$, the jet shear layer no longer intersects the plate however, a share of the surrounding air entrained by the jet still impinges on the plate and recirculates in the region between the jet and the plate. This leads to a deformed circulation bubble with a relatively smaller core existing near the end of the plate. Moving the plate further causes this bubble to escape and burst away from the plate surface. The pressure between the jet and the plate is still sub-atmospheric, leading to a slight periodic deflection of the jet, however not strong enough to pull the jet until it attaches to the surface.

It is evident from the previous discussion that the vortex core formation between the jet and the flat plate is the major contributor to the loss of the twin intersecting jet control authority. The suction effect of a vortex core is a natural consequence of the rotational flow within the vortex. As seen from the experimental data, the strength of the vortex and its effect on the jet angle can be influenced by factors such as the size and shape of the vortex core, the velocity of the fluid, and the surrounding flow conditions. Reducing the installation effect on the jet control range requires weakening or suppressing the vortex. This can be achieved by using active flow control techniques by introducing a synthetic jet that disturbs the boundary layer in the attachment region or through external forcings, such as acoustic fields.

5.3. RANS Turbulence Models Assessment

With the goal of identifying the most appropriate turbulence model for simulating intersecting twin jet, a number of turbulence models are assessed. The models investigated are the **standard k – ε**, the **realizable k-ε**, the **k-ω SST** and finally the **RSM**. Each run is performed using the respective model's default coefficient values in STAR-CCM+. Similar to the sensitivity studies presented in the previous chapter, the different models' centerline velocity decay and the half-width growth profiles are compared to the PIV results, as these are the most critical to the author's application. Further assessment of the best-performing candidate's ability to predict the jet development profiles and characteristic points is performed. Next, mass flow ratio and offset height sweeps are carried out using this model to confirm its validity for simulating the interaction between uneven velocity ratio twin jets and for predicting the fluid-structure interaction.

The discrepancies in the performance of the different turbulence models can be attributed to the underlying assumptions and modeling techniques used in each model. The results show that RSM exhibited remarkable agreement with the experimental data as this model considers the full tensor of Reynolds stress, and is generally more accurate for simulating complex turbulent flows, but can be computationally expensive. The $k-\varepsilon$ models show significant inaccuracies as they under-predicted the decay closer to the nozzle outlet as depicted in Figure 5.21. This discrepancy is attributed to the model's isotropy assumption, neglecting anisotropic effects and relying on simple, empirically derived coefficients, leading to significant inaccuracies in simulating complex flows such as the jet flow. Several attempts have been made to modify the standard $k-\varepsilon$ model to remedy a particular class of flows [18], which makes the model less general. The poor near-wall flow treatment is another reason for the deteriorated performance of the $k-\varepsilon$ models. $k-\omega$-SST demonstrated improved performance near the wall than $k-\varepsilon$ resulting in better agreement with the experiment as shown in Figure 5.21. However, the linear assumption of the eddy viscosity with the strain rate still imposed some limitations, leading to less accurate predictions. Surprisingly, the

quadratic constitutive version of the $k-\omega$ SST model, which accounted for the interaction between the turbulence and the mean flow, demonstrated less capability of matching the experimental data's centerline velocity profile.

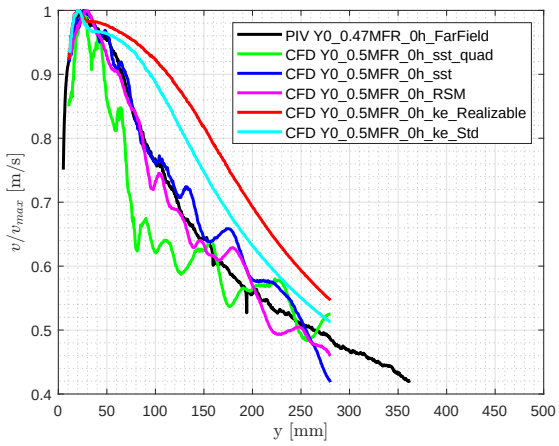

Figure 5.21: TM Study-Velocity Decay

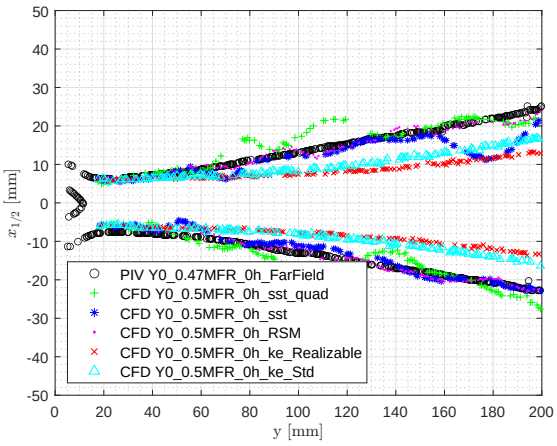

Figure 5.22: TM Study-Spread Rate

To develop further confidence in the $k-\omega$ SST model, the mean flow field obtained from that at MFR = 0.5 is compared to the PIV counterpart. The contour plots in Figure 5.23 confirm that the RSM and SST demonstrate a high level of agreement with PIV data (grey isolines) in predicting the centerline velocity decay as the contour lines with the same value are almost collapsing at the nozzle centerline. Moreover, by observing the spread rate of the outermost contour lines, it could be noticed that the same models demonstrated a much better correlation to the PIV measurement than the $k-\varepsilon$ models which yielded more compact jets.

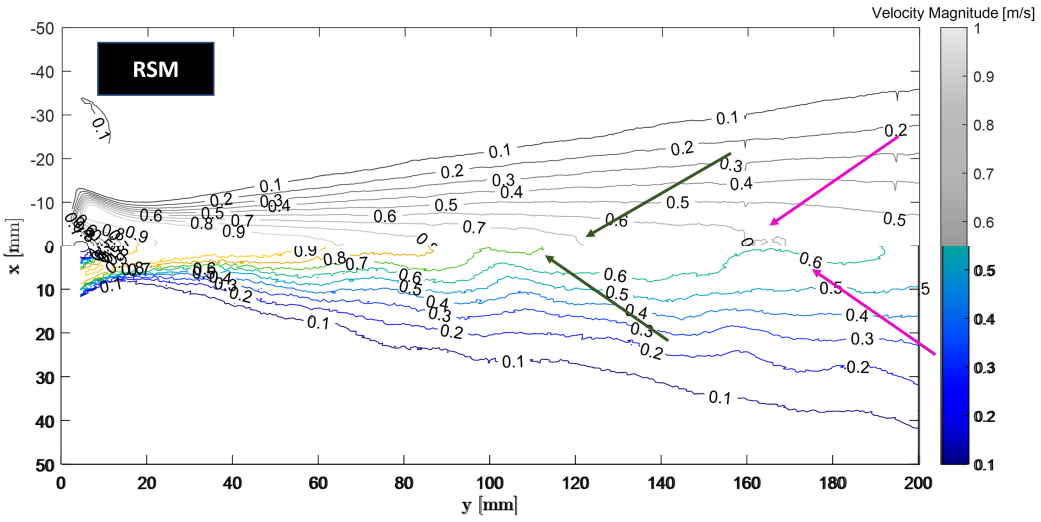

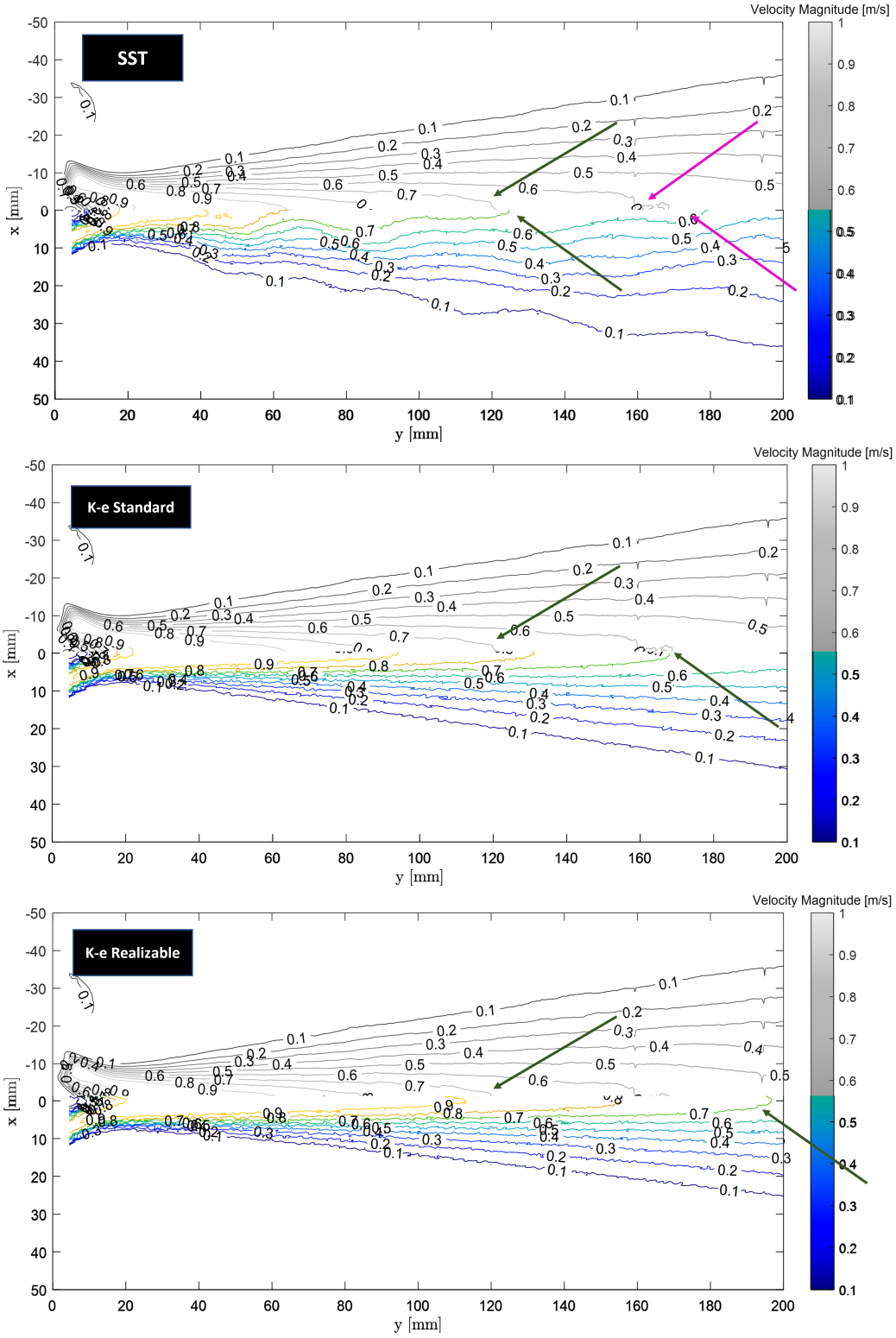

Figure 5.23: Turbulence Models Flow Field Comparison

5.3.1. RANS Model Sensitivity to MFR

The initial turbulence model sensitivity study results show that the $k-\varepsilon$ models struggled to predict the mean flow for the simplest case of MFR = 0.5, which led to eliminating these in the

following studies involving more complex flow dynamics. The substantially higher computational cost of RSM hindered the evaluation of its performance as it is considered unfeasible for the iterative design process. Hence, the $k-\omega$ SST is found to be the most suitable for carrying out the analysis at hand

The $k-\omega$ SST model incrementally sweeps through different mass flow ratios for the uninstalled configuration. The way of varying the mass flow ratio is maintained identical to how it is done with the experimental setup using the flap. The relatively faster simulation turnaround time motivated increasing the sweep's resolution to eight points instead of four experimental data points. The control curve shown in Figure 5.13 is overlaid with the curve obtained from CFD and presented in Figure 5.24. The variation of the jet angle obtained through CFD follows the trend of the PIV and analytical curves sitting somewhere between the two. The CFD profile shows a reasonable agreement with the PIV control curve in the range of MFR= [0.3.5-0.5], which also aligns with the PIV suggestion that the jet angle remains nearly constant for the first 0.05 MFR moving in either direction from MFR=0.5. The CFD curve demonstrates a higher discrepancy from the PIV curve, increasing with lower MFR reaching about a 10% difference in the jet angle at MFR=0.2. The CFD control curve here agrees with the hypothesis that the jet angle should only be offset from the analytical curve when confluence between two jets occurs. As the MFR drops meaning one channel is getting more and more shut off, the jet angle should behave more like a single jet emanating at an angle θ with the horizontal. This outcome grants the author more confidence in the selected turbulence model.

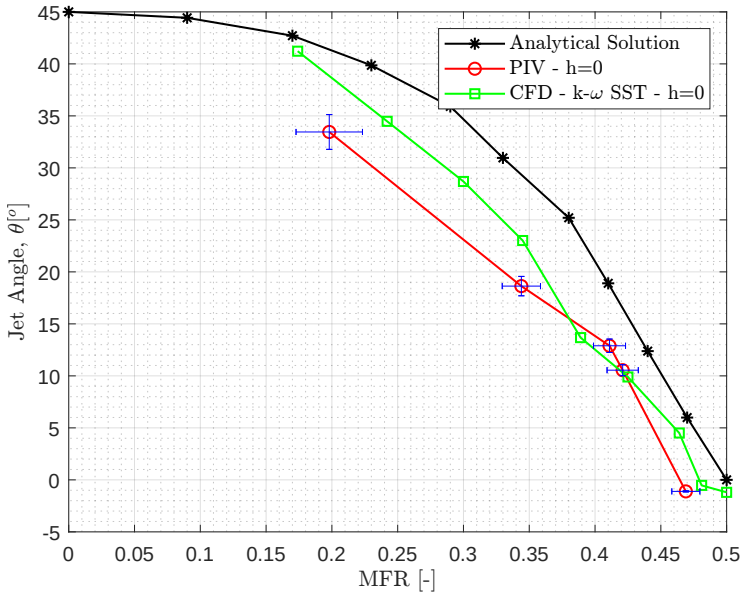

Figure 5.24: PIV vs CFD (k-ω SST) Uninstalled Jet Control Curve

5.3.2. RANS Model Sensitivity Installation

The control curves obtained from the $k-\omega$ SST CFD runs are compared to the test results. The data is overlaid in Figure 5.25 to show a clear discrepancy between the CFD and PIV data, with the majority of that being in the range of 0.4<MFR<0.5 and $h = 14, 21, 28, 35$ cases. In the low MFR range, the CFD model over-predicts the jet deflection by an excessive margin. This behavior can be explained by numerical hysteresis as the order of the simulations for every offset position is performed from low to high MFR. The pseudo-transient behavior of the circulation between the

jet and offset plate can be the reason for the systematic higher deflections seen in the higher MFR ranges. Nonetheless, the direction and offset of the control curves predicted by CFD still follow the trends shown in the experiment.

The PIV data showed that for a given MFR, the variation in the reattachment point location with the surface offset distance for the installed cases is nearly linear. This has been confirmed by the close to uniformly spaced curves shown in Figure 5.20. Similarly, the $k-\omega$ SST turbulence model is employed to estimate the reattachment point location for the exact offset distances. This exercise assesses the model's capability in simulating two of the most challenging flow dynamics to capture with RANS models: high curvature flows and wall reattachment. These flow phenomena are critical to capture correctly with the model as they largely contribute to the control authority of the twin intersecting jets. The reattachment points predicted by the $k-\omega$ SST model show very high agreement, within less than 5% error, for low offset distances ($h = 7$ and $h = 14$) across the whole simulated MFR range. This demonstrates the solver's decent capability in simulating the jet's curvature under aggressive pressure gradients leading to the deviation of the jet centerline significantly. For higher offset distances, the error in the reattachment point prediction increases and becomes more apparent for $h = 21$ case. The solver over-predicts the RP location for the majority of the MFR range. The higher RP position indicates a delayed prediction of the reattachment by CFD. It could be seen from the experimental data that the reattachment for the mid-level offset distance is caused by both the deflection of the centerline and the stretching of the jet boundary resulting in a "soft snap". CFD seems to be incapable of capturing this stretching effect the jet boundary undergoes. When the jet is directed toward the plate for lower MFR values, the CFD model suggests closer reattachment than that suggested by the test data. It is observed that the CFD reattachment curves converge to a single point at MFR<0.25, which is not reflected by the test data.

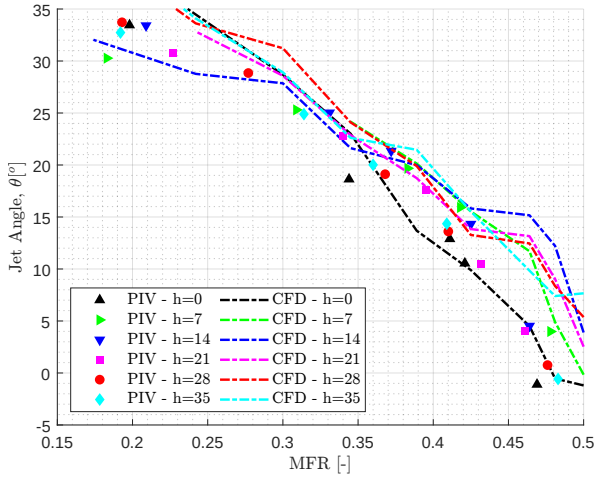

Figure 5.25: PIV vs CFD (k-ω SST) Installed Jet Control Curves

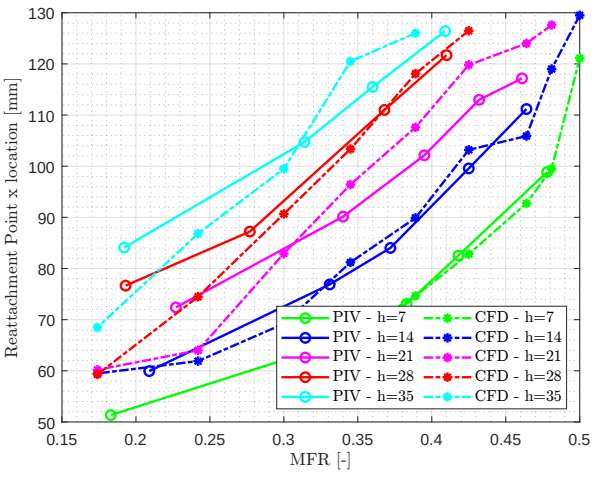

Figure 5.26: PIV vs CFD (k-ω SST) Installed RP Locations

6

Conclusion

A single jet flow field can be divided into three main regions based on the decay characteristics: the potential core, the characteristic decay region, and the axisymmetric decay region. The jet maintains its centerline velocity in the potential core region; as the shear layers grow, the centerline velocity drops. The jet decay profile in the characteristic region varies with the aspect ratio and geometry of the nozzle and completely vanishes with axisymmetric nozzles. For asymmetric jets, the decay exponent in the characteristic decay region varies non-linearly with the aspect ratio and realizes a local minimum at an aspect ratio of 0.1. In the axisymmetric decay region, the jet becomes self-similar and is characterized by a circular profile. As the jet exits the nozzle it tends to entrain the surrounding air due to the mixing nature of the shear layer. The entrainment intensity of a jet is a function of the turbulence intensity of the jet boundary at the exit plane. As the jet travels through a quiescent environment it entrains mass from the surrounding. Experimental work demonstrates that the mass entrainment increases nearly linearly with the axial distance as the jet develops and is higher for higher aspect ratio jets. However, The momentum flux across the jet's streamwise stations is nearly constant and independent of the jet's aspect ratio.

Exposing a jet to another adjacent jet substantially alters the behavior of the original jet. The geometry, the initial conditions, and the surrounding of each contributing jet all play roles in the merging process and the performance of the merged jet regarding the velocity decay, the spread rate, the maximum attainable centerline velocity, jet direction, and entrainment properties. For parallel jets, it is observed that the merging and combined points of the jets are strong functions of the outlet spacing. A directly proportional correlation is also noticed between the spacing ratio and the twin jets' spread and decay rates. Additionally, Reducing the jet discharge angle (pointing the jets towards each other) speeds up the merging process and increases the combined jet's direction control range based on the outlet discharge angles. This motivated reviewing the literature on the influence of discharge angle on the combined jet characteristics. The literature suggests that increasing the discharge angle boosts the maximum centerline due to the early merging; however, it does not influence the jet decay profile.

Placing a parallel wall near a jet (or multiple jets) results in a low-pressure area between the nozzle outlet and the surface, influencing the jet shape and trajectory. The lower pressure zone trapped between the jet and the surface results from the mass the moving jet entrains. This zone of circulation doesn't only pull the jet until it comes in contact with the wall at the reattachment point but also alters its characteristics upstream of this point. The curvature of the jet is found to be a parameter of the offset height and the initial conditions of the jet itself. As the flow attaches, it develops through the reattachment region, which serves as a transitional region between the free shear flow and the wall flow, beyond which the flow behaves similarly to classic wall flow.

Introducing an addition jet(s) allows for manipulating the wall attachment behavior and provides control over the combined jet angle. This does not fully eliminate the interaction between the jets and the adjacent surface. For this reason, understanding this interaction is crucial for applications that involve jet-jet and jet-wall interactions. These findings from the literature have paved the path for the author to develop the detailed workflow pursued in the rest of the thesis work.

In the present experiment, PIV measurements are conducted on the setup described in Chapter 3. The time-averaged results of this measurement revealed the main flow features of twin intersecting jets, which are found to be similar to closely spaced parallel twin jets found in the literature. For the setup in hand, it is found that the two jets merge at about $0.9 - 1w$ downstream of the nozzle, depending on the mass flow ratio. However, the inscribed upper and lower vortex core experience more variation in the streamwise position and size with the MFR. The lower vortex core had shifted from 4mm to 2mm for 0.47 to 0.2 MFR, respectively. A less notable change is observed on the upper vortex core location (the core on the opposite side of the jet deflection). The x-position of the intersecting jets demonstrates higher sensitivity to the MFR; the combined point shifts from near the nozzle's geometric center for MFR=0.5 to reside on the stronger jet as the MFR drops. The y-position of the combined point varies the most when initially shifting away from MFR=0.5, but it becomes less insensitive to further MFR changes. Since jet direction controllability is a critical component of the design of intersecting twin jet nozzles, the control performance of the current setup is assessed by varying the MFR. The acquired curve elucidates a shift from the analytical solution curve. This shift is attributed to the jet angle being agnostic of the first 0.05 MFR change in either direction. This is attributed to the pressure distribution across the converging and merging regions of the jet altering the jet deflection angle. As the effect of MFR becomes more pronounced and higher values, the control curve of the jet starts following the same trend shown by the analytical solution curve. The experimental curve is expected to collapse with the analytical solution at lower MFR as the lower channel gets blocked.

The installation surface impact is then explored on the MFR=0.5 case. The $h = 7$ offset distance shows a clear divergence of the supposedly zero-degree jet. The flow field examined indicates that the merging and combined points and the vortex core locations are oblivious of the installation surface even at the closest positions to the jet it is tested at. The effect of the installation surface only appears after the two jets merge, and more specifically, closer to where the vortex core exists. This behavior is rational as the peak suction prevails in the vortex core. Inspecting the variation in the jet deflection with respect to the different offset distances reveals that the onset of the installation surface effect the jet angle advects along with the vortex core location, leaving the upstream region jet considerably less impacted. As the jet starts experiencing a higher pressure gradient across its boundary and deflects towards the surface, its velocity starts to gradually. The minimum velocity point across the jet is found to be where the jet's lower shear layer impinges on the surface and stagnates. Between the location where the jet starts deflecting and it first contacts the surface, its decay rate rises. The relatively higher pressure at the reattachment point accelerates the jet as it moves along the wall allowing it to compensate for expedited decay due to the higher kinetic energy diffusion resulting from the wall interaction.

The placement of the surface in close vicinity to the nozzle outlet alters the angle of the jet for a given MFR. The control curves acquired from the experiment show a clear shift in the y-axis direction across the entire range, varying from about 40% to 60% depending on the offset distance and the MFR. Moving the installation surface away reduces this shift and brings the control curve closer to that of the uninstalled case. However, an exact match of the installed and

uninstalled control curve is never achieved, even at the largest offset distance position. Tracking the reattachment point for the different cases also reveals that the jet reattachment length varies linearly with the offset distance regardless of the jet's angle. This finding helps define the trade-off between the desired jet angle range and the design of the installation surface's offset distance, length, and profile during the design process. Since it is revealed by the experiment that the effect of the installation surface mainly lies in the formation of a circulation zone between the jet and the surface. The key to reducing or mitigating that installation effect would be by addressing this circulation. This can be done by introducing another jet that disturbs its boundary layer, which might lead to more complex interactions. A geometric feature could be added to the surface to prevent the reversal of the portion of the jet boundary that travels backward post-impingement.

With RANS offering acceptable solutions for different engineering applications at a relatively affordable cost, different 2+ equation models RANS turbulence models are assessed to select the most appropriate for simulating this type of flow dynamics. CFD model validation is initially performed using an arbitrary turbulence model to confirm the potential of RANS in simulating free shear flows and momentum mixing. This model is then used to perform grid and turbulence intensity sensitivity studies. The outcome of these study suggests that the jet centerline velocity decay and spread rate are highly dependent on the mesh resolution, and accurate prediction of these attributes requires capturing length scales that are as small as 1 mm in the near-field region. Additionally, a higher resolution of the flow inside the nozzle and the wall resolution is shown to be required. A mesh base size of 2 mm and a volume refinement size of 1 mm are shown to be adequate. Moreover, the inlet turbulence intensity prescribed considerably affects the jet characteristic profiles. High turbulence intensities at the inlet are shown to destabilize the jet, with the instability's frequency being a function of the turbulence intensity. This study showed the importance of selecting turbulence intensity within reasonable ranges based on the application. An Inlet turbulence intensity of 1% is chosen for the present study's computational runs.

The validated CFD model is then used to assess 4 different turbulence models. The results of the $MFR = 0.5$ case reveal that the $k-\omega$ SST and RSM agree the most with the experimental data, with RSM demonstrating higher convergence. However, for the given mesh size and computational resources, the cost of the RSM simulation is nearly double the $k-\omega$ SST counterpart. Hence, the $k-\omega$ SST is found to be an adequate turbulence model for the application. This turbulence model is then examined to evaluate the installation effect of the jet. The results show this model's validity for capturing the control curve trends. However, the CFD curves indicate numerical hysteresis signified by the large disparity of the CFD data at higher MFRs. Apart from the 0.4<MFR<0.5 range, the discrepancy from the experimental data is found to be around 5° or about 6% of the full control range. This disparity is considered significant as it's in the same order as the control curve shift due to the installation effect. This makes differentiating the actual jet behavior from the error challenging. Hence, the $k-\omega$ SST is deemed inadequate to quantify the exact installation effects. However, the directionality of the offset distance effect on the curves is found to be consistent when compared to the experiment, making CFD a good comparative tool for this application.

References

[1] Zhang W. "Study on the key technology of thermal environment and occupant's thermal comfort in vehicles". In: *Ph.D. Thesis. South China University of Tech, Guangdong, China* (2013).

[2] Dayi Lai et al. "A two-dimensional model for calculating heat transfer in the human body in a transient and non-uniform thermal environment". In: *Energy and Buildings* 118 (Apr. 2016), pp. 114–122. DOI: 10.1016/j.enbuild.2016.02.051.

[3] Dayi Lai et al. "Measurements and predictions of the skin temperature of human subjects on outdoor environment". In: *Energy and Buildings* 151 (Sept. 2017), pp. 476–486. DOI: 10.1016/j.enbuild.2017.07.009.

[4] "ISO/TS 14505-1:2007 Ergonomics of the thermal environment—Evaluation of thermal environments in vehicles". In: (2006).

[5] "E. ISO, ISO 7730 - Ergonomics of the thermal environment Analytical determination and interpretation of thermal comfort using calculation of the PMV and PPD indices and local thermal comfort criteria". In: (2005).

[6] P. O. Fanger. "Thermal comfort. Analysis and applications in environmental engineering". In: *Danish Technical Press* (1970).

[7] Nishi Gagge Stolwijk. "An Effective Temperature Scale Based on a Simple Model of Human Physiological Regulatory Response". In: *the Faculty of Engineering, Hokkaido University* (1972).

[8] Paul Danca et al. "An Overview of Current Methods for Thermal Comfort Assessment in Vehicle Cabin". In: *Energy Procedia*. Vol. 85. Elsevier Ltd, 2016, pp. 162–169. DOI: 10.1016/j.egypro.2015.12.322.

[9] Fredrik Norin et al. *Driver Vigilance-The Effects of Compartment Temperature Reprinted from: Design and Performance of Climate Control Systems*. Tech. rep.

[10] Andrzej Szczurek et al. "Categorisation for air quality assessment in car cabin". In: *Transportation Research Part D: Transport and Environment* 48 (Oct. 2016), pp. 161–170. DOI: 10.1016/j.trd.2016.08.015.

[11] Xiaojie Zhou et al. *Experimental Investigation of Thermal Comfort in a Passenger Car under Driving Conditions 2 3*. Tech. rep.

[12] M. C. Gameiro da Silva. "Measurements of comfort in vehicles". In: *Measurement Science and Technology* 13.6 (2002). DOI: 10.1088/0957-0233/13/6/201.

[13] Gautam Peri et al. "Cool Down Analysis of an HVAC System Using Multi-Zone Cabin Approach". In: *SAE Technical Papers*. Vol. 2017-March. March. SAE International, Mar. 2017. DOI: 10.4271/2017-01-0182.

[14] David Marcos et al. “The development and validation of a thermal model for the cabin of a vehicle”. In: *Applied Thermal Engineering* 66.1-2 (2014), pp. 646–656. DOI: 10.1016/j.applthermaleng.2014.02.054.

[15] Dayi Lai et al. “Modelling dynamic thermal sensation of human subjects in outdoor environments”. In: *Energy and Buildings* 149 (Aug. 2017), pp. 16–25. DOI: 10.1016/j.enbuild.2017.05.028.

[16] Pearson JT Burch SD Ramadhyani S. “Experimental study of passenger thermal comfort in an automobile under severe winter conditions”. In: *ASHRAE Transactions 97* (1991).

[17] Castiglioni Giacomo et al. *THERMAL SYSTEM WITH HIGH ASPECT RATIO VENT - TESLA PATENT*. Tech. rep. 2017.

[18] Stephen B Pope. *Turbulent Flows*. Tech. rep. 2000.

[19] Nicholas Trentacoste et al. “Further experimental results for three- dimensional free jets”. In: *AIAA Journal* 5.5 (1967), pp. 885–891. DOI: 10.2514/3.4096.

[20] Zaman et al. “The ‘preferred mode’ of the axisymmetric jet”. In: *Cambridge University Press* (1981).

[21] Abramovich. *The Theory of Turbulent Jets*. Tech. rep. 1963.

[22] A. Bejan et al. “Evolution: Why all plumes and jets evolve to round cross sections”. In: *Scientific Reports* 4 (Apr. 2014). DOI: 10.1038/srep04730.

[23] G. F. Marsters et al. “INFLUENCE OF ASPECT RATIO ON INCOMPRESSIBLE, TURBULENT FLOWS FROM RECTANGULAR SLOTS.” In: *Aeronautical Quarterly* 31.pt 4 (1980), pp. 285–305. DOI: 10.1017/s0001925900008957.

[24] N Rajaratnam. *Turbulent Jets (Developments in Water Science, Volume 5)*. Tech. rep. 1976.

[25] G. V. Kozlov et al. “Influence of initial conditions at the nozzle exit on the structure of round jet”. In: *Thermophysics and Aeromechanics* 15.1 (2008), pp. 55–68. DOI: 10.1134/S0869864308010046.

[26] W. R. Quinn. “Development of a large-aspect-ratio rectangular turbulent free jet”. In: *AIAA Journal* 32.3 (1994), pp. 547–554. DOI: 10.2514/3.12020.

[27] Fazle Hussain et al. *Elliptic jets. Part 1. Characteristics of unexcited and excited jets*. Tech. rep. 1989, pp. 257–320.

[28] A. A. Sfeir. “Investigation of three-dimensional turbulent rectangular jets”. In: *AIAA Journal* 17.10 (1979), pp. 1055–1060. DOI: 10.2514/3.61277.

[29] Y Tsuchiya et al. *Experiments in Fluids On the spread of rectangular jets* *. Tech. rep. 1986, pp. 197–204.

[30] Chih Ming Ho et al. “Vortex induction and mass entrainment in a small-aspect-ratio elliptic jet”. In: *Journal of Fluid Mechanics* 179 (1987), pp. 383–405. DOI: 10.1017/S0022112087001587.

[31] S. Husain et al. “Elliptic jets. Part 3. Dynamics of preferred mode coherent structure”. In: *Cambridge University Press* (1992).

[32] Zaman KB. *Axis switching and spreading of an asymmetric jet: the role of coherent structure dynamics*. Tech. rep. 1996, pp. 1–27.

[33] F. Grinstein. "Vortex dynamics and entrainment in rectangular free jets". In: *Laboratory for Computational Physics Fluid Dynamics, Code 6410, Naval Research Laboratory, Washington, DC 20375-5344, USA* (2001).

[34] F P Ricout et al. *Measurements of entrainment by axisymmetrical turbulent jets*. Tech. rep. 1960.

[35] Dai Albertson et al. "Diffusion of Submerged Jets". In: *Transactions of the American Society of Civil Engineers* (1950).

[36] A. Nasr et al. *Comparison of flow characteristics in the near field of two parallel plane jets and an offset plane jet*. 1997. DOI: 10.1063/1.869404.

[37] David R Miller et al. *Force-momentum fields in a dual-jet flow*. Tech. rep. 1959.

[38] H. Elbanna et al. "Investigation of two plane parallel jets". In: *AIAA Journal* 21.7 (1983), pp. 986–991. DOI: 10.2514/3.8187.

[39] J C S Lai et al. *Two parallel plane jets: comparison of the performance of three turbulence models*. Tech. rep. 1998.

[40] N Fujisawa et al. *Interaction of Two Parallel Plane Jets of Different Velocities*. Tech. rep. 2. 2004, pp. 135–142.

[41] Eiichi Tanaka. *The Interference of Two-Dimensional Parallel Jets (2nd Report)*. Tech. rep. 1974.

[42] Saya Lee et al. "Experimental study of flow structures near the merging point of two parallel plane jets using PIV and POD". In: *International Journal of Heat and Mass Transfer* 116 (2018), pp. 871–888. DOI: 10.1016/j.ijheatmasstransfer.2017.09.047.

[43] Ramin Naseri Oskouie et al. "Effect of Nozzle Spacing on Turbulent Interaction of Low-Aspect-Ratio Twin Rectangular Jets". In: *Flow, Turbulence and Combustion* 103.2 (Aug. 2019), pp. 323–344. DOI: 10.1007/s10494-019-00023-1.

[44] Eiichi Tanaka. *The Interference of Two-Dimensional Parallel Jets (1st Report)*. Tech. rep. 1973.

[45] Robert E. Spall et al. "Momentum flux in plane, parallel jets". In: *Journal of Fluids Engineering, Transactions of the ASME*. Vol. 126. 4. July 2004, pp. 665–670. DOI: 10.1115/1.1778717.

[46] Ameya Durve et al. "Numerical investigation of mixing in parallel jets". In: *Nuclear Engineering and Design* 242 (Jan. 2012), pp. 78–90. DOI: 10.1016/j.nucengdes.2011.10.051.

[47] H. Elbanna et al. "Interaction of two nonequal plane parallel jets". In: *AIAA Journal* 25.1 (1987), pp. 12–13. DOI: 10.2514/3.9571.

[48] Anthony S Harpham et al. *Flow Field of Practical Dual Rectangular Jets*. Tech. rep. 1996.

[49] H. Elbanna et al. "Interception of two equal turbulent jets". In: *AIAA Journal* 23.7 (1985), pp. 985–986. DOI: 10.2514/3.9027.

[50] H. Elbanna et al. “Interaction of two nonequal jets”. In: *AIAA Journal* 24.4 (1986), pp. 686–687. DOI: 10.2514/3.9329.

[51] Holly M. Krutka et al. “Analysis of a melt-blowing die: Comparison of CFD and experiments”. In: *Industrial and Engineering Chemistry Research* 41.20 (Oct. 2002), pp. 5125–5138. DOI: 10.1021/ie020366f.

[52] Bradbury. *AN INVESTIGATION INTO THE STRUCTURE OF A TURBULENT PLANE JET*. Tech. rep. Queen Mary College, 1963.

[53] Brian D Tate et al. *Modified Dual Rectangular Jets for Fiber Production*. Tech. rep. 1998.

[54] Murai Kazuhiro et al. *An Experimental Study on Confluence of Two Two-Dimensional Jets*. Tech. rep. 1976.

[55] Holly M. Krutka et al. “Effects of Die Geometry on the Flow Field of the Melt-Blowing Process”. In: *Industrial and Engineering Chemistry Research* 42.22 (Oct. 2003), pp. 5541–5553. DOI: 10.1021/ie030457s.

[56] C. Bourque et al. “Reattachment of a Two-Dimensional, Incompressible Jet to an Adjacent Flat Plate”. In: *Aeronautical Quarterly* 11.3 (Aug. 1960), pp. 201–232. DOI: 10.1017/s0001925900001797.

[57] R A Sawyer. *The flow due to a two-dimensional jet issuing parallel to a flat plate*. Tech. rep. 1960.

[58] R. Sawyer. “Two-dimensional reattaching jet flows including the effects of curvature on entrainment”. In: *Cambridge University Press* (1963).

[59] J R R Pelfrey et al. *Mean Flow Characteristics of a Turbulent Offset Jet*. Tech. rep. 1986. URL: http://fluidsengineering.asmedigitalcollection.asme.org/.

[60] J R R Pelfrey et al. *Experiments in Fluids Effect of curvature on the turbulence of a two-dimensional jet*. Tech. rep. 1986, pp. 143–149.

[61] Soon Hyun Yoon et al. *Comparative Study of a Turbulent Wall-Attaching Offset Jet and a Plane Wall Jet*. Tech. rep. 2. 1993, pp. 101–102.

[62] D T Walker’ et al. *Turbulent structure in free-surface jet flows*. Tech. rep. 1995, pp. 223–261.

[63] Jiahao Tian et al. “Characteristics of a jet in the vicinity of a free surface”. In: *Journal of Fluids Engineering, Transactions of the ASME* 134.3 (2012). DOI: 10.1115/1.4005739.

[64] Tachie Tay Rahman. “Characteristics of a horizontal square jet interacting with the free surface”. In: *Phys. Fluids* (2017).).

[65] Rupp Carriveau Girish Sankar Ram Balachandar. “Tailwater effects on the characteristics of a square jet near a free-surface”. In: *Phys. Fluids* (2010.).).

[66] N. Rajaratnam et al. “Jets de surface libre turbulents non portants”. In: *Journal of Hydraulic Research* 22.2 (1984), pp. 103–115. DOI: 10.1080/00221688409499387.

[67] Liu Wen Kim. “Dynamic structures of a submerged jet interacting with a free surface”. In: *Exp. Thermal Fluid Sci.* (2014).).

[68] Liu Wen Kim. “Structure analysis of a low Reynolds number turbulent submerged jet interacting with a free surface”. In: *Exp. Thermal Fluid Sci.* (2014).).

[69] Mishra Tay et al. “Free surface effects on the statistical properties of a submerged rectangular jet”. In: *Phys. Fluids* (2017).).

[70] Tachie Rahman Tay. “Effects of Nozzle Geometry on Turbulent Characteristics and Structure of Surface Attaching Jets”. In: *Flow, Turbulence and Combustion* (2019).).

[71] Hyeong-Mo Koo et al. *PREDICTION OF TURBULENT OFFSET JET FLOWS WITH A N ASSESSMENT OF QUICKER SCHEME*. Tech. rep. 1992, pp. 355–372.

[72] L M Jiji. *Theoretical and Experimental Temperature Distribution in Two-Dimensional Turbulent Jet-Boundarf Interaction*. Tech. rep. 1981. URL: http://heattransfer.asmedigitalcollection.asme.org/.

[73] Ruochuan Gu et al. *MODELING TWO-DIMENSIONAL TURBULENT OFFSET JETS*. Tech. rep. 1996.

[74] Tanmoy Mondal et al. “Numerical study on mean flow field of turbulent dual offset jet”. In: *Proceedings of the Institution of Mechanical Engineers, Part C: Journal of Mechanical Engineering Science* 235.23 (Dec. 2021), pp. 6865–6882. DOI: 10.1177/09544062211000774.

[75] Markus Raffel et al. *Particle Image Velocimetry: A Practical Guide*. 3rd. Berlin, Germany: Springer, 2018. DOI: 10.1007/978-3-319-65897-4.

[76] R.J. Adrian et al. “Particle-imaging techniques for experimental fluid mechanics”. In: *Annual Review of Fluid Mechanics* 23.1 (1991), pp. 261–304. DOI: 10.1146/annurev.fl.23.010191.001401.

[77] F. Scarano. *Experimental Aerodynamics*. Delft University of Technology, 2013.

[78] Roberto Merino-Martínez et al. “Aeroacoustic design and characterization of the 3D-printed, open-jet, anechoic wind tunnel of Delft University of Technology”. In: *Applied Acoustics* 170 (Dec. 2020). DOI: 10.1016/j.apacoust.2020.107504.

[79] Lavision. *Davis*. Version 10.2. Mar. 11, 2023. URL: https://www.lavision.de/en/products/davis-software/.

[80] Klas Svensson. *Experimental and numerical investigations of confluent round jets*. Division of Energy Systems. Department of Management and Engineering. Linköping University, 2015, p. 127.

[81] F. R. Menter. “Two-equation eddy-viscosity turbulence models for engineering applications”. In: *AIAA Journal* 32.8 (1994), pp. 1598–1605. DOI: 10.2514/3.12149.

[82] Maruszewski J.P. Weiss J.M. et al. “Implicit solution of preconditioned Navier-Stokes equations using algebraic multigrid”. In: (1999). Accessed: 2022-05-25.

[83] Francesco Bonelli et al. “High-speed turbulent gas jets: an LES investigation of Mach and Reynolds number effects on the velocity decay and spreading rate”. In: *Flow, Turbulence and Combustion* 107.3 (Sept. 2021), pp. 519–550. DOI: 10.1007/s10494-021-00242-5.

[84] W R Quinn et al. *Effects of nonparallel exit flow on turbulent free jets round*. Tech. rep. 1989.

[85] B E Launder et al. *THE NUMERICAL COMPUTATION OF TURBULENT FLOWS*. Tech. rep. 1974, pp. 269–289.

[86] D.C. Wilcox. “Turbulence Modeling for CFD”. In: *Handbook of Computational Fluid Mechanics*. Ed. by E.H. Hirschel. New York, NY: Springer, 2006, pp. 235–292. DOI: 10.1007/978-3-540-26443-5_8.

[87] A. N. Kolmogorov. “Equations of turbulent motion in an incompressible fluid”. In: *Izvestiya Akademii Nauk SSSR, Seriya Fizicheskaya* 5.3 (1941), pp. 3–14.

[88] P G Saffman. *A Model for Inhomogeneous Turbulent Flow*. Tech. rep. 1530. 1970, pp. 417–433.

[89] Version 2021.1 Software Package. *Simcenter STAR-CCM+*. 2021.

[90] Philippe R Spalart et al. *Effective Inflow Conditions for Turbulence Models in Aerodynamic Calculations*. Tech. rep. 2012.

[91] J.F. Foss. “Flow Characteristics of the Defined Region Geometry for High-Gain Proportional Amplifiers”. In: *Proceedings of the 1967 Fluidics Symposium*. Chicago, IL: The American Society of Mechanical Engineers, May 1967, pp. 45–61.

[92] G. Han et al. “Some Observations of the Coanda Effect”. In: *Engineering Turbulence Modelling and Experiments 6*. Elsevier, 2005, pp. 545–553. DOI: 10.1016/B978-008044544-1/50052-2.

[93] N W M Ko et al. *Flow Structures in Initial Region of Two Interacting Parallel Plane Jets*. Tech. rep. 1989.

[94] Y. F. Lin et al. “Interaction of parallel turbulent plane jets”. In: *AIAA Journal* 29.9 (1991), pp. 1372–1373. DOI: 10.2514/3.10749.

[95] Elgin A. Anderson et al. *Experimental and numerical investigation of two-dimensional parallel jets*. 2001. DOI: 10.1115/1.1363701.

[96] X. K. Wang et al. “Experimental investigation of the interaction between a plane wall jet and a parallel offset jet”. In: *Experiments in Fluids* 42.4 (Apr. 2007), pp. 551–562. DOI: 10.1007/s00348-007-0263-9.

[97] Huhu Wang et al. “Particle image velocimetry measurements of the flow in the converging region of two parallel jets”. In: *Nuclear Engineering and Design* 306 (Sept. 2016), pp. 89–97. DOI: 10.1016/j.nucengdes.2015.09.032.

[98] Xin Sanfa et al. “Investigation into the effect of the angle of dual slots on an air flow field in melt blowing via numerical simulation”. In: *E-Polymers* 16.4 (July 2016), pp. 337–342. DOI: 10.1515/epoly-2016-0057.

[99] Sheng Xie et al. “Particle Image Velocimetry (PIV) investigation of the turbulent airflow in slot-die melt blowing”. In: *Polymers* 12.2 (Feb. 2020). DOI: 10.3390/polym12020279.

A

Literature Summary

Table A.1: Free Parallel Twin Jet Literature

Author	Aspect Ratio (l/w)	Spacing ratio (2h/w)	Re	Merging Point (x_{mp}/w)	Measurement Technique
[37]	40	6	17,800	8.5	HWA
[44, 41]	N/A	8.5-26.3	4290-8750	$5.06(2h/w)^{0.27}$ for $(8.5 < 2h/w < 16)$ $0.667(2h/w)$ for $(16 < 2h/w)$	HWA
Militzer	0	6	55,600	7.1	HWA
[38]	40.8	12.5	20,000	12	HWA
[93]	0	2.5	40,000	1.75	HWA
[94]	90	30,40	7,600	21.6, 27.6	Split-film
[36]	24	4.25	8,300-19,300	4.3	LDA
[95]	32	9,13,18.25	6,000	10,14,18	HWA & CFD
[96]	0	2	10,000	0.75	PIV
[46]	N/A	3.5 - 40.1	21,000	$0.721(2h/w) + 2.06(I) - 2.453$	HWA & CFD
[97]	15.1	3.1	9,100	1	LDA & PIV
[42]	0	3.07	4,900	1	PIV
[43]	0	3,4.5,6,9,12	6,500	1,2.75,4,7.5,10.5	PIV

Table A.2: Free Intersecting Twin Jet Literature

Author	Spacing ratio (2h/w)	Discharge angle	Surface Recession (a/w)	Re	Measurement Technique
[54]	4,17,21,24,31	0,15,30,45	0	4603-25594	HWA
[49]	12.5	30,60,80,100	0	20000	HWA
[48]	4.1	60	0	3800, 7600	Pitot Probe
[53]	0,4.1	60,70	0,	3800,7600	HWA
[51]	0,4.1	60,70	0	1.75	CFD
[55]	0	60	$\pm 1/4, \pm 1/2, \pm 1, \pm 5/4, +3/2$	0	CFD
[98]	0.41	0,20,40,50,60,70,80,100,120	0	4.3	CFD
[99]	0	2	10,000	0.75	PIV

B

PIV Experiment Test matrix

Block Number	Sub-Block Number	Measurement Plane (Y=) [mm]	Offset Distance [mm] (z)	Flap Angle [deg]	Uc [m/s]	Flow Rate [CMH]	Reynolds Number	Dt(mus)	Objective
Block 1	Sub-Block 1	-20	0	0	25	567	16610	24	Flow two dimensionality and Re Independence
		-20	0	0	20	453.6	13288	30	
		-20	0	0	15	340.2	9966	40.00	
		-20	0	0	10	226.8	6644	60	
	Sub-Block 2	20	0	0	25	567	16610	24	
		20	0	0	20	453.6	13288	30	
		20	0	0	15	340.2	9966	40.00	
		20	0	0	10	226.8	6644	60	
	Sub-Block 3	0	0	0	25	567	16610	52	
		0	0	0	20	453.6	13288	65	
		0	0	0	15	340.2	9966	86.67	
		0	0	0	10	226.8	6644	130	
	Sub-Block 4	0	7	0	25	567	16610	52	
		0	7	0	20	453.6	13288	65	
		0	7	0	15	340.2	9966	86.67	
		0	7	0	10	226.8	6644	130	
Block 2	Sub-Block 1	0	0	0	20	453.6	13288	30	Installation effect on control authority for various offset distances
		0	0	5	20	453.6	13288	30	
		0	0	7.5	20	453.6	13288	30	
		0	0	10	20	453.6	13288	30	
		0	0	15	20	453.6	13288	30	
	Sub-Block 2	0	7	0	20	453.6	13288	30	
		0	7	5	20	453.6	13288	30	
		0	7	7.5	20	453.6	13288	30	
		0	7	10	20	453.6	13288	30	
		0	7	15	20	453.6	13288	30	
	Sub-Block 3	0	14	0	20	453.6	13288	30	
		0	14	5	20	453.6	13288	30	
		0	14	7.5	20	453.6	13288	30	
		0	14	10	20	453.6	13288	30	
		0	14	15	20	453.6	13288	30	
	Sub-Block 4	0	21	0	20	453.6	13288	30	
		0	21	5	20	453.6	13288	30	
		0	21	7.5	20	453.6	13288	30	
		0	21	10	20	453.6	13288	30	
		0	21	15	20	453.6	13288	30	
	Sub-Block 5	0	28	0	20	453.6	13288	30	
		0	28	5	20	453.6	13288	30	
		0	28	7.5	20	453.6	13288	30	
		0	28	10	20	453.6	13288	30	
		0	28	15	20	453.6	13288	30	
	Sub-Block 6	0	35	0	20	453.6	13288	30	
		0	35	5	20	453.6	13288	30	
		0	35	7.5	20	453.6	13288	30	
		0	35	10	20	453.6	13288	30	
		0	35	15	20	453.6	13288	30	

Figure B.1: PIV Measurement Campaign Test Matrix